SYNTHESIS AND CHARACTERIZATION OF PEROVSKITE NANOSTRUCTURES

Kristina Žagar

Doctoral Dissertation
Jožef Stefan International Postgraduate School
Ljubljana, Slovenia, May 2011

Supervisor: *Prof. Dr. Miran Čeh*

Evaluation Board:

Assist. Prof. Dr. Aleksander Rečnik, Jožef Stefan Institute, Jamova cesta 39, 1000 Ljubljana

Assist. Prof. Dr. Sašo Šturm, Jožef Stefan Institute, Jamova cesta 39, 1000 Ljubljana

Dr. Andreja Gajović, Ruđer Bošković Institute, Bijenička 54, 10000 Zagreb, Croatia

MEDNARODNA PODIPLOMSKA ŠOLA JOŽEFA STEFANA
JOŽEF STEFAN INTERNATIONAL POSTGRADUATE SCHOOL

Kristina Žagar

SYNTHESIS AND CHARACTERIZATION OF PEROVSKITE NANOSTRUCTURES

Doctoral Dissertation

SINTEZA IN KARAKTERIZACIJA PEROVSKITNIH NANOSTRUKTUR

Doktorska disertacija

Supervisor: Prof. Dr. Miran Čeh

Ljubljana, Slovenia, May 2011

Table of Contents

Abstract

Polycrystalline, $BaTiO_3$ nanorods and $SrTiO_3$ nanotubes were synthesized by the electrophoretic deposition (EPD) of a barium titanate sol and a strontium titanate sol into 2D ordered anodic aluminium oxide templates (AAO) with a subsequent thermal treatment and template removal.

The $BaTiO_3$ nanorods grown within the AAO template membranes had diameters ranging from 150 to 200 nm, with an average length of 10-25 μm. The following processing parameters were systematically varied in order to obtain $BaTiO_3$ nanorods with the most uniform morphology: applied potential, time of deposition, annealing temperature and annealing time. The obtained $BaTiO_3$ nanorods were always polycrystalline and were composed of well-crystallized xenomorphic pseudo-cubic $BaTiO_3$ grains, ranging from 10 to 30 nm. Grain boundaries between the $BaTiO_3$ grains contained an approximately 1-nm-thick amorphous phase with the composition matching $BaTiO_3$. It was shown that the processed nanorods were homogeneous with respect to their chemical composition and grain size along their longer axis. In addition to cubic polymorph hexagonal $BaTiO_3$ polymorph was observed as intergrowth of more or less dense sequences of (111) twins. Its formation was triggered by the reduction of Ti^{4+} to Ti^{3+} as a consequence of highly reducing atmosphere during the annealing process. When AAO templates containing the BT sol were annealed in an oxygen atmosphere the presence of the hexagonal polymorph was significantly reduced.

Electrical measurements performed on single polycrystalline $BaTiO_3$ nanorods showed resistivity values between 10 and 100 ohm·cm, which is in a good agreement with typical reported values for oxygen-deficient barium titanate. Single $BaTiO_3$ nanorods were tested as proof-of-concept humidity sensors. The measurements of the electrical resistivity of the single $BaTiO_3$ nanorods in a varying humidity environment showed a reproducible response, thus demonstrating that single $BaTiO_3$ nanorods can be integrated into complex circuit architectures with the functional capacities of a humidity nanosensor.

Polycrystalline $SrTiO_3$ nanotubes that were obtained by the electrophoretic deposition of a ST sol into AAO membranes were dense and polycrystalline with outer diameters of approximately 200 nm, inner diameters of approximately 180 nm and lengths ranging from a few micrometres up to a few tens of micrometres.

A unique phenomenon of the self-ordering of $SrTiO_3$ nano-cubes inside the AAO template was observed that was not yet reported for any other material prepared by the EPD of sols into templates and subsequent annealing. This unusual crystallization mechanism resulted in the assembly of highly-organized $SrTiO_3$ nanocrystals in a perfect cube-to-cube arrangement. Namely, homogeneous nucleation inside the AAO pores produces a critical number of $SrTiO_3$ crystallites, which leads to their self-organization as soon as the nanocrystals reach the sizes that equal to the mean free distance between the nuclei. Due to steric constraints the crystals start to rearrange in order to most efficiently fill the available surface on the pore walls. This process leads to the formation of domains containing a large number of idiomorphic $SrTiO_3$ nano-cubes that are self-aligned into an almost perfect cube-on-cube and cube-to-wall registry, which cover the walls. The described mechanism shows the ability of nanocrystals with well defined morphologies to adopt to spatial constraints and self-organize into desired architectures. By optimizing the processing parameters one should be able to control the rates of nucleation and growth, the morphology dictated by the crystallography of the nanocrystal units, exploit the self-organization mechanism to design layers of any desired material in a chosen crystallographic orientation in virtually any geometrical setting.

The electric properties of single $SrTiO_3$ nanotubes doped with Fe to modify the materials conductivity were investigated by measuring their current-voltage (I-V) characteristics at room temperature. The results showed ideal linear I-V characteristics with the electrical resistivity of a single Fe-doped $SrTiO_3$ nanotube of 35 ohm·cm. Additionally, a single Fe-doped $SrTiO_3$ nanotube-based device was tested as a UV photodetector. A repeatable and reversible response under the UV radiation was found with short response and recovery times, which indicates that such prototype devices can be used as UV photodetectors.

Povzetek

Polikristalinične $BaTiO_3$ nanopalčke in $SrTiO_3$ nanocevke smo sintetizirali z metodo elektroforetske depozicije (EPD) barij titanatnega sola in stroncij titanatnega sola v pore membran 2D urejenega anodiziranega aluminijevega oksida (AAO). Postopku je sledila toplotna obdelava vzorcev in odtopitev AAO membrane.

$BaTiO_3$ nanopalčke, sintetizirane v porah AAO membran so imele premer v razponu od 150 do 200 nm in povprečno dolžino od 10 do 25 μm. Z namenom pridobiti $BaTiO_3$ nanopalčke z najbolj pravilno obliko, smo sistematično spreminjali naslednje procesne parametre: napetost med depozicijo, čas depozicije, temperaturo žganja in čas žganja. Sintetizirane $BaTiO_3$ nanopalčke so polikristalinične in sestavljene iz kristaliničnih ksenomorfnih pseudo-kubičnih $BaTiO_3$ zrn velikosti od 10 do 30 nm. Na mejah med $BaTiO_3$ zrni smo zasledili do 1 nm debelo plast amorfnega $BaTiO_3$. Ugotovili smo, da imajo $BaTiO_3$ nanopalčke homogeno kemijsko sestavo v celotni dolžini palčke. Nadalje smo opazili, da ima majhen del pseudo-kubičnih $BaTiO_3$ zrn vraščene bolj ali manj urejene lamele hexagonalnega polimorfa $BaTiO_3$, ki ga strukturno lahko opišemo kot 6H zaporedje (111) dvojčkov. Vzrok za nastanek (111) dvojčkov je redukcija Ti^{4+} v Ti^{3+}, do katere pride zaradi lokalne redukcijske atmosfere med procesom žganja. Pri žganju v kisikovi atmosferi, je bila prisotnost heksagonalnega polimorfa občutno manjša.

Električne meritve, ki smo jih opravili na posameznih $BaTiO_3$ nanopalčkah so pokazale vrednosti upornosti med 10 in 100 ohm·cm. Omenjene vrednosti so primerljive z vrednostmi, ki so bile objavljene za $BaTiO_3$, ki vsebuje kisikove vrzeli. Nadalje smo $BaTiO_3$ nanopalčke testirali kot možne senzorje vlage. Meritve električne prevodnosti pri različnih stopnjah vlažnosti v okolju so pokazale ponovljiv in hiter odziv prevodnosti $BaTiO_3$ nanopalčk v odvisnosti od stopnje vlage. Slednja ugotovitev dokazuje, da lahko posamezne $BaTiO_3$ nanopalčke integriramo v kompleksna vezja s funkcijo nano-sezorjev vlage.

Polikristalinične $SrTiO_3$ nanocevke z zunanjim premerom približno 200 nm, notranjim premerom priblizno 150 nm in dolžino od nekaj mikrometrov do nekaj deset mikrometrov smo sintetizirali z metodo elektroforetske depozicije stroncij titanatnega sola v pore AAO membran.

Pri sintezi $SrTiO_3$ nanocevk smo opazili edinstven pojav samourejanja $SrTiO_3$ nano-kock znotraj AAO por, ki do sedaj še ni bil opisan za noben drug material sintetiziran z EPD sola v pore AAO membran in nadaljnim žganjem. Omenjeni pojav kristalizacije povzroči organizirano samourejanje nanokristalov v skorja idealen kocka-na-kocko zlog. Homogena nukleacija $SrTiO_3$ znotraj por namreč ustvarja kritično število kristalitov in v procesu rasti kristalov nadalje vodi k njihovemu samourejanju, ko dosežejo velikost, ki je enaka njihovi povprečni prosti razdalji. Zaradi lokalnih steričnih omejitev se kristali prično urejati, s težnjo po najbolj učinkoviti zapolnitvi razpoložljive površine na stenah por. Opisan proces vodi k nastajanju področij, ki vsebujejo veliko število idiomorfnih $SrTiO_3$ nano-kock, ki so same po sebi urejene v skoraj popoln kocka-na-kocko in kocka-na-steno sklop, ki pokriva stene cevk. Opisan mehanizem kaže, da se idiomorfni nanokristali med rastjo v amorfnem mediju lahko prilagajajo prostorskim omejitvam in se posledično organizirajo v željeni geometriji. Z optimizacijo procesnih parametrov lahko kontroliramo hitrost nukleacije in rast kristalov ter morfologijo osnovnih nanokristalitov, ki jo pretežno določa njihova kristalna struktura. Na ta način lahko oblikujemo monokristalne plasti poljubnih materialov v izbrani kristalografski orientaciji in v željeni geometriji.

$SrTiO_3$ nanocevke smo dopirali z železom, da bi povečali njihovo električno prevodnost. Merili smo tokovno-napetostne (I-V) karakteristike pri sobni temperaturi. Rezultati so pokazali idealno ohmsko odvisnost in izmerjeno upornost 35 ohm·cm na posamezni z železom dopirani $SrTiO_3$ nanocevki. Nadalje so bile nano-naprave, narejene iz posameznih, z železom dopiranih, $SrTiO_3$ nanocevk, testirane kot UV fotodetektorji. Izkazalo se je, da so pod vplivom obsevanja z UV svetlobo tokovne karakteristike nano-naprave ponovljive in imajo zelo kratkek odzivni čas, kar nakazuje na uporabnost omenjenih nano-naprav za UV nano fotodetektorje.

Abbreviations

0-D = zero dimensional

1-D = one dimensional

2-D = two dimensional

3-D = three dimensional

AAO = anodic aluminium oxide

BE = backscattered electrons

BT = barium titanate sol

DC = direct current

DLVO = Derjaguin, Landau, Varwey and Overbeek

E = electrical charge density or surface potential

EDXS = energy-dispersive X-ray spectroscopy

EPD = electrophoretic deposition

FEG = field-emission gun

FIB = focused ion beam

FSEM = field-emission scanning electron microscopy

H = Helmholtz plane

HAADF-STEM = high-angle annular dark-field scanning-transmission electron microscopy

HRTEM = high-resolution electron microscopy

I_{ph} = photocurrent

I-V = current-voltage

PC = polycarbonate

R = electrical resistance

RS = Raman spectroscopy

SAED = selected-area electron diffraction

SE = secondary electrons

SEM = scanning electron microscopy

ST = strontium titanate sol

STEM = scanning-transmission electron microscopy

TEM = transmission electron microscopy

VLS = vapor-liquid-solid

XRD = X-ray powder diffraction

z.p.c. = zero point charge

1 Introduction

1.1 Nanomaterials and nanostructures

The synthesis and fabrication of nanomaterials and nanostructures with the desired dimensions and compositions is a crucial milestone of nanotechnology. In order to achieve this goal several synthesizing techniques have been developed.[1-4] The basic feature of nanomaterials and nanostructures is their reduced dimensional system, in which one or more dimensions are reduced so that materials begin to display novel quantifiable physical properties. For solids, reduced dimensions typically cause a reduction in the coordination number; hence the electrons have less opportunity to hop from site to site, thus reducing the kinetic energy of the electrons or their bandwidth. Furthermore, the symmetries of the system are lowered and the appearance of new boundary conditions leads to unique surface and interface states. This is why new applications of nanomaterials and nanostructures can be developed with novel or significantly improved properties including transparency, hydrophobicity, photoluminescence, toughness and hardness and chemical sensing. From fabricated nanostructures, devices that exhibit superior electrical, mechanical, chemical or optical properties can be designed and build.[1-5]

There are two main approaches to synthesize and fabricate nanomaterials and nanostructures, *i.e.*, the top-down and bottom-up approaches. When forming nanoparticles, attrition milling and lithography are typical top-down techniques, whereas colloidal dispersion is just one of the examples for the bottom-up approach. Both approaches play an important role in nanotechnology, but there are some disadvantages of each approach that have to be considered.[4]

The main disadvantage arising from the top-down approach is imperfection of the surface structure. For example, lithography and/or a focused ion beam can cause significant crystallographic damage to the processed patterns. Produced nanowires are not smooth and may contain a lot of impurities and structural defects on the surface. Such imperfections would have a significant impact on the physical properties and the surface chemistry of nanostructures, since the surface over volume ratio in nanostructures is very large.

The bottom-up approach refers to a building-up of material using atom-by-atom, molecule-by-molecule or cluster-by-cluster approach and after impinging onto the growth surface they assemble into a crystal structure one after another. The bottom-up approach is very

important in the fabrication and processing of nanomaterials and nanostructures and has many advantages over the top-down approach, such as the formation of nanostructures with fewer defects, a more homogeneous chemical composition and better short- and long-range ordering. The reason for that is because the bottom-up approach is driven by the Gibbs free energy and therefore the nanomaterials and nanostructures synthesized in that manner are in a state closer to the thermodynamic equilibrium state. On the other hand, the top-down approach most likely introduces internal stresses, in addition to surface defects and contaminations.[3,4]

To properly understand and describe the diversity of modern nanomaterials and nanostructures, some general form of classification is needed.[2-5] In principle, the term "nanomaterials" preferentially describes the dimensionality of nano-sized materials, while the term "nanostructures" may already imply certain geometric arrangement of nanoparticles. Since the scope of this work is more focused on the synthesis and characterization of polycrystalline nanorods and nanotubes we prefer to use the term "nanostructures" over the term "nanomaterials".

As mentioned, the most typical way of categorizing nano-sized materials is to identify them according to their dimensions. In view of this we can distinguish zero-dimensional (0-D), one-dimensional (1-D), two-dimensional (2-D), and three-dimensional (3-D) nanostructures. 0-D nanostructures are materials where all the dimensions can be measured within the nanoscale. The most common representative of such nanostructures are nanoparticles. On the other hand, 1-D nanostructures differ from 0-D nanostructures in having one dimension that is outside the nanoscale. This difference in materials dimensions results in needle- or rod-like nanostructures. 1-D nanostructures therefore include nanotubes, nanorods and nanowires. The nanostructures can be:

- Amorphous or crystalline
- Single crystalline or polycrystalline
- Chemically pure or impure
- Stand-alone materials or embedded in other materials
- Metallic, ceramic (oxide) or polymer

Two-dimensional nanostructures are somewhat more difficult to classify, nevertheless 2-D nanostructures are materials in which two of the dimensions are not confined to the nanoscale. As a result, 2-D nanostructures exhibit a plate-like morphology. 2-D nanostructures include nanofilms, nanolayers and nanocoatings. And finally, 3-D structures are not confined to the

nanoscale in any dimension. These materials are thus characterized by having three arbitrary dimensions above 100 nm and can also be referred to as bulk materials. The reason that they are still regarded as nanostructures despite their nanoscale dimensions is that they possess a nanocrystalline structure or involve features at the nanoscale. In terms of nanocrystalline structure, bulk materials can be composed of multiple arrangements of nanosized crystals, most typically in different orientations. With respect to the presence of features at the nanoscale, 3-D nanostructures can contain a dispersion of nanoparticles, bundles of nanowires, nanotubes and/or nanorods as well as multilayers. In the following section a moe detailed description of 1-D nanostructures, which are the topic of this work, is given.[1-5]

1.2 One-dimensional nanostructures: nanorods and nanotubes

Typical one-dimensional nanostructures are nanorods, nanowires, whiskers and fibres. Nanotubes and nanocables are also considered as 1-D structures. Nanorods are generally considered to be shorter than nanowires, but the definition is often a little vague, but nevertheless nanowires in general have a higher aspect ratio than nanorods. Furthermore, 1-D nanostructures with diameters ranging from several nanometres to several hundred microns are referred to as whiskers and fibres, whereas nanorods and nanowires should not exceed a few hundred nanometres in diameter.[2-7]

Various techniques have been studied for the synthesis and formation of 1-D nanostructured materials and they can be generally classified into four groups:

- Spontaneous growth
- Template-assisted synthesis
- Electrospinning
- Lithography

Spontaneous growth, template-assisted synthesis and electrospinning are known as bottom-up techniques, whereas lithography is a top-down technique. Spontaneous growth usually results in single-crystal nanorods or nanowires formation along a preferential crystal growth direction depending on the crystal structures and surface properties of the synthesized material. In

contrast, polycrystalline or even amorphous nanorods or nanotubes are typically formed by the template-assisted synthesis.[4,8-12]

Nanorods, nanowires and nanotubes obtain a significantly larger surface area than films or bulk materials. While they possess a smaller surface area compared to the nanoparticles, they can offer many advantages in device fabrication. Nanorods, nanowires and nanotubes, which are uniformly sized with unidirectional alignment are especially useful and can function as both, structural and functional components in devices. Furthermore, nanorods, nanowires and nanotubes offer various physical properties and therefore interesting and unique applications in nanotechnology.[2,13]

1.2.1 Simple and complex metal oxides in one-dimensional nanostructures

One-dimensional nanostructures of metal oxides (AO where A is a metal) and particularly complex metal oxides with a perovskite structure $ATiO_3$ (A= Ba, Sr, Ca, Pb, *etc.*) are important materials for a variety of applications in the microelectronics industry, and more recently in nanotechnology.[2,13] This is due to their multi-faceted functional properties, their chemical and thermal stability and their mechanical properties. Metal oxides and particularly complex metal oxides possess many unique physical properties, such as ionic and electronic conductivity, superconductivity, ferroelectricity, piezoelectricity, as well as dielectric, electro-optic, electrochemical and magnetic properties. There is a wide range of applications for these materials; they can be used as electronic devices, sensors, catalysts and composites with multiple physical properties.[14-28] For example, piezoelectrics, such as lead zirconate titanate (PZT), play a key role in micro-electro-mechanical systems (MEMS).[29,30] Tin-doped indium oxide (ITO) films on glass have been used as optically transparent electrodes in light-emitting diodes or solar cells.[31] Sol-gel-derived mesoporous titania (TiO_2) films or nanorods, hydrothermally produced TiO_2 nanotubes and electrochemically anodized TiO_2 nanotubes have been extensively studied in organic-inorganic hybrid photo-electrochemical cells.[32,33] The physical properties of oxide materials can be tunable through appropriate doping or substitution. Zirconia that is partially stabilized through doping with yttrium oxide (Y_2O_3) or calcium oxide (CaO) exhibits excellent mechanical properties. On the other hand doped zirconia can also be an oxygen ionic conductor with applications in oxygen sensors and solid-oxide fuel cells.[34] Another example of a material, which has enhanced physical properties when doped is strontium titanate ($SrTiO_3$) with iron

additions. Fe-doped $SrTiO_3$ has large ionic conductivity and can be used in oxygen sensor.[35] Among the mentioned perovskite materials, barium titanate ($BaTiO_3$) is one of the most promising candidates that possesses a variety of attractive properties, such as ferroelectricity, piezoelectricity and even semiconductivity, when it is in a reduced state or when doped with aliovalent dopants. It serves as one of the most versatile functional materials for wide range of technological applications.[18,19,36-38] Working into the direction of nanodevices based on this material, 1-D $BaTiO_3$ nanostructures with a high surface-to-volume ratios in the form of nanorods or nanotubes were studied in the past, showing promising applications as basic building-blocks of, for instance, energy-harvesting systems and sensors.[19-21,39] $SrTiO_3$, on the other hand, is an ideal substrate for the epitaxial growth of many functional materials. Its high dielectric constant, thermal stability and photocatalytic properties make $SrTiO_3$ one of the most versatile functional materials for a wide range of nanotechnology applications.[2,13,16,27,33,35,40-42] As the materials approach the nanoscale dimensions their intrinsic features become subordinated to the surface properties and their functionality extends to a variety of yet unexplored potentials for the production of multifunctional nanodevices with the targeted geometries and specific physical properties.[35,40] Recently, $SrTiO_3$ in nanoscale dimensions has been highlighted as a promising candidate that improves the photo-electrochemical performance of TiO_2[27] or could even be used as a Sr delivery platform to assist osseointegration on Ti-based bone implants.[42] Furthermore, oxide surfaces can have special chemical properties and consequently they can be used as catalysts and sensors.[28] In addition, the oxide surface can easily be incorporated with organic functional groups through surface condensation or self-assembly.[43]

For many applications physical properties of the above mentioned metal oxides depend on their surface-to-volume ratio. The sensitivity or efficiency obtained is directly proportional to the surface area of the material. This is why many efforts have recently been made to synthesize and understand the growth mechanisms producing nanorods and nanotubes of functional ceramics via different processing procedures.[2,4,5] Using an evaporation-condensation process at elevated temperatures and under moderate vacuum, single-crystal oxide nanowires and nanobelts can be formed. For single-crystal growth also various forms of hydrothermal synthesis have been proposed and studied.[16,25,44,45] However, the growth of oxide nanorods or nanotubes arrays involves special control of the growth direction and also control of the size of the formed nanorods or nanowires. Examples of techniques that allow the controlled synthesis of nanorods or nanowires arrays are:

- vapour-liquid-solid (VLS) growth under vacuum,[46]
- oxidation of metallic nanorods,[47]
- seeded growth,[48,49]
- template filling of oxide colloidal particles.[11,33,50-52]

The VLS growth of oxide nanorods or nanotubes is limited to systems that can form a eutectic liquid with the substrate at a high growth temperature. However, there is still not enough information on the formation of eutectic liquids between complex oxides and possible substrates. Another method that is limited to only simple oxide materials is the oxidation of the metallic nanorods. Seed growth is another technique where single-crystal oxide nanorods can be formed. However, this method suffers from the fact that final nanorods typically possess an inverse conical shape, starting with a smaller diameter at the bottom that becomes larger as the growth proceeds. The template filling technique with oxide sol particles is another method for the growth of oxide nanorods and nanotubes and it also offers the synthesis and growth of complex oxide materials with appropriate control of sols or colloid dispersions. The template filling technique was recently upgraded to the so-called sol-gel template-assisted electrophoretic growth technique which was shown to be very promising method for the synthesis and growth of complex oxide nanorods and nanotubes.[8,50,53,54] Both methods, direct template filling and the sol-gel template-assisted electrophoretic growth technique, offer several advantages over the VLS technique, oxidation of metallic nanorods and seeded growth. The advantages of the template-assisted sol-gel electrophoretic growth technique a with detailed explanation of the procedure are explained in the following section.

1.3 Template-assisted sol-gel electrophoretic deposition

Template-assisted sol-gel electrophoretic deposition combines several processing methods:

- template-based growth,
- sol-gel processing and
- electrophoretic deposition (EPD).

This technique is a versatile method for forming nanorods and nanotubes of numerous simple and complex oxides. Sol EPD has been known as a technique for the formation of films and has only been adapted for the formation of nanorods or nanotubes for approximately ten years. This method provides several distinct advantages over the previously mentioned techniques. One of the advantages is the possibility to synthesize nanorods or nanotubes with a precise stoichiometric composition. Another great advantage is the simplicity of the method. Furthermore, it allows the fabrication of uni-directionally aligned and uniformly sized oxide nanorods or nanotubes over a large area and therefore can be impemented for device fabrication as well as for property characterization. However, complete filling of a solid inside the template pores is a challenging task since sols consist of approximately 10 % of solid dispersed in a solvent. Therefore, nanotubes are more often obtained by this technique instead of the nanorods.[4,8,9]

In the following section the template-assisted sol-gel EPD technique is explained, step by step. In the first part template-assisted synthesis is presented together with the aluminium oxide (Al_2O_3) membrane formation. Afterwards, the sol-gel processing is elucidated in detail, followed by the colloidal stabilization with electrical double-layer structure theory and the DLVO theory and finally the EPD process is explained.[4] Additionally, the applications of direct template filling and the applications of the template-assisted sol-gel EPD technique are presented.

1.3.1 Template-assisted synthesis

The template-assisted synthesis of 1-D nanostructured materials is a very general method that can be used in the synthesis of nanorods, nanowires or nanotubes of various materials such as oxides, semiconductors, metals and polymers.[4,6,10,33,51,52,55] Templates with nanosized pore channels have been explored for the template-based growth of nanorods and nanotubes. The most commonly used templates are anodic aluminium oxide (AAO) membranes and radiation track-etched hydrophilic polycarbonate (PC) membranes. Other membranes that have also been used as templates are nanochannel array glass, radiation track-etched mica, porous silicon, zeolites and carbon nanotubes.[4] AAO membranes with a uniform and parallel pore structure are formed by the anodic oxidation of an aluminium foil in appropriate electrolyte solutions. The pores are arranged in a close-packed hexagonal array with a pore sizes ranging from 10 nm to 200 nm and densities of 10^{11} pores/cm^2 can be achieved.[56] The PC membranes are made by bombarding a nanoporous polycarbonate sheet with nuclear fission fragments to create damage tracks and then these tracks are chemically etched into pores. A pore size can range from 10 nm to 10 μm and they are randomly distributed. Pore densities can be as high as 10^9 pores/cm.[2,4,10,52,57]

In addition to the desired pore size, morphology, size distribution and density of pores, templates must fulfil certain requirements. The first and the most important requirement is that the template materials must be compatible with the processing conditions. For example, templates that will be used in electro-deposition must be electrical insulators and should be chemically and thermally inert during the synthesis. The next requirement is that the depositing material or solution must wet the internal pore walls. Last but not least is that for the synthesis of nanorods or nanowires the deposition should start from the bottom or from one end of the template pores and proceed from one side to another. Kinetically, enough surface relaxation permits the maximum packing density, so a diffusion-limited process is preferred. Other considerations include the ease of the release of nanorods from the templates and handling of the templates during the experiments.[4,8]

1.3.1.1 Anodic aluminium oxide (AAO) membranes

AAO membranes with a pore densities up to 10^{12} pores/cm^2 and pore diameters down to 4 nm can be prepared electrolythically by the electrochemical oxidation of aluminium foil in an acid electrolyte under DC conditions. The formation of high-aspect-ratio nanopores during the anodic oxidation of ultra-pure aluminium was first reported by Masuda and Fukada.[56,58-60] The structure of the AAO membranes is characterized as a close-packed array of hexagonal columnar cells, each of which contains an elongated cylindrical nanopore normal to the Al surface extending from the surface of the AAO oxide layer down to the oxide/metal interface, where it is sealed by a thin oxide barrier layer (Figure 1).[56,61-66]

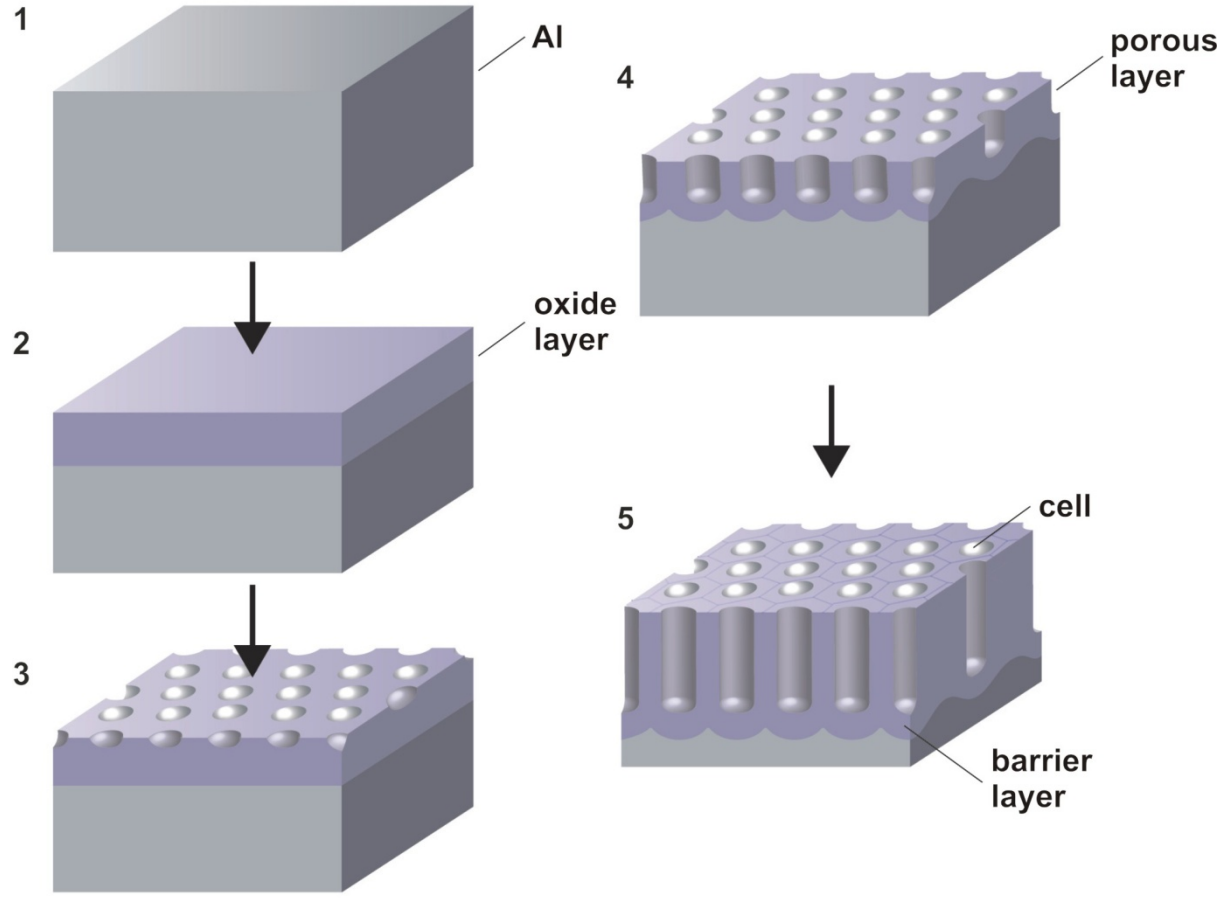

Figure 1. Formation scheme of the of AAO membrane.[56]

The pore diameters and the interpore spacing (diameter and length) are determined largely by the anodization parameters, such as the applied DC voltage, pH, type of acid, temperature of electrolyte, time of anodization, *etc.* Typically, the electrochemical oxidation of Al sheets is conducted using one of the three electrolytes, sulphuric acid, oxalic acid or phosphoric acid. Depending on the chosen electrolyte, different interpore distances ranging from 60 to 500 nm can be achieved (Table 1).

Table 1. Values of various parameters for AAO formed in a different acidic media. Determined pore diameter (D_p), interpore distance (D_{int}), pore density (ρ), barrier thickness layer (t), and oxide growth rate (v) under the anodization conditions.[62,66]

Electrolyte	C	T (°C)	D_p (nm)	D_{int} (nm)	ρ (cm^{-2})	t (nm)	v (μm/h)
H_2SO_4	0.3-M	8	25-55	60	$3x10^{10}$	27	7.6
$H_2C_2O_4$	0.3-M	8	40-85	105	$1x10^{10}$	59	3.5
H_3PO_4	1 wt. %	1.4	180-240	500	$5x10^{7}$	180	2

C: concentration of electrolyte, T: temperature of electrolyte, D_p: pore diameter, D_{int}: interpore distance, ρ: pore density ($\boldsymbol{\rho} = \left(\frac{2}{\sqrt{3*D_{int}^2}}\right) * \mathbf{10^{14}}$-Eq 1), t: barrier thickness layer, v: oxide growth rate.

Several mechanisms have been proposed to explain the unique structural characteristics of AAO and the origin of self-organized pore growth with a close-packed hexagonal structure; however the exact explanation of these processes is still unclear. Based on the proposed mechanisms in the literature, one the most widely accepted mechanism is the acid-catalyzed local dissolution of the barrier oxide at the pore bottom, where significant Joule heating occurs due to concentrated electric field. This preferential barrier oxide dissolution is believed to produce an approximately hemispherical barrier layer at the metal/oxide interface while leaving an array of hexagonally arranged concave patterns on the aluminium substrate. Since the dissolution process is expected not to affect the pore walls, the resulting structure of the AAO membrane is an ordered hexagonal array of cylindrical pores with alumina walls (Figure 1).[62]

The following are the step-by-step events at the molecular level during the potentiostatic anodic oxidation of aluminium:[66]

1. Electropolishing flattens surface irregularities, and creates a large number of small pores. Some of these pores can develop into pore nuclei. Their density will decrease as the pores grow and merge as the time of anodization increases.

2. Al^{3+} ions form at the metal/oxide interface and migrate into the oxide layer.

$$Al(s) \rightarrow Al^{3+}(aq) + 3e^{-} \quad (2)$$

3. At the oxide/electrolyte interface the water-splitting reaction occurs

$$\frac{3}{2}H_2O(l) \rightarrow 3H^{+}(aq) + \frac{3}{2}O^{2-}(oxide) \quad (3)$$

The O^{2-} ions migrate (due to the influence of the electric field), from the oxide/solution interface towards the metal/oxide to form Al_2O_3.
Most of the oxide produced by Eq. 3 produces the sidewalls of the pores.

4. H^{+} ions generated by the water splitting locally dissolve the oxide:

$$\frac{1}{2}Al_2O_3(s) + 3H^{+}(aq) \rightarrow Al^{3+}(aq) + \frac{3}{2}H_2O(l) \quad (4)$$

5. H^{+} ions can also migrate toward the cathode, where they leave the cell as H_2 gas, completing the circuit:

$$3H^{+} + 3e^{-} \rightarrow \frac{1}{2}H_2(g) \quad (5)$$

For a charge balance, the rates of Eq. 2 and Eq. 5 must be equal.

6. Eq. 4 occurs preferentially where the electric field is the highest (at the pore bottom), *i.e.* at the centre or close to the centre of the pore bottom and keeps the barrier oxide thin. Since the pore walls are uniform through their entire length, the key growth step must be near the pore bottom, probably very close to the circle of intersection between the

cylinder of the pore wall and the spherical segment of the pore bottom. At this circle of intersection the water-splitting reaction (Eq. 3) must occur. As a result the porous oxide can grow, by Al^{3+} ions originating from below and by O^{2-} from the sidewalls.

7. As the anodization starts, the electric field at the oxide/electrolyte interface should be greater at the sites where the native oxide coverage is thinner or else the metal/oxide interface flattens out initially, so that the oxide layer is thicker in some parts of the surface allowing the electric field to concentrate where the oxide layer is thinner. As the pore growth continues, a curved metal/oxide interface is maintained or re-established at the pore bottom, to match the curved oxide/electrolyte interface. Once small pores have formed, the acid as well as the electric potential penetrate into a pore, and the growth becomes self-sustaining (Figure 2).

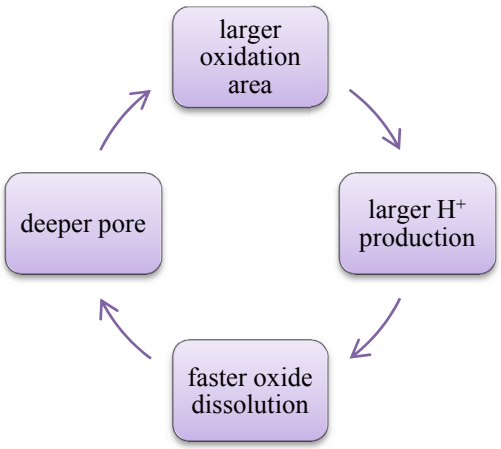

Figure 2. Self-organizing mechanism for AAO pore formation. The higher oxidation rate of a deeper pore induces the formation of more H^+ ions as consequence of the higher electric field. The larger amount of H^+ ions accelerates the dissolution of the oxide, resulting in an accelerated advancement of the deeper pore. Cyclic repetition of these steps results in self-organization of AAO pores.[67]

If the pores are initially not ordered, then a horizontal mobility of ions in the barrier layer allows reordering of the pore, until an equilibrium hexagonal arrangement is reached.[61-64,66,68]

1.3.2 Sol-gel processing

Oxide particles in colloidal dispersions are usually synthesized by sol-gel processing. Sol-gel processing is a wet chemical route for the synthesis and processing of inorganic and organic-inorganic materials, particularly oxides and oxide-based materials. An appropriate sol-preparation procedure yields solid nanoparticles with the desired stoichiometric chemical composition. Sol-gel processing offers many advantages, such as a low processing temperature and molecular-level homogeneity, and is therefore particularly useful in making complex metal oxides and temperature-sensitive organic-inorganic materials.[4,8,53,69]

Typical sol-gel processing consists of the hydrolysis and condensation of precursors. Precursors can be metal alkoxides or inorganic or organic salts. Organic or aqueous solvents can be used to dissolve precursors, and catalysts are often added to promote hydrolysis and polycondensation reactions:[69]

Hydrolysis:

$$M - OR + HOH \rightarrow M - OH + ROH \quad (6)$$

Polycondensation:

$$M - OR + M - OH \rightarrow M - O - M + ROH \quad (7)$$

$$M - OH + M - OH \rightarrow M - O - M + HOH$$

oxo bridge

building blocks of the inorganic network

Where M-OR stands for metal alkoxide and M is Ba, Sr, Ca, Pb, *etc*. and OR is organic group from alkoxide.

Hydrolysis (Eq. 6) and polycondensation (Eq. 7) reactions are both multiple-step processes, occurring either sequentially and in parallel. Condensation results in the formation of nanoscale particles of metal oxides and hydroxides, usually with organic (OR) groups attached to them. These organic groups may be due to incomplete hydrolysis, or introduced as non-hydrolyzable organic ligands. The size of the nanoscale particles, along with the morphology and microstructure of the final product, can be tailored by controlling the hydrolysis and polycondensation reactions.[69]

The greatest advantage of sol-gel processing is the ability to synthesize and process complex metal oxides. This requires careful control of the hydrolysis and polycondensation reactions of the constituent precursors. The constituent materials should be homogeneously mixed at the molecular level with a desired stoichiometry of nanoparticles. The problem arises from the fact that each precursor has a different chemical reactivity and therefore the hydrolysis and polycondensation reaction rates can differ significantly from one to another. Consequently each precursor can form nanoparticles of a mixed simple metal oxide in the sol instead of forming the desired complex metal oxide. There are several routes to avoid or prevent this homo-condensation and achieve a homogeneous mixture of multiple components at the molecular level. The most common approaches are the modification of precursors, use of complex precursors, partial hydrolysis and multistep hydrolysis and condensation. Another problem that should be taken into account is that the constituent precursor may act as a catalyst to another precursor and as result the hydrolysis and condensation reaction rates can be different from those where the precursors are processed separately.

To form organic-inorganic materials the organic components can be incorporated into an oxide system by sol-gel processing. There are several ways to accomplish this. One is to copolymerize or co-condense both inorganic and organic precursors and as a result the formed organic-inorganic hybrids are a single-phase material, in which the inorganic and organic components are linked by through chemical bonds. Another approach is to trap the organic components inside the inorganic or oxide network, by homogeneously dispensing the organic components in the sol or by infiltrating the organic molecules into the gel network.

In sol-gel processing, very little attention has been paid to the control of the crystallization or the formation of the crystalline material, which is desired for some applications. Matsuda *et al.* have demonstrated that it is possible to form the crystalline phase of $BaTiO_3$ without high-temperature sintering simply by controlling the processing parameters, including concentrations and temperature.[70] Nevertheless, there is insufficient knowledge on the control of the crystallization of complex oxides during sol synthesis and processing. Monodisperse nanoscale particles of various oxides, including complex oxides, organic-inorganic hybrids and biomaterials, can be synthesized by careful control of the sol synthesis and processing. The most important matter is to promote a simultaneous homogeneous nucleation, followed by the diffusion-controlled growth.[4,71,72] In the sol, nanoparticles synthesized by hydrolysis and polycondensation reactions typically have a size ranging from 1 to 100 nm and the particle size can be varied by changing the concentration and aging time.[69] Nanoparticles formed in this manner have many applications in nanostructured material synthesis and

processing. For example, they can be building blocks for the formation of photonic band-gap crystals,[73] or for the use in optical applications in the form of various core-shell structures.[74]

Like in other colloidal systems, gravity in a sol is an insignificant factor, whereas Brownian motion plays an important role. Nanoparticles possess a large surface area versus the volume ratio and therefore a large surface energy and consequently there is a strong tendency for such particles to agglomerate. To prevent agglomeration in a sol two types of mechanisms are available, such as steric or polymeric stabilization and electrostatic stabilization (Figure 3). The mechanism of polymeric stabilization is the adsorption of polymeric molecules onto the nanoparticle surface and spatial exclusion then prevents two nanoparticles from getting close enough to agglomerate. Electrostatic stabilization is based on the surface charge of nanoparticles in a sol. The surface charge will interact with other charged species (named counter-ions) in the sol to form a charged structure around the particle, which in turn introduces an energy barrier to prevent two particles from approaching one another. An electrosteric stabilization is therefore a mechanism which combines both a steric and an electrostatic mechanism, where the electrostatic effect is due to the surface charge of the particle or an uneven charge distribution in the polymer molecules.[4,8,75-77]

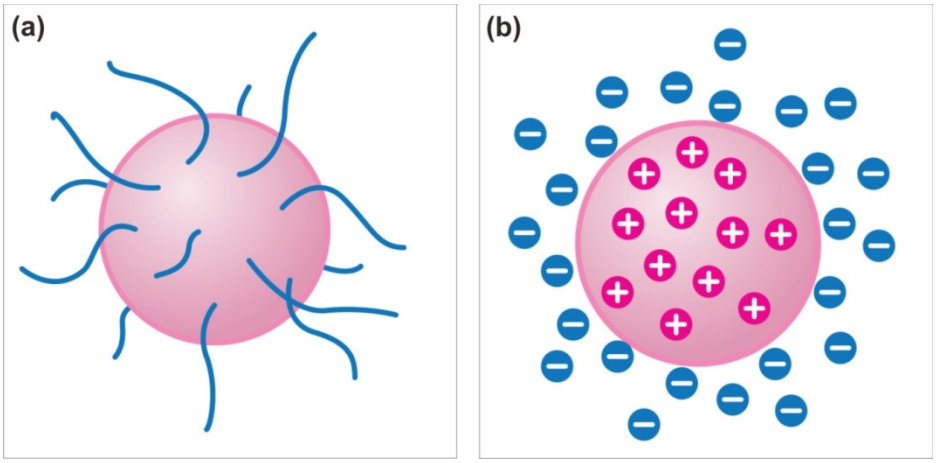

Figure 3. Schematic illustration of (a) steric stabilization and (b) electrostatic stabilization.[75]

A sol is a very dilute system and typically consists of 90% or more solvent by volume.[69] As a consequence there can be a significant amount of shrinkage upon drying and severe cracking can be observed during the synthesis of thin films. The formation of cracks can limit the synthesis of thin films by sol-gel processing, but does not have such a strong effect on the synthesis and processing of nanostructured materials. Another resulting problem could be that the product is highly porous and that sol-gel processing usually yields amorphous oxide materials. Therefore, high-temperature treatment is often required to obtain dense and crystalline materials.[4,8,75]

1.3.2.1 Surface charge density

As mentioned in the previous section, nanosized particles in sols can be stabilized by electrostatic or electrosteric mechanisms. The surfaces of nanoparticles, when they are dispersed in a polar solvent or electrolytic solution, develop an electrical charge via one or more of the following mechanisms:

- Preferential adsorption of ions
- Dissociation of surface-charged species
- Isomorphic substitution of ions
- Accumulation or depletion of electrons at the surface
- Physical adsorption of charged species (such as polymers) onto the surface

A fixed surface electrical charge density or surface potential, E, can be established for a given solid surface in a given liquid medium.[4,8,75-77]

$$E = E_0 + \frac{R_g T}{n_i F} ln a_i \qquad (8)$$

The electrical charge density is given by the Nernst equation, where E_0 is the standard electrode potential, n_i is the valence state of the ions, a_i is the activity of ions, R_g is the gas constant, T is the temperature and F is Faraday's constant. Eq. 8 shows that the surface potential of solids

varies with the concentration of ions in the surrounding solution and therefore can be either positive or negative.

The surface charge of oxides mainly results from the preferential dissolution or deposition of ions. Charge-determining ions are the ions adsorbed on the solid surface and in oxide systems the charge-determining ions are typically protons and hydroxyl groups. Their concentration can be described by pH.

$$pH = -log[H^+] \tag{9}$$

Surface charge density changes from positive to negative and vice versa, as the concentration of the charge-determining ions changes. The zero point charge (z.p.c.) is determined as the concentration of charge-determining ions corresponding to a neutral charged surface. At pH > z.p.c., the oxide surface is negative, since the surface is covered by OH^- groups and at pH < z.p.c. H^+ is the charge-determining ion and the surface is positively charged. E can now be simply related to the pH and the Nernst equation can be written as:

$$E = \frac{2.303 R_g T[(z.p.c.) - pH]}{F} \tag{10}$$

And at room temperature the above term can be simplified to:

$$E \approx 0.06[(z.p.c.) - pH] \tag{11}$$

1.3.2.2 Electrical double layer

When the surface charge density of an oxide surface is established, there will be an electrostatic force present in the suspension between the oxide surface and counter-ions which have an opposite sign to the charge-determining ions. Charge neutrality is maintained in a system but the distributions of the charge-determining ions and counter-ions in the proximity of the solid surface are inhomogeneous and very different. The distributions of both ions are mainly controlled by a combination of the following forces:[4,75-77]

- Electrostatic force
- Entropic force or dispersion
- Brownian motion

The combination of these forces results in such a way that the concentration of counter-ions near the oxide surface is the highest and this decreases with the increasing distance from the surface. The concentration of charge-determining ions changes in the opposite manner. This inhomogeneous distributions of ions in the vicinity of the oxide surface leads to the formation of the so-called electrical double-layer structure, which is schematically presented in Figure 4.

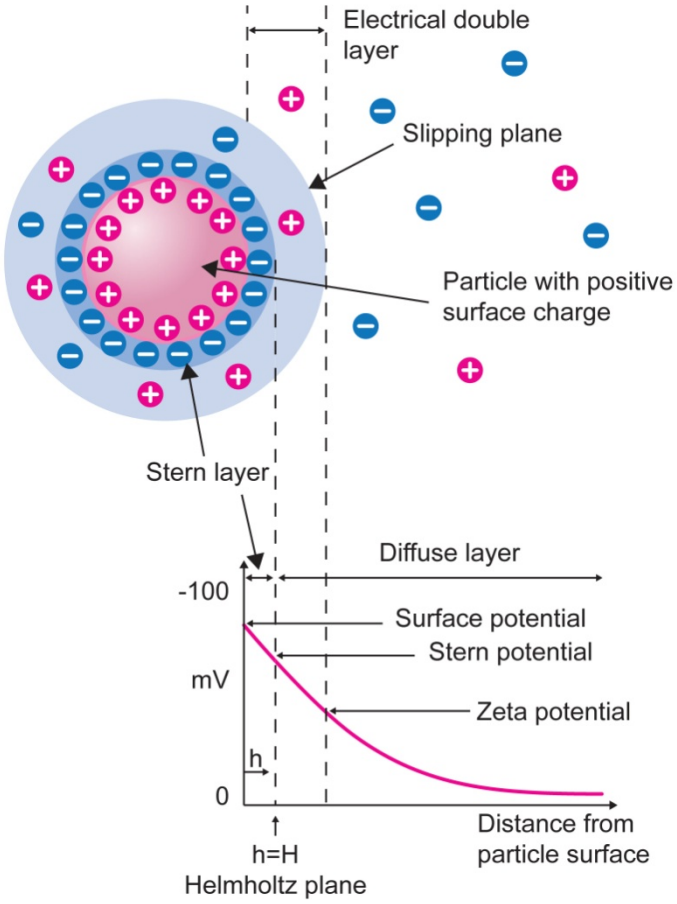

Figure 4. Schematic illustration of electrical double-layer structure and the electric potential near the solid surface with Stern and diffuse layers. Surface charge is positive.[4,8,75]

The double layer consists of two layers, named the Stern layer and the diffuse double layer. Those two layers are separated by the Helmholtz plane (H). Between the solid surface and the Helmholtz plane is the Stern layer and there the electrical potential drops linearly through the tightly bound layer of solvent and counter-ions. Behind the Helmholtz plane until the counter-ions reach average concentration in the solvent is the diffuse double layer. Here, the counter-ions diffuse freely and the electrical potential does not reduce linearly but follows an exponential relationship:

$$E \propto e^{-\kappa(h-H)} \quad (12)$$

Where h ≥ H, which is the thickness of the Stern layer. κ is the Debye-Huckle parameter and 1/κ is used to describe the double-layer thickness or Debye length. κ is given by:

$$\kappa = \sqrt{\frac{F^2 \sum_i C_i Z_i^2}{\varepsilon_r \varepsilon_0 R_g T}} \quad (13)$$

Where F is Faraday's constant, ε_0 is the permittivity of vacuum, ε_r is the dielectric constant of the solvent and C_i and Z_i are the concentration and valences of the counter-ions of i-type. This equation shows that the electric potential near the oxide surface decreases with the increasing concentration and valence state of the counter-ions, and increases with an increasing dielectric constant of the solvent. If the concentration and the valence state of counter-ions would are, then the thickness of both the Stern layer and the diffuse double layer is reduced. It has been reported that the approximate thickness is usually 10 nm or more.[4,8,75,76]

When spherical particles are dispersed in a solution and the distance between two particles is large enough so that the charge distribution on the particle surface is not influenced by the other particles. The electrostatic repulsion between two particles arises from electric surface charges, which are attenuated to a varied extent by the double layers. There will be no overlap of two double layers when the particles are far apart. In this case the electrostatic repulsion between two particles is zero. When two particles approach each other, double layers overlap and repulsive force develops.

When particles are small, such as nanosized particles dispersed in a sol, then van der Waals attraction forces and Brownian motion play important roles, whereas the influence of gravity becomes negligible. The van der Waals force is a relatively weak force compared to normal chemical bonds and becomes significant only for very small particles brought to a very short distance. On the other hand, Brownian motion ensures the nanosized particles are colliding with each other all the time. The combination of both forces results in the formation of agglomerates of nanoparticles. To prevent agglomeration electrostatic repulsion or steric exclusion is applied.

1.3.2.3 DLVO theory

The combination of van der Waals attraction (V_A) and electrostatic repulsion (V_R) is the total interaction between two particles that are electrostatically stabilized.[4,8,57,75-78]

$$V = V_A + V_R \qquad (14)$$

The electrostatic stabilization in suspensions has been described by the DLVO theory established by Derjaguin, Landau, Varwey and Overbeek. The interaction between two particles in a suspension is a combination of both van der Waals attraction potential and electrostatic repulsion potential. The DLVO theory is very useful in explaining the interactions between two approaching particles, which are electrically charged and is widely accepted in the community of colloidal science.[4]

Figure 5 shows the van der Waals attraction potential, electrostatic repulsion potential and the combination of two opposite potentials as a function of the distance from the surface of a spherical particle. The potential of both, the van der Waals attraction potential and the electrostatic repulsion potential, reduces to zero far from the oxide surface. A minimum in the potential energy, produced by the van der Waals attraction is close to the surface, whereas the maximum, also known as the repulsive barrier, is located further away from the oxide surface where electrostatic repulsion potential dominates over the van der Waals attraction potential.

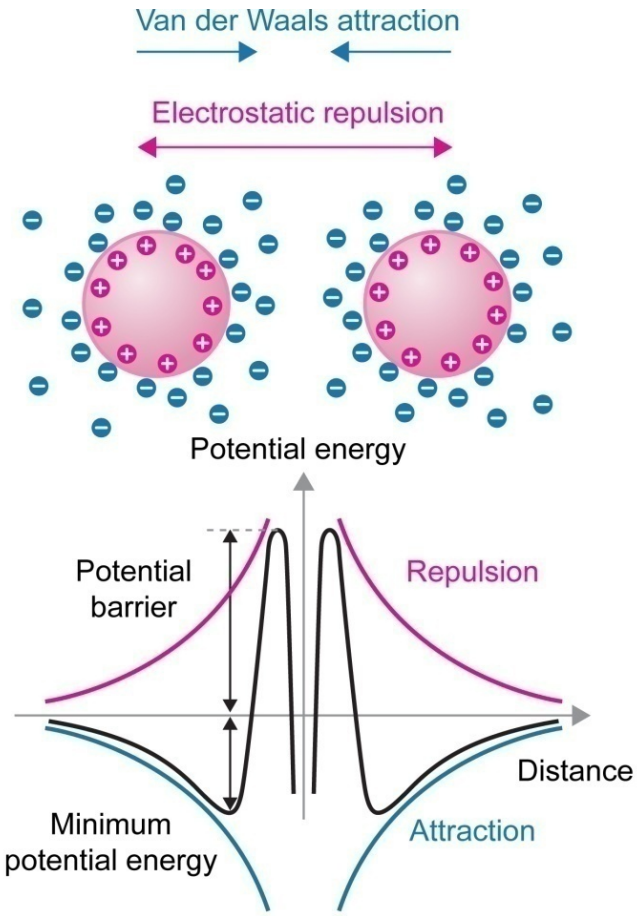

Figure 5. Schematic illustration of the DLVO potential: total potential energy versus interparticle distance.[4,75-78]

When the maximum potential energy is large enough compared to the thermal energy (k_BT, where k_B is the Boltzmann constant) of the particles the system should be stable. The system is stable when the barrier is greater than ~$10k_BT$.[4] The electrostatic potential is dependent on the concentration and valence state of the counter-ions as given in Eq. 5 and 6. On the other hand, the van der Waals potential is almost independent of the concentration and the valence state of the counter-ions. This is why the overall potential is strongly influenced by the concentration and valence state of the counter-ions.

There would be no interaction between the two particles if they were far apart from each other or the distance between surfaces of those two particles would be larger than the combined thickness of electric double layers of the two particles. Also, there would be no overlap of the diffusion double layers (Figure 6(a)). But when two particles move closer to each other and the two electric double layers overlap, a repulsion force is developed. By reducing the distance between the two particles the repulsion increases. The maximum is reached when the distance

between two particle surfaces is equal to the distances between the repulsive barrier and the surface (Figure 6(b)).

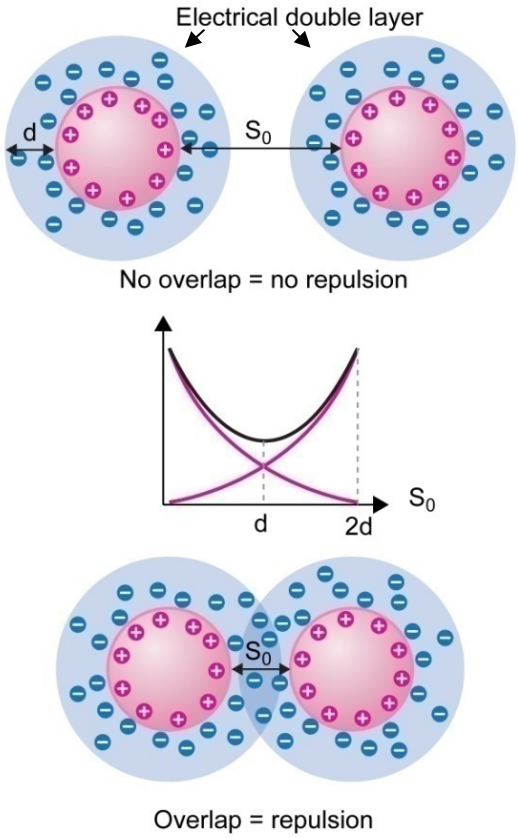

Figure 6. Schematic illustration of the conditions needed for the occurrence of the electrostatic repulsion between two particles. (a) No repulsion between particles and (b) existing repulsion between particles. S_0 is the distance between the surfaces of two particles.[4,8,75-78]

The repulsion force between two particles can be explained in two ways:[4,8,75-78]

1. The repulsion force develops when the distance between the two particles is shorter than the width of the two double layers. It should be noted that the repulsion is not directly due to the surface charge on the solid particles, but it is the interaction between the two double layers.

2. The second explanation is the osmotic flow. When two particles approach one another, the concentration of ions between two particles where double layers overlap increases. Therefore, the original equilibrium concentration profiles of counter-ions and surface-charge-determining ions are destroyed. To restore these original equilibrium concentration profiles, more of the solvent needs to flow into the region where the two double layers overlap. Such a flow of the solvent is called osmotic flow and it prevents two particles from approaching one another. The osmotic force then disappears when the distance between two particles equals, or becomes larger than, the sum of the thickness of the two double layers.

1.3.3 Direct template filling

The most straightforward and common technique when using templates to process nanorods and nanotubes is direct template filling. A liquid precursor or precursor mixture such as a sol-gel can be used to fill the pores of the template where the pores can only be filled from the bottom up. There are several drawbacks in applying this method, such as:

- To permit the penetration and complete filling of the sol-gel into the pores, the wetability of the template pores should be considered. For filling at low temperatures the pore surface can be modified to be either hydrophobic or hydrophilic by introducing a monolayer of organic molecules.
- The template materials should be chemically inert.
- Control of the shrinkage during solidification is required. If the adhesion between the pore walls is weak or if the solidification starts at the centre or from one end of the pore, nanorods are formed. In contrast, if the adhesion is strong or if the solidification starts at the interfaces and proceeds inwardly then the nanotubes are formed.

Direct template filling was often used for studying the formation of various oxide nanorods and nanotubes. The preparation procedure is the following. Colloidal dispersions are prepared using appropriate sol-gel processing. The templates, such as polycarbonate membranes (PC) or anodic aluminium oxide membranes (AAO), are dipped directly into the sol and the only driving force to fill the pores of the template with the sol is the capillary action. After the pores are filled with sol the annealing at elevated temperatures is introduced. The annealing serves for removing of the PC template and for densification of the sol-gel material. The morphology of the material is controlled by the shape of the pores within the template, while any aggregation of the material is blocked by the pore walls of the template. Since the template contains a high density of pores, a large number of nanotubes or nanorods with the same morphology can easily be synthesized at the same time.[9,11,30,50,79-84] The nanorods and nanotubes synthesized by direct template filling are generally polycrystalline or amorphous.[4,67]

Using the direct-template-filling approach, Sigh and Krupanidhi synthesized $Ba_{0.6}Sr_{0.4}TiO_3$ nanotubes in AAO templates with pores of 200 nm diameter,[84] while Hernandez *et al.* processed $BaTiO_3$ and $PbTiO_3$ nanostructures.[85] Martin *et al.* extensively reported on other materials that have also been processed by this method, such as TiO_2, MnO_2, V_2O_5 and ZnO.[52] Slight modifications of this direct-template-filling approach have also been reported. For example Chen *et al.* produced $SrTiO_3$ and $BaTiO_3$ nanotubes by liquid-phase deposition of an aqueous solution into AAO template membranes without the application of an external electric field. By varying the solution pH, concentration of the precursor and depositing temperature they optimized the (Sr, Ba)/Ti ionic ratio in order to produce stoichiometric polycrystalline titanate nanotubes.[50] Hsu *et al.* fabricated $PbTiO_3$ using an aqueous solution instead of a sol solution to fill the pores of AAO or PC templates,[86] while Wen *et al.* reported on the processing of SiO_2, TiO_2 and PZT nanorods by a combination of sol-gel processing and centrifugation.[87] In this case the centrifugal force drives the sol into the pores of the PC template, which resulted in the formation of nanorods.

1.3.3 Electrophoretic deposition mechanism

The electrophoretic deposition (EPD) technique has been extensively explored, particularly in the film deposition of ceramic materials from colloidal dispersions. As already mentioned in previous sections, the nanosized particles in colloidal dispersions, including sols, can be stabilized by electrostatic or electrosteric mechanisms. When they are dispersed in a polar solvent or an electrolyte solution, the surfaces of the nanoparticles can develop an electrical charge via one or more of the following mechanisms:[4,8,75-78]

- preferential dissolution or deposition of charges or charged species,
- preferential reduction or oxidation,
- adsorption of charged species such as polymers.

Charged surfaces will electrostatically attack oppositely charged species (counter-ions) in a sol. Thus, the so-called double-layer structure would be formed, which results after a combination of Brownian motion, electrostatic forces and osmotic forces. The double layer was already discussed in detail in the previous section and is schematically presented in Figure 4, showing a positively charged particle surface, the concentration profiles of negative ions (couter-ions) and positive ions (surface-charge determining ions) and the electric potential profile. The concentration of the negative ions (counter-ions) gradually decreases with distance from the particle surface, whereas the concentration of charge-determining ions increases, while the electric potential decreases with distance. In the region known as the Stern layer, the electric potential decreases linearly, and outside the Stern layer, the decrease is exponential. The region between the Stern layer and the point where the electric potential equals zero is called the diffusion layer. The Stern and diffusion layer together are called the double-layer structure in the classic theory of electrostatic stabilization.[4,8,57,75-78]

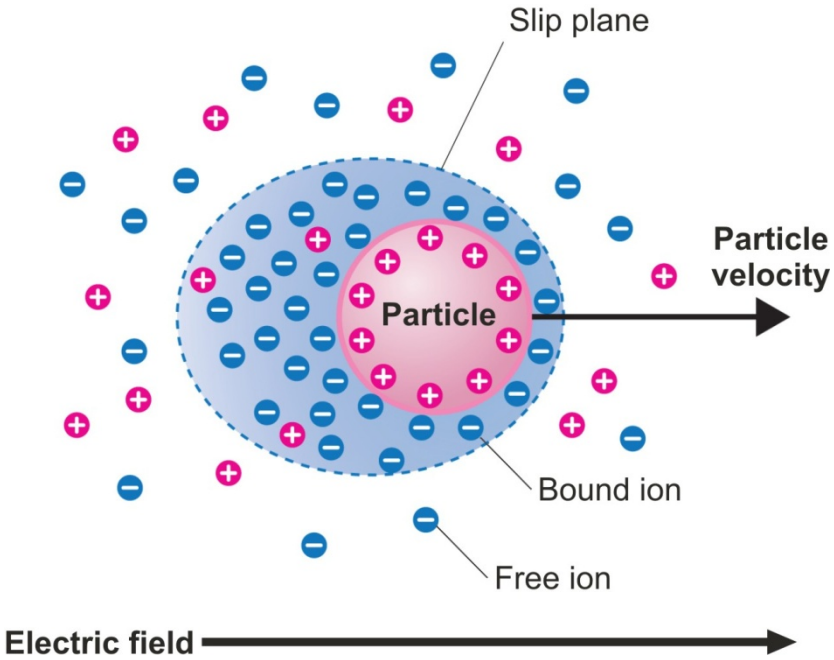

Figure 7. Schematic illustration of the electrophoresis of a positively charged particle in a sol, demonstrating the motion in the direction of the applied field.[4,75,76]

When an external electric field is applied to a sol, charged particles are set in motion in response to the applied electric field (Figure 7). This type of motion is referred to as electrophoresis. When a charged particle is in motion, some of the solvent surrounding the particle will move with it, since part of the solvent is tightly bound to the particle. The slip plane is the plane that separates the tightly bound liquid layer from the rest of the liquid (Figure 7). The electric potential at the slip plane is the zeta-potential, ζ, and it is an important parameter in determining the stability of a sol. The zeta-potential is determined by a number of factors, such as particle surface charge density, the concentration of counter-ions in the solution, solvent polarity and temperature. The zeta-potential around a spherical particle can be described as:[4,8,57,75-78,88,89]

$$\xi = \frac{Q}{4\pi\varepsilon_r a(1+\kappa a)} \qquad (15)$$

Where κ is:

$$\kappa = \sqrt{\frac{e^2 \sum n_i z_i^2}{\varepsilon_r \varepsilon_0 kT}} \qquad (16)$$

Q is the charge on the particle, a is the radius of the particle out to the slip plane, ε_r is the relative dielectric constant of the medium, and n_i and z_i are the bulk concentration and valence of the i-th ion in the system. The positively charged surface results in a positive zeta-potential in a dilute system. It is worthwhile to mention that a high concentration of counter-ions can result in a zeta-potential of the opposite sign.[4,57]

The next important factor in EPD is the mobility of a nanoparticle, μ. The mobility in a sol is dependent on the dielectric constant of the liquid medium, ε_r, the zeta-potential of the nanoparticle, ζ, and the viscosity of the solvent, η. Several forms or relationship have been proposed and one of them is the Hückel equation:[57,89]

$$\mu = \frac{2\varepsilon_r \varepsilon_o \xi}{3\pi\eta} \qquad (17)$$

EPD exploits this oriented motion of charged particles to grow films or monoliths by depositing the solid particles from a sol onto the surface of an electrode, as schematically shown in Figure 8. If the zeta-potential is positive, then the particles are positively charged and the deposition of solid particles will occur at the cathode. Otherwise, the deposition will occur at the anode. At the electrodes, surface electrochemical reactions proceed to generate or receive electrons. Upon deposition on the growth surface the electrostatic double layers collapse and the particles coagulate. There is not much information on the deposition behaviour of particles at the growth surface, however some surface diffusion and relaxation is expected. Once the particles coagulate, relatively strong attractive forces, including the formation of chemical bonds develop between two particles. The films or monoliths grown from sols by EPD are principally a compaction of nanosized particles. The formed films or monoliths are porous and typical packing densities of nanoparticles (green density) are less than 74%,[4,8,57,75,90] which is also the highest packing density for uniformly sized spherical particles.[90] The green density of material formed by EPD is strongly dependent on the concentration of the particles in sols, the zeta-potential, the externally applied electric field and the reaction kinetics between the particle surfaces. A high packing

density is achieved, if the reaction is slow and the arrival of nanoparticles onto the surface is slow allowing a sufficient particle relaxation on the deposition surface.[4,57,75,90]

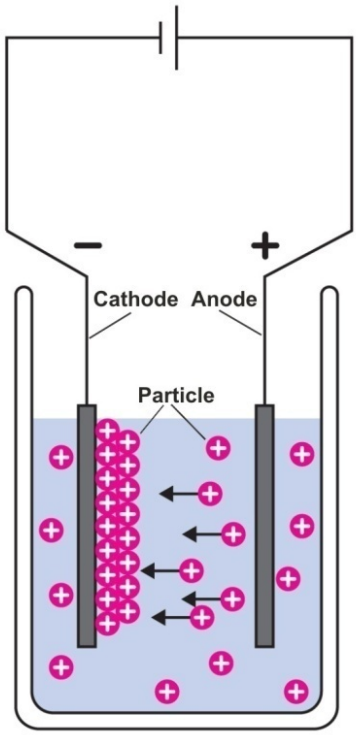

Figure 8. Schematic drawing of electrophoretic deposition cell showing the EPD process.[4,8,75-78]

Many theories have been proposed to explain the processes at the deposition surface during EPD. The electrochemical process at the surface of the electrode or at the deposition surface is complex and differs from system to system. However, an existing current during EPD indicates that reduction and oxidation reactions occur at electrodes and/or on the deposition surface. Usually films or monoliths grown by EPD are electric insulators. Nevertheless, the films or monoliths are porous and the surface of the pores would be electrically charged, just like the nanoparticle surfaces, since surface charge is dependent on the solid material and the solution. Furthermore, the pores are filled with solvent or a solution that contains counter-ions and charge-determining ions. The electrical conduction between the growth surface and the bottom electrode can proceed either via surface conduction or solution conduction. Films or monoliths grown by EPD are porous, so post-deposition annealing at elevated temperatures is required to form a dense material. If the initial solid particles are amorphous, a high-temperature treatment would also trigger crystallization.[4,8,75-78]

1.3.5 Application of template-assisted sol-gel EPD

The template-assisted sol-gel electrophoretic deposition (EPD) method provides several distinct advantages over the direct filling of the pores of the template, since it enables much denser packing of the sol particles within the pores of the template with an aid of the applied electric field. Various simple and complex oxide nanorods and nanotubes have been synthesized by template-assisted sol-gel EPD. For example, Limmer *et al.* synthesized nanorods of various oxides, such as anatase TiO_2, amorphous SiO_2, PZT, $BaTiO_3$, and layered-structured perovskite $Sr_2Nb_2O_7$.[53] They applied a combination of sol-gel and template-assisted EPD. Conventional sol-gel processing was adapted for the synthesis of various sols and by appropriate control of the sol synthesis, nanometre particles with the desired stoichiometric composition were formed, which were afterwards electrostatically stabilized by adjusting to the appropriate pH. Upon the application of an external electric field, electrostatically stabilized nanoparticles started to move and deposit on the electrode until the pores were completely filled with sol. After annealing at elevated temperatures polycrystalline or amorphous nanorods were formed. The advantage of this method is the ability to synthesize a variety of simple oxide and complex oxide materials with a desired stoichiometric composition.[8,53,54,57,81,88,91-96]

Wang *et al.* applied EPD from colloidal sols to synthesize ZnO nanorods and nanotubes. A ZnO colloidal sol was prepared by hydrolyzing an alcohol solution of zinc acetate with sodium hydroxide and a small amount of zinc nitrate as a binder. The sol was afterwards deposited into the pores at voltages from 10 to 400 V. It was observed that lower voltages led to more dense and solid nanorods, while higher voltages caused the formation of nanotubes. They proposed a mechanism, stating that higher voltages cause dielectric breakdown of the AAO template, which becomes charged similar to the cathode. In that way the electrostatic attraction between ZnO nanoparticles and the pore walls leads to the formation of nanotubes.[97-100]

Miao *et al.* prepared single-crystalline TiO_2 nanowires by template-assisted electrochemically induced sol-gel deposition, where TiO^{2+} ionic particles were prepared and deposited into the template pores. Before annealing the material was amorphous and after annealing they were obtained as single-crystalline nanowires.[101]

2 Aims and hypothesis

The synthesis and fabrication of materials with the desired structure, morphology and chemical composition on a nanoscale is an essential milestone of new materials development in the rapidly growing fields of nanoscience and nanotechnology. Namely, it has been shown that materials, when prepared on a nanoscale (nanopowders, nanotubes, nanorods, *etc.*), usually exhibit different physical properties than their "bulk" counterparts due to very large surface/volume ratio and possible confinement effects. This is why many efforts have recently been put into determining the correlation between the structure and chemical composition of nanomaterials and nanostructures with their resulting physical properties in order to process materials for various technological applications on a nanoscale. The processing of materials in various nano-morphological forms and their characterization therefore represent up-to-date research in both basic science and the research and development for new technological applications.

In view of this, the primary aims and goals of the conducted research within present my research topic were the synthesis and processing of complex oxide materials in the form of 1-D nanostructures (nanorods, nanotubes) using the electrophoretic deposition of sols into template membranes in order to produce materials with a defined shape and morphology on a nanoscale. Two important technological oxide ceramic materials with the perovskite structure, namely ferroelectric $BaTiO_3$ and dielectric $SrTiO_3$, were chosen as the target materials for the formation of 1-D nanostructures. One of the main goals was also the functionalization of obtained 1-D $BaTiO_3$ and $SrTiO_3$ nanostructures, especially in view of their potential applications for nano-sensors.

The main hypothesis was that when both $BaTiO_3$ and $SrTiO_3$ are manufactured in the form of 1-D nanostructures (nanorods and/or nanotubes), they should exhibit different physical properties due to their dimensionality and nanosize polycrystalline nature. Dimensionality plays a crucial role in determining the physical properties of nanostructures and this is why the control of the size and shape of nanoparticles is of great interest. In contrast to the size and shape control of individual nanoparticles, the aggregation of nanoparticles into more complex 1-D nanostructures is quite challenging topic. Consequently, various polycrystalline 1-D nanostructures (nanorods, nanotubes, nanowires) are becoming a more and more interesting class of nanomaterials from both the scientific and technological points of view.

The more specific aims and goals of the conducted research were as follows:

- To optimize and implement the process of anodization of an aluminium foil in order to prepare highly ordered AAO membranes with long, parallel, close-packed arrays of channels suitable as templates for forming 1-D $BaTiO_3$ and $SrTiO_3$ nanostructures.
- To compare the prepared AAO templates with other available organic membranes, such as track-etched hydrophilic polycarbonate (PC) membranes.
- To optimize the processing parameters for the most efficient electrophoretic deposition of BT and ST sols into the pores of the AAO templates in order to obtain 1-D $BaTiO_3$ and $SrTiO_3$ nanostructures with the highly uniform morphology.
- To determine the crystallization and growth mechanisms of 1-D $BaTiO_3$ and $SrTiO_3$ nanostructures within the pores of the AAO templates that favours either the formation of nanorods or nanotubes within the pores of the template during the thermal treatment.
- To assess the possibility of the preparation of 1-D $BaTiO_3$ and $SrTiO_3$ nanostructures in singlecrystalline form, *i.e.*, nanorods and/or nanotubes, by the annealing process after the electrophoretic deposition.
- To construct prototype devices made of a single nanorods or nanotubes and to measure their electrical properties and responses under different environmental conditions in order to investigate their potential use for nanosensors. In the present work single $BaTiO_3$ nanorods were tested for a humidity nanosensor, while single Fe-doped $SrTiO_3$ nanotubes were tested for UV nano-photodetectors.
- To use various analytical techniques to monitor the 1-D $BaTiO_3$ and $SrTiO_3$ nanostructure processing parameters, as well as to determine their structure and chemical composition on the micro, nano and atomic scales with a special emphasis on the use of modern electron-microscopy techniques.

3 Materials and methods

3.1 Processing and sample preparation

3.1.1 Synthesis of highly ordered anodic aluminium oxide membranes

The template membranes used for the synthesis of $BaTiO_3$ and $SrTiO_3$ 1-D nanostructures were anodic aluminium oxide (AAO) membranes produced with two step anodization process using commercially available aluminium foils as substrates (99.999%, Goodfellow, Huntingdon, England). AAO membranes were synthesized according to the procedure reported by Lee *et al.*[62] The Al foils were first cleaned in an ultrasonic bath, then in an acetone solution and finally in an ethanol solution to remove any possible oil layer or other organic layer from the Al foil surface. Otherwise this contamination layer would prevent homogeneous growth of the oxide layer on the Al foil since the contact between anode and electrolyte would be prevented. After cleaning, the foils were annealed for 3 h at 500 °C under an argon atmosphere to remove residual stresses in the material. The annealed samples were subsequently electropolished to avoid any unwanted effects caused by surface roughness. Al samples were electropolished by (Struers LectoPol-5, Ballerup, Denmark) electropolisher using an electrolyte mixture of $HClO_4$, C_2H_5OH and butylcellulose, which is commercially available as the Electrolyte A2 (Struers, Ballerup, Denmark). The parameters used for the electropolishing are given in Table 2. The as-polished Al foils were ultrasonically cleaned with ethanol and distillated water.

Table 2. Parameters for electropolishing.

Parameter	Value
area of electropolished part	2 cm^2
temperature	16 °C
voltage	48 V
flow rate	15 ml/min
time	12 s

After cleaning, annealing and electropolishing of the Al foils a two-step anodization process was conducted using an electrochemical cell equipped with a cooling stage (Lauda RE 306, Lauda-Königshofen, Germany) and a data-acquisition/switch unit (Agilent technologies 34970A, Santa Clara, USA) (Figure 9). A schematic diagram of the electrochemical cell, where the electropolished Al foil is used as the anode and Al electrode is used as the cathode, is shown in Figure 10. For both anodization steps oxalic acid solution was used as electrolyte (p.a., Aldrich, Taufkirchen, Germany). During anodization the electrolyte was cooled down to 5-7 °C. The anode and cathode were connected to a DC power supply of 40 V. Constant stirring was applied to the solution to accelerate the diffusion of the heat that generated by anodization from the sample. This treatment is important for maintaining the constant temperature in the cell and to maintain the continuous growth of the anodic oxide membrane. The anodization current and electrolyte temperature were monitored during anodization. When an external electric field is applied, the first oxide layer is formed. The higher local electric-field, existing between stripes formed during electropolishing, consequently leads to the dissolution of the oxide layer at the oxide/electrolyte interface.

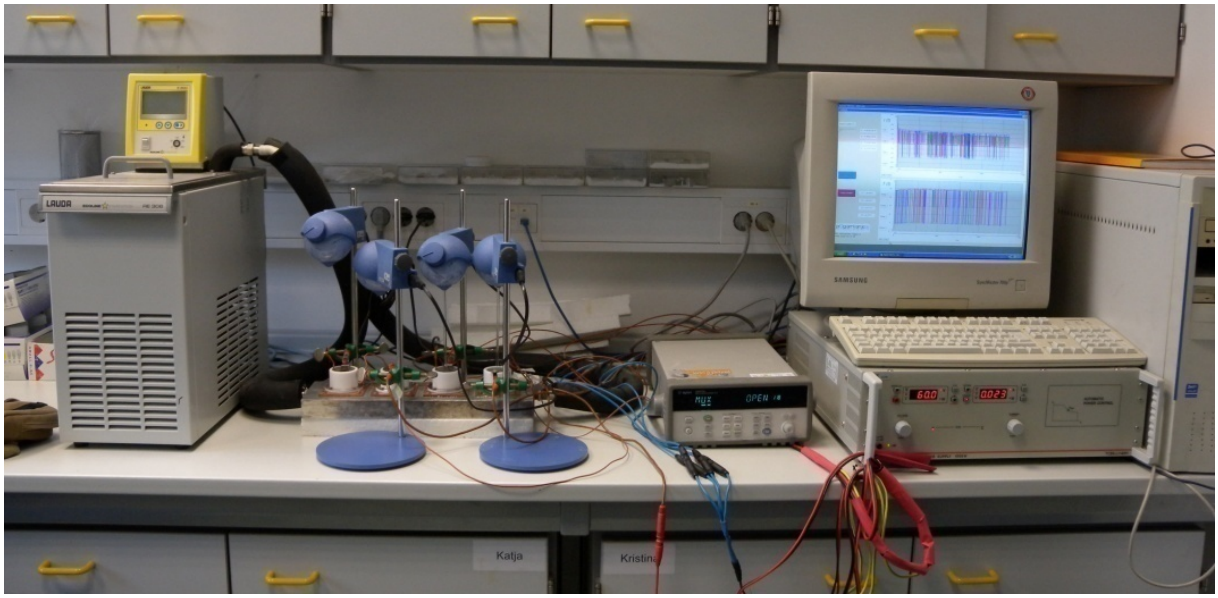

Figure 9. Anodization setup coupled with cooling stage and DC power supply. The setup was constructed for anodization of four Al foils at the same time.

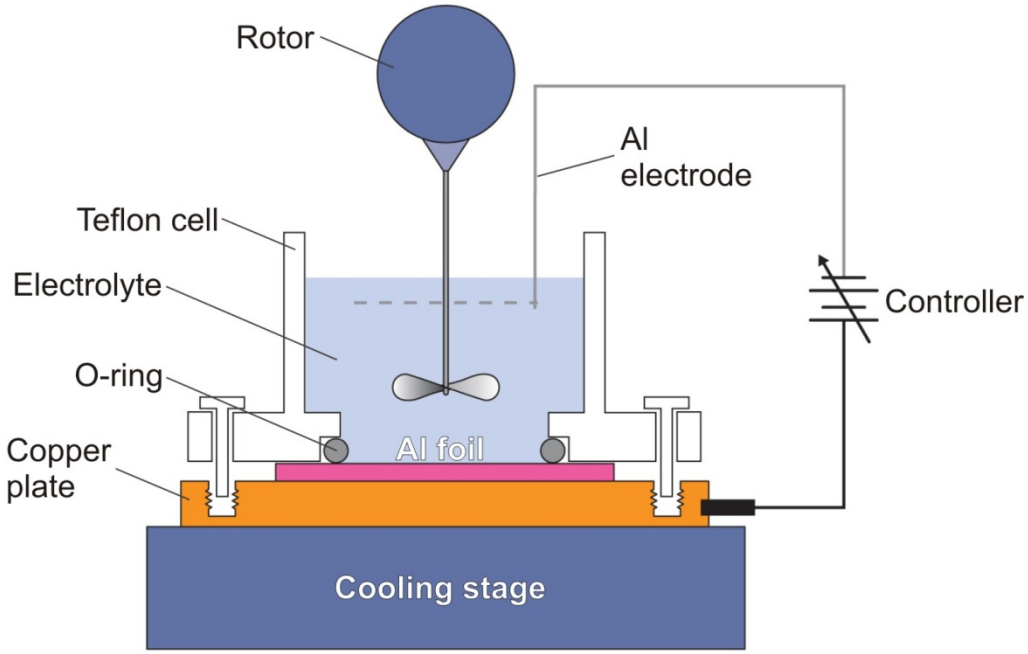

Figure 10. Experimental setup. Schematic drawing of the electrochemical cell used in the two-step anodization experiments.[62]

The first anodization step was conducted in a 0.3-M oxalic acid solution at 5-7 °C at 40 V for 24 h to obtain a continuous aluminium oxide (Al_2O_3) layer on the surface. After the first anodization step the Al_2O_3 layer was removed in a solution of 35 ml/l H_3PO_4 and 20 g/l of CrO_3 solution heated up to 80 °C for 2h. This step is necessary because pores in Al_2O_3 layer formed after first anodization are randomly distributed. By removing that layer textured Al foil is obtained which leads to production of ordered Al_2O_3 pores during the second anodization. Second anodization step was performed in a 0.3-M oxalic acid solution at 5-7 °C at 40 V for 17 h followed by selective removal of the un-anodized Al in a solution containing 1.7 g $CuCl_2$ x $2H_2O$, 25 ml 34 % HCl and 100 ml of H_2O. This process is based on the large standard reduction potential of Cu^{3+}/Cu compared to the Al^{3+}/Al pair where Al would be spontaneously oxidized into Al^{3+} when Al metal is immersed into an aqueous solution containing $CuCl_2$. The Al foil reacted exothermally with $CuCl_2$, accompanied by H_2 gas evolution. Figure 11 illustrates an experimental setup for the selective removal of the remaining Al substrate. Afterwards, selective removal of the barrier layer and a pore widening treatment were performed in 5 wt% phosphoric acid at room temperature for 4 h on AAO membranes to obtain a through-channel membrane. The as-prepared AAO membranes had pore diameters raging between 80 and 150 nm and were 15-25 μm thick.

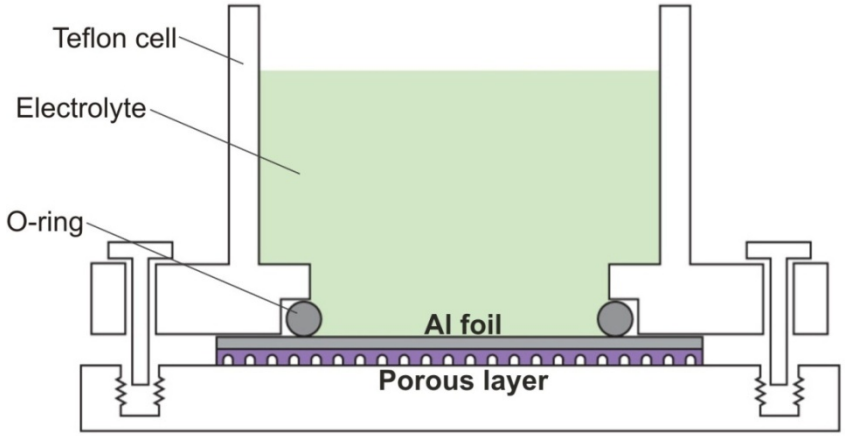

Figure 11. Schematic drawing of a setup for the selective removal of the Al substrate in a $CuCl_2/HCl/H_2O$ solution.[62]

3.1.2 Template-assisted EPD of BT sol and ST sol

Before achieving the final $BaTiO_3$ and $SrTiO_3$ 1-D nanostructures the barium titanate (BT) and strontium titanate (ST) sols were deposited into the pores of AAO templates by the electrophoretic deposition (EPD).

3.1.2.1 EPD of BT sol into the templates

Barium acetate $Ba(CH_3CO_2)_2$ (≥ 99.0 %, Fluka, Seelze, Germany) and precursor titanium (IV) isopropoxide $Ti\{OCH(CH_3)_2\}_4$ (p.a., Fluka, Seelze, Germany) were used for the synthesis of the BT sol. To prevent hydrolysis the solvents ethylene glycol (p.a., Riedel-de Haen, Seelze, Germany) and acetic acid (p.a., Fluka, Seelze, Germany) were used. Barium acetate (14.4 g) was first dissolved in glacial acetic acid (56.2 ml) by stirring at room temperature for 1 h. Then titanium isopropoxide (16.6 ml), in an amount corresponding to the molar ratio Ba:Ti=1:1, was added to the barium acetate solution during constant-rate stirring. Finally, the ethylene glycol (18.3 ml) was added as a solvent to the solution in order to adjust the viscosity and to stabilize the sol.[54] The as-prepared sol was transparent and stable for approximately one week in a dry atmosphere. The sol concentration does not have a significant influence on the deposit and allows the synthesis of solid nanorods even from very dilute sols.[57]

The barium titanate sol is after condensation reactions formed of Ba-O-Ti oxo bridges with organic groups attached to them. The formula for the sol most likely looks like this:

$$[RO - Ba - O - Ti - (OR)_3]_n \qquad (18)$$

Where -OR is organic group. For easier writing the barium titanate sol will be written as BT sol through the whole thesis.

Commercially available polycarbonate (PC) membranes (Whatman, Dassel, Germany) and a two-step anodization produced anodic aluminium oxide (AAO) membranes that were used as a template for the EPD of BT sol into the pores. Both the PC and AAO template membranes had pore diameters of approximately 150-200 nm and thicknesses of up to 25 μm. The template (PC or AAO) was attached to an aluminium working electrode with a piece of conducting tape in order to provide a conductive path between the membrane and the cathode, whereas a Pt mesh electrode was used as the counter electrode. Both electrodes were placed into the BT sol, parallel with each other at a fixed distance of 1.5 cm. The sol is initially drawn into the membrane pores by capillary action after the immersion into the sol. The EPD setup used in our experiments is shown in Figure 12 and Figure 13. For the electrophoretic deposition of the sol into the template pores potentials between 5 to 50 V were applied between the electrodes. The selected potential was then maintained for 30 min, to ensure a complete filling of the pores. The parameters used in the EPD process are given in Table 3. During electrophoretic deposition the current between the electrodes was monitored using a power supply interfaced to a computer (Agilent technologies 34970A, Santa Clara, USA).

3.1.2.2 EPD of ST sol into the templates

The procedure for the synthesis of the ST sol was similar to the synthesis of the BT sol. Strontium acetate $Sr(CH_3CO_2)_2$ (≥ 99.0 %, Fluka, Seelze, Germany) and titanium (IV) isopropoxide $Ti\{OCH(CH_3)_2\}_4$ (p.a., Fluka, Seelze, Germany) were used as precursors for the preparation of the ST sol, while ethylene glycol (p.a., Riedel-de Haen, Seelze, Germany) and acetic acid (p.a., Fluka, Seelze, Germany) were used as the solvents to prevent the hydrolysis. Strontium acetate was first dissolved in glacial acetic acid by stirring at room temperature for 1 h. Then the titanium isopropoxide, in an amount corresponding to the molar ratio Sr:Ti=1:1, was added to the strontium acetate solution during constant-rate stirring. Finally, ethylene glycol was added to the solution mixture in order to adjust the viscosity and to stabilize the sol. The as-prepared sol was transparent and stable for approximately three days in a dry atmosphere.

As for the barium titanate sol also the strontium titanate sol is after condensation reactions formed of Sr-O-Ti oxo bridges with organic groups attached to them. The formula for the sol most likely looks like this:

$$[RO - Sr - O - Ti - (OR)_3]_n \quad (19)$$

Where -OR is organic group. For easier writing the strontium titanate sol will be written as ST sol through the whole thesis.

The AAO membrane was used as a template for the EPD of ST sol into the pores. The template was attached to an aluminium working electrode with a piece of conducting tape in order to provide a conductive path between the membrane and the cathode, whereas a Pt mesh electrode was used as the counter electrode. Both electrodes were placed into the ST sol, parallel with each other at a fixed distance of 1.5 cm. The sol is initially drawn into the membrane pores by capillary action after the immersion into the sol. For electrophoretic deposition of the sol into the template pores, a potential of 30 V was applied between the electrodes. The selected potential was then maintained for 30 min, to ensure a complete filling of the pores. During the electrophoretic deposition the current between the electrodes was monitored.

Table 3. Parameters for EPD of BT sol into AAO template.

Applied voltage	Deposition time
5 V	30 min
10 V	30 min
30V	30 min
50 V	5 min

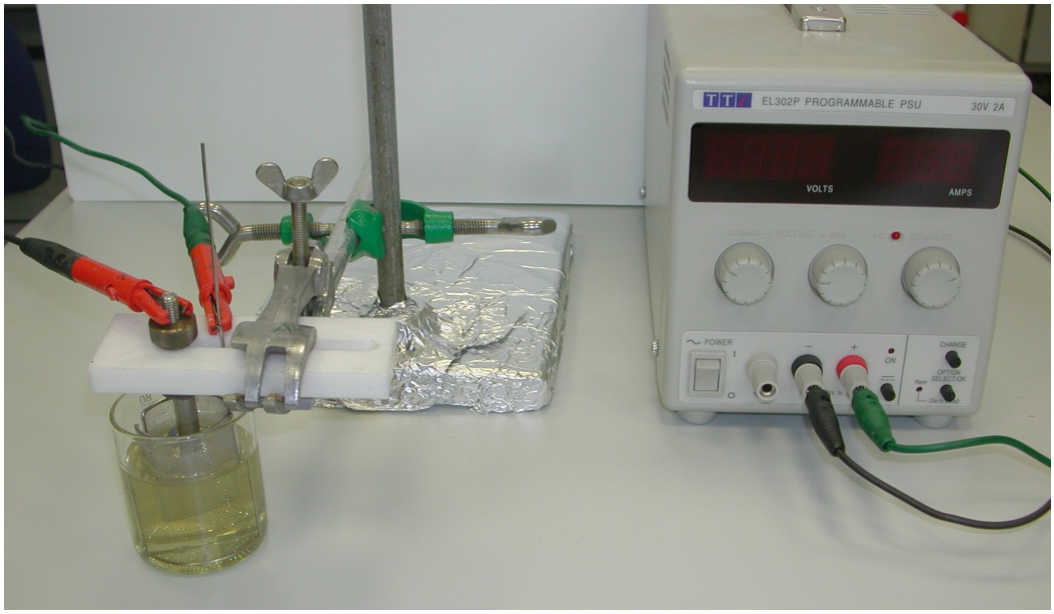

Figure 12. EPD setup coupled with DC power supply.

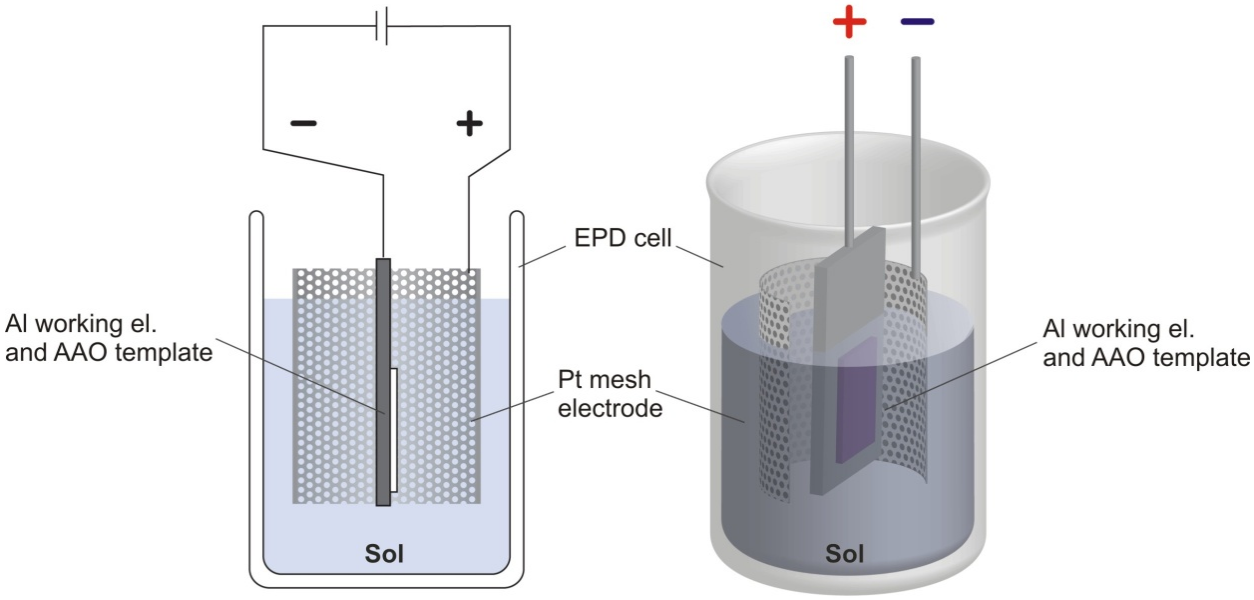

Figure 13. Schematic drawing of electrophoretic deposition cell used for formation of 1-D nanostructures by sol-gel EPD. AAO template attached on Al working electrode with a piece of conducting tape in order to provide a conductive path and Pt mesh electrode as the counter electrode. The electrodes are placed into the sol parallel with each other. And the sol is drawn into the template membrane pores by capillary action.

3.1.3 Annealing and $BaTiO_3$ and $SrTiO_3$ crystallization

After EPD of BT and ST sols into the template membranes the samples were annealed. The templates were afterwards etched away in strong base solution in order to obtain the free-standing $BaTiO_3$ and $SrTiO_3$ nanostructures 1-D (nanorods or nanotubes).

3.1.3.1 Annealing and $BaTiO_3$ crystallization

After electrophoretic deposition the samples were thermally treated in order to make the material dense and crystalline. First they were dried at 200 °C for 12 h and then annealed at temperatures from 500 to 800 °C at constant time in order to allow crystallization of the $BaTiO_3$. The annealing times at the selected annealing temperature (700 °C) were 1, 12, 24 and 48 hours. The parameters for heat treatment are given in Table 4. During heating, the PC membrane was finally burnt off, while the AAO membranes were removed after heat treatment in a 6-M NaOH solution. The obtained product finely replicated the template pores and showed a nanostructured texture. The nanostructures were repeatedly washed in water and ethanol and concentrated by centrifugation.

Table 4. Parameters for heat treatment of deposited $BaTiO_3$ material in AAO templates.

Annealing temperature at constant time	500 °C for 1 h	600 °C for 1 h	700 °C for 1 h	800 °C for 1 h
Annealing time at constant temperature	700 °C for 1 h	700 °C for 12 h	700 °C for 24 h	700 °C for 48 h

3.1.3.2 Annealing and $SrTiO_3$ crystallization

After deposition the samples were first dried at 200 °C for 12 h and then annealed at 700 °C for 1 h. A heating rate of 3 °C/min was applied in order to allow optimum crystallization of the $SrTiO_3$. After annealing the AAO membranes were removed in a 6-M NaOH solution. The obtained product finely replicated the template pores and showed a nanostructured texture. The nanostructures were repeatedly washed in water and ethanol and concentrated by centrifugation.

Synthesis of Fe-doped $SrTiO_3$ nanotubes

In addition to pure $SrTiO_3$ we also prepared Fe-doped $SrTiO_3$ nanotubes by the same procedure as the pure $SrTiO_3$ nanotubes. The iron, titanium and strontium contents in the starting sol were adjusted so that the final composition of the nanotubes after annealing would give a material with approximately 2 mol% of iron replacing the titanium in $SrTiO_3$ according to the formula $Sr(Ti_{0.98}Fe_{0.02})O_{3-y}$ (y = deviation from stoichiometry).

3.2 Characterization

3.2.1 X-ray powder diffraction

The crystal structures of the $BaTiO_3$ and $SrTiO_3$ 1-D nanostructures were determined by X-ray powder diffraction (XRD). $BaTiO_3$ nanorods or $SrTiO_3$ nanotubes were dispersed onto the Si substrates and the XRD spectra were recorded from 10° to 70° (2-theta angle) with CuK_α radiation (λ=1.5418 Å) using 0.04 2-theta degree step-scan mode (Bruker AXS Model D4, Endeavor, Wien, Austria). The spectra were identified by EVA software (version 12.0, Bruker, Wien, Austria) showing the presence of cubic $BaTiO_3$ and cubic $SrTiO_3$ after annealing the samples.

3.2.2 Raman spectroscopy

While $SrTiO_3$ exists only in its cubic form at room temperature and above, $BaTiO_3$ can crystallize in cubic, tetragonal or hexagonal modification. The tetragonal phase of $BaTiO_3$, having *4mm* symmetry with the *c*/*a* axis ratio approximately 1.01 is difficult to distinguish from the cubic phase by using diffraction techniques[102]. This is why Raman spectroscopy (RS) was applied for the structural investigations as well. In order to distinguish the $BaTiO_3$ polymorphs we used RS and the measurements were performed using a Raman spectrometer (Jobin-Yvon T64000, Horiba, Kyoto, Japan) with an argon ion laser (Coherent, Innova 400, Santa Paula, California, USA) operating at 514.5 nm for the excitation. Raman data were collected with a multi-channel CCD detector. With the aim to avoid the crystallization due to the heating in the laser beam during RS measurements, a laser power of 7 mW was applied using a 50x long working distance objective. The spectra were fitted to a Lorentzian line shape on a sloping baseline, and from this fit the integrated band intensities were determined.

3.2.3 Scanning electron microscopy

Scanning electron microscopy (SEM) was used to characterize the morphology of the AAO and PC membranes as well as the $BaTiO_3$ and $SrTiO_3$ 1-D nanostructures. The specimens for the SEM observations were prepared by placing them on an adhesive carbon conductive tape. Afterwards all specimens were coated with an approximately 2-nm-thick carbon layer to ensure electrical conductivity of the specimens in the SEM.

Samples were analyzed in a scanning electron microscope (Jeol JSM-7600F, Jeol Ltd., Tokyo, Japan) with in-lens thermal field-emission gun (FEG) and equipped with detectors for secondary electrons (SE), lower secondary electron image (LEI), backscattered electrons (BE), energy-dispersive X-ray spectroscopy (EDXS) (X-MAX, Oxford Instruments, Oxfordshire, UK), wave-length-dispersive X-ray spectroscopy (WDXS) (INCA Wave, Oxford Instruments, Oxfordshire, UK), electron backscatter diffraction (EBSD) (EBSD Channel 5, Oxford Instruments, Oxfordshire, UK) and electron lithography (XENOS Semiconductor Technologies GmbH, Kusterdingen**,** Germany)**.** Electron micrographs were obtained using SE and BE electrons for imaging at accelerating voltages of 10 and 20 kV, at a working distance of 15 mm and a specimen tilt of 0°.

3.2.4 Transmission electron microscopy

In order to study the nanoscale structure and chemistry of 1-D $BaTiO_3$ and $SrTiO_3$ nanostructures we used transmission electron microscopy (TEM).

3.2.4.1 Sample preparation

The samples for TEM observations were prepared by dispersing the nanorods or nanotubes after ultrasonic deagglomeration in ethanol onto lacy, carbon-coated nickel grids. For the preparation of cross-section samples of $BaTiO_3$ nanorods and $SrTiO_3$ nanotubes ultra-microtomy was used to prove their rod or tubular shape. The nanorods were embedded in an epoxy resin. Unclosed flat embedding moulds were used. After hardening the resins in the moulds, the hardened resin blocks were removed and were trimmed in the high-speed milling system (Leica EM-TRIM2, Leica Microsystems GmbH, Wetzlar, Germany). Then they were transferred to the ultramicrotom (Leica EM-UC6, Leica Microsystems GmbH, Wetzlar, Germany). The face to be sectioned was aligned perpendicular to the axis of the specimen holder. The rough surface after the trimming was removed by a 35° diamond blade. After that 40-70-nm-thick sections were cut with a diamond knife speed of 1 mm/s at a cleavage angle of 6°.[103,104] Finally, the cut sheets were picked up and placed on lacy carbon-coated copper grids and examined in a TEM.

For the quantitative EDXS analyses of the nanostructures, pure, stoichiometric $BaTiO_3$ nanosized powder was used as a standard reference material. The experimental k-factors were calculated from 10 EDXS spectra acquired from the $BaTiO_3$ standard. These k-factors were then used to quantify the EDXS spectra from our samples using the Cliff-Lorimer procedure.[105]

3.2.4.2 Imaging and spectroscopy

The following two electron microscopes were used to study nanocale structure, ordering and chemical composition of produced 1-D $BaTiO_3$ and $SrTiO_3$ nanostructures.

1. The TEM (Jeol JEM-2100, Jeol Ltd., Tokyo, Japan) microscope with LaB_6 filament operating at 200 kV and equipped with EDXS detector (JED 2300T Jeol Ltd., Tokyo, Japan) and CCD camera (Orius DC1000, Gatan Inc., Pleasanton, USA).
2. The TEM (Jeol JEM-2010F TEM/STEM with a field-emission gun, Jeol Ltd., Tokyo, Japan) operating at 200 kV and equipped with a Si(Li) EDXS detector (Link ISIS 300, Oxford Instruments, Oxfordshire, UK), scanning unit with a bright-field (BF), dark-field detector (DF) and high-angle annular dark-field detector (EM-24140 YDF-Yap, Jeol Ltd., Tokyo, Japan), EELS (PEELS Model 677, Gatan Inc., Pleasanton, USA), and CCD camera (Orius SC1000C, Gatan Inc., Pleasanton, USA).

For tomography the TEM/STEM electron microscope (FEI Technai F20, FEI, Eindhoven, Netherlands) with field-emission gun (FEG) operating at 200kV was used. This microscope has a SuperTwin objective lens with a Cs of 1.2 mm and it is equipped with a Gatan Imaging Filter (GIF) 200, fitted with a 1k x 1k CCD camera, for energy-filtered diffraction, imaging and EELS; an EDAX r-TEM ultra-thin window (UTW) X-ray detector; Off-axis STEM bright-field (BF) and dark-field (DF) detectors and On-axis high sensitivity (single electron detection) Fischione Model 3000 high-angle annular dark-field (HAADF) detector for high-resolution Z-contrast imaging.

Electron tomography studies were performed using a tomography holder (Fischione 2040 Dual-Axis, FEI, Eindhoven, Netherlands) in the tilt range of -74º to +72º, with images recorded every 2º, and the tilt-series acquired in HAADF-STEM mode (inner angle of detector = 35 mrad). TEM parameters such defocus, image shift, specimen tilt, and the condenser lens astigmatism were controlled during the acquisition of the tilt series of projections. Once the acquisition of the tilt series was completed, images were spatially aligned by a cross-correlation algorithm using Inspect3D software (FEI, The Netherlands), and 3D reconstructions were achieved using a simultaneous iterative reconstruction algorithm (SIRT), 20 iterations, of consecutive 2D slices. Visualization was performed using software (AMIRA 3.1, Mercury Computer Systems).

3.2.5 Nanodevice fabrication - FIB contacting

For electrical DC measurements on individual $BaTiO_3$ nanorods and Fe-doped $SrTiO_3$ nanotubes, they were contacted with focused ion beam (FIB) nanolithography in order to produce $BaTiO_3$ and Fe-doped $SrTiO_3$ nanodevices.

The $BaTiO_3$ nanorods and/or Fe-doped $SrTiO_3$ nanotubes were dispersed over the surface of the SiO_2/Si substrates with photolitographically pre-patterned Ti/Ni/Au microelectrodes. The as-dispersed nanostructures were electrically contacted using a FIB (FEI Dual-Beam Strata 235 instrument, FEI, Eindhoven, Netherlands) combined with a tri-methyl-methylcyclopentadienyl-platinum [$(CH_3)CH_3C_5H_4Pt$] injector to deposit the platinum. The platinum was deposited using both ion- and electron-assisted deposition. The electron and gallium ion beams were accelerated to 5 and 30 kV, respectively. Since the interaction between the accelerated electrons and sample is less destructive than the interaction with ions, platinum metal stripes were first electron-assisted deposited from the nanostructure to a certain distance. Afterwards, ion-assisted deposition was used to extend the electron-assisted contacts to the pre-patterned contacts. The reason for this is that the deposition rate is higher and in this way undesired surface damage and structure modification of the nanostructure can be avoided.[106-108]

Using the Dual-Beam FIB-FSEM as a conventional SEM, suitable $BaTiO_3$ or Fe-doped $SrTiO_3$ nanostructures were selected. All the selected nanorods or nanotubes had lengths between 5-20 μm and diameters of approximately 200 nm. An example of a selected and contacted $BaTiO_3$ nanorod is shown in Figure 14. The first contacts on top and near the nanorod were fabricated with the use of electrons (Figure 14(a)), and from them, the ion-beam induced deposition is used to extend the stripes to the pre-patterned contacts (Figure 14(b) and (c)). The Fe-doped $SrTiO_3$ nanodevice produced by FIB nanolithography is shown in Figure 15.

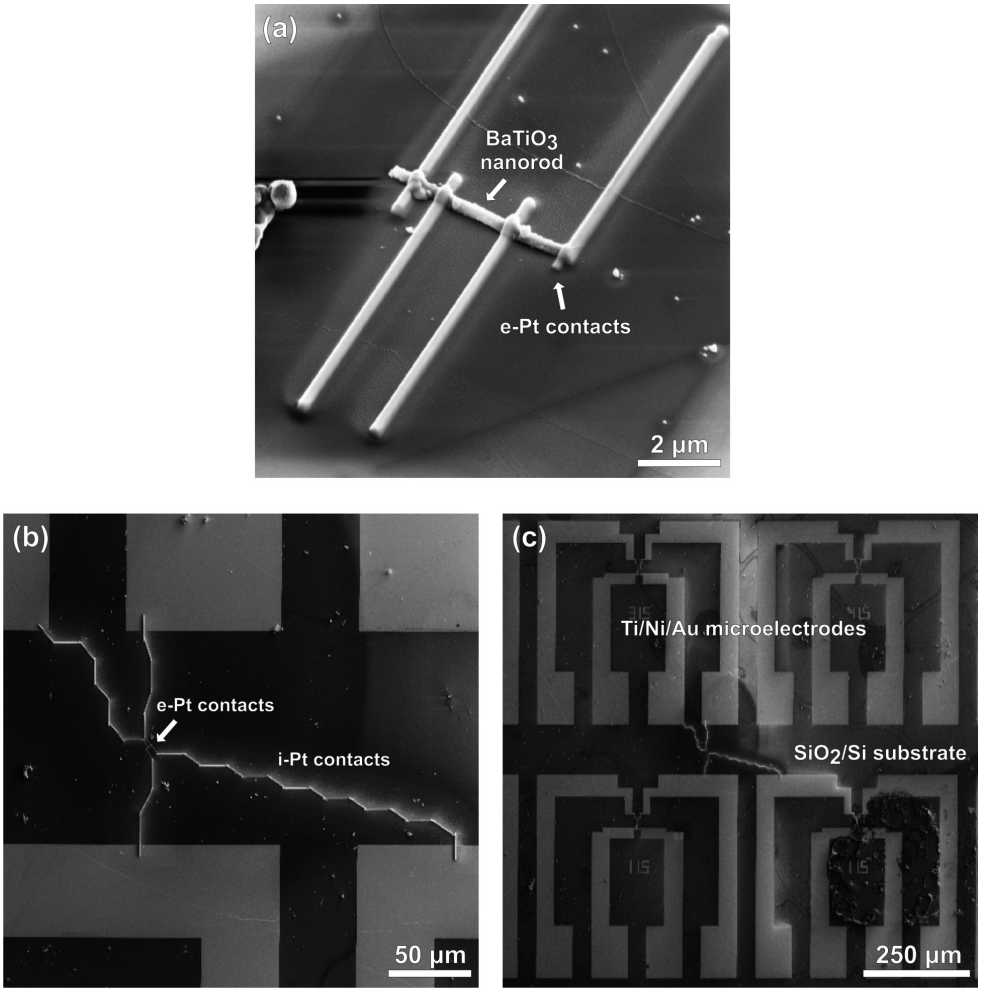

Figure 14. $BaTiO_3$ nanorod with diameter of 200 nm and length of 6 µm contacted with Dual Beam FIB lithography. (a) Higher-magnification image of $BaTiO_3$ nanorod contacted with platinum electron-assisted deposition. (b) Combination of both platinum ion- and electron-assisted deposition. (c) General view of the contacted nanorod and the contacts to Ti/Ni/Au microelectrodes.

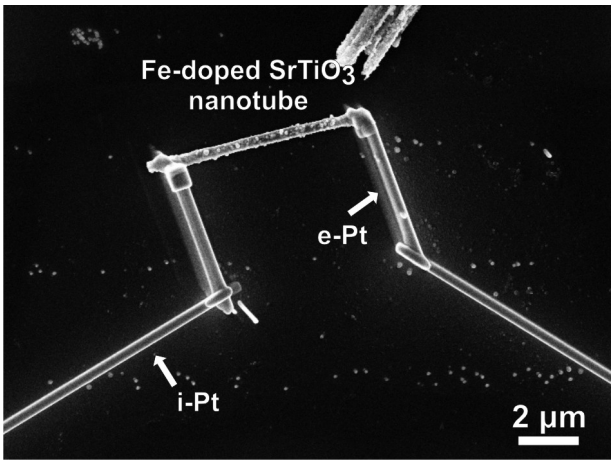

Figure 15. Fe-doped $SrTiO_3$ nanotube contacted in 2-probe configuration using FIB lithography.

3.2.6 Electrical measurements

Two- and four-probe DC electrical measurements on single $BaTiO_3$ nanorods were carried out with a standard source measure unit (Keithley 2400, Keithley instruments, Cleveland, Ohio, USA); gaseous environments were maintained inside a ProboStat cell with mass flow controllers mixing the lab-class analytic gases.[109,110] The effective temperature of the devices was monitored using a thermocouple located beside the sample. The experimental setup (the cell and furnace) was found to act as a Faraday cup, which prevents the electrical measurements from being affected by external electromagnetic noise.

Two-probe DC electrical measurements on single Fe-doped $SrTiO_3$ nanotubes were performed with the help of a self-made electronic circuit designed to ensure low current levels and to avoid undesired fluctuations.[111] The photoresponse was excited using a UV lamp. The UV lamp (HAMAMATSU LC8, Hamamatsu Photonics, Hamamatsu City, Japan) with light source using a type [-01] Hg-Xe lamp enhanced for the line lambda = 365 nm. All the experiments were performed in a real air atmosphere.

4 Results and discussion

4.1 Preparation of highly ordered anodic aluminium oxide membranes

Anodized aluminium oxide (AAO) membranes were used as templates for the EPD deposition of BT and ST sols to form polycrystalline $BaTiO_3$ nanorods and $SrTiO_3$ nanotubes. For that purpose AAO membranes were synthesized by a two-step anodization process in 0.3-M oxalic acid. In that process nanopores with diameters in the range of 80-200 nm were formed with pore lengths of few tens of micrometers. A two-step anodization process was applied to obtain hexagonal close packed columnar cells with uniform Al_2O_3 nanopores. Each cell contains an elongated cylindrical nanopore extending perpendicular from the Al surface. At the oxide/metal interface the pore channels sealed by a thin (few tens of nanometres) barrier layer.[56,58,62]

Figure 16(a) shows annealed Al foil in Ar atmosphere at 500 °C for 3 h in order to release the strains between grain boundaries and to consequently improve the grain connectivity in polycrystalline Al foil. Afterwards the Al foil was electropolished where by means of an electrical potential and current metal was removed in a highly ionic solution. Figure 16(b) shows a FSEM image of electropolished Al sample where highly smooth and optically clean metal surface was observed. At higher magnification (Figure 16(b) inset) we observe the presence of Al_2O_3 nanostripes, which are typically formed during electropolishing of metal foils. During anodization the oxide pore formation starts between those stripes.[112]

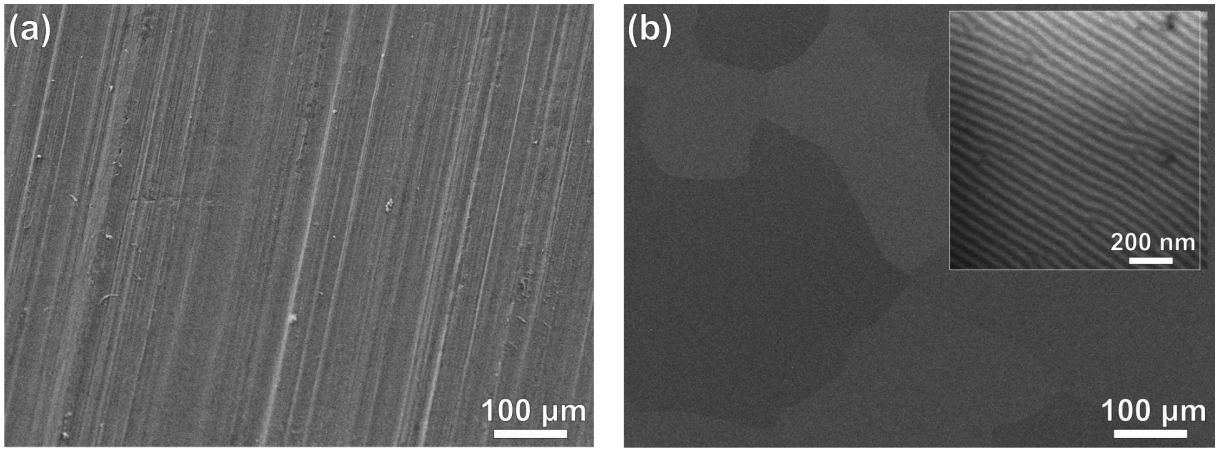

Figure 16. FSEM image of (a) annealed and un-polished Al foil. Annealing conditions: 500 °C for 3 h in Ar atmosphere. (b) Electropolished Al foil where a smooth and optically clean surface is observed. Domains of Al crystals can be seen after polishing. Right corner in Figure 16(b) shows higher magnification image where Al_2O_3 nanostripes are observed.

At the initial stage of anodization, the pores nucleate at small pits or between the nanostripes on the Al surface in an almost random manner. Therefore Al_2O_3 pores on the metal surface have a broad size distribution as shown in Figure 17(a). As the anodization proceeds, the pores merge with each other at the pore bottom in order to establish a homogeneous electric field distribution and/or to minimize the mechanical stress that arises from the volume expansion during the oxide formation at the metal/oxide interface. This process continues until the equilibrium concave shape at the curved oxide/metal interface is established. The equilibrium shape can be observed by completely removing the porous Al_2O_3 layer after the first anodization step. Underneath the first Al_2O_3 layer an ordered hexagonal pattern of etched-pits is formed. This can be exposed by removing the first Al_2O_3 layer (Figure 17(b)) Each etched-pit on the Al surface act as a pore nucleation centre in the second anodization step, resulting in highly ordered hexagonal array of Al_2O_3 nanopores as shown in Figure 17(c). The cross-section image of the Al_2O_3 membrane in Figure 17(d) shows that the pores are usually parallel and straight. Nevertheless, in some places defects are seen in the form of "branches" which are always present regardless of the anodization parameters. The formation of a "branched" pore structure is therefore due to the unstable formation of the Al_2O_3 film at high voltage and is not caused by structure defects on the Al surface.[113]

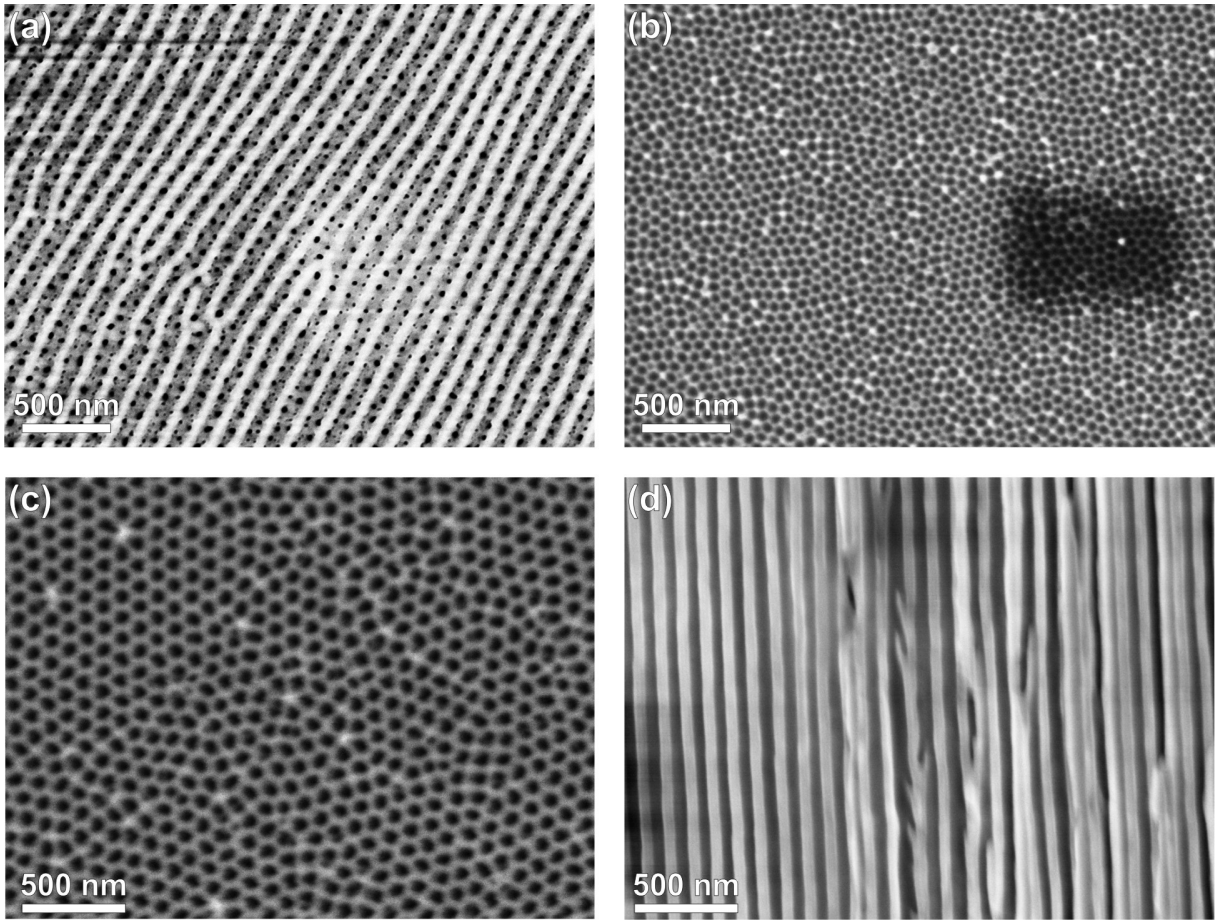

Figure 17. Top-view FSEM images of (a) irregular stripe- like alumina pore formation after first anodization conducted at 40 V in a 0.3-M oxalic acid solution at 5-7 °C. (b) Textured Al surface obtained after removal of the first Al_2O_3 layer. (c) Top-view FSEM image of ordered alumina pores formed using pretextured imprints of alumina on Al foil. Second anodization step was carried out at the same electrochemical conditions as first anodization step. (d) Side-view FSEM image of alumina membrane after second anodization step.

The anodization current as a function of time was measured during both anodization steps (Figure 18). The current for the second anodization step is almost the same as for the first anodization step. The current during the first few minutes increases then it constantly decreases (top line in Figure 18). The high initial current at the beginning of the anodization is due to the conductive nature of the Al surface. As anodization proceeds, insulating Al_2O_3 starts to form on the surface, resulting in a small decrease in the current. The bottom line in Figure 18 corresponds to the second anodization step and has the same behaviour as the first anodization step.

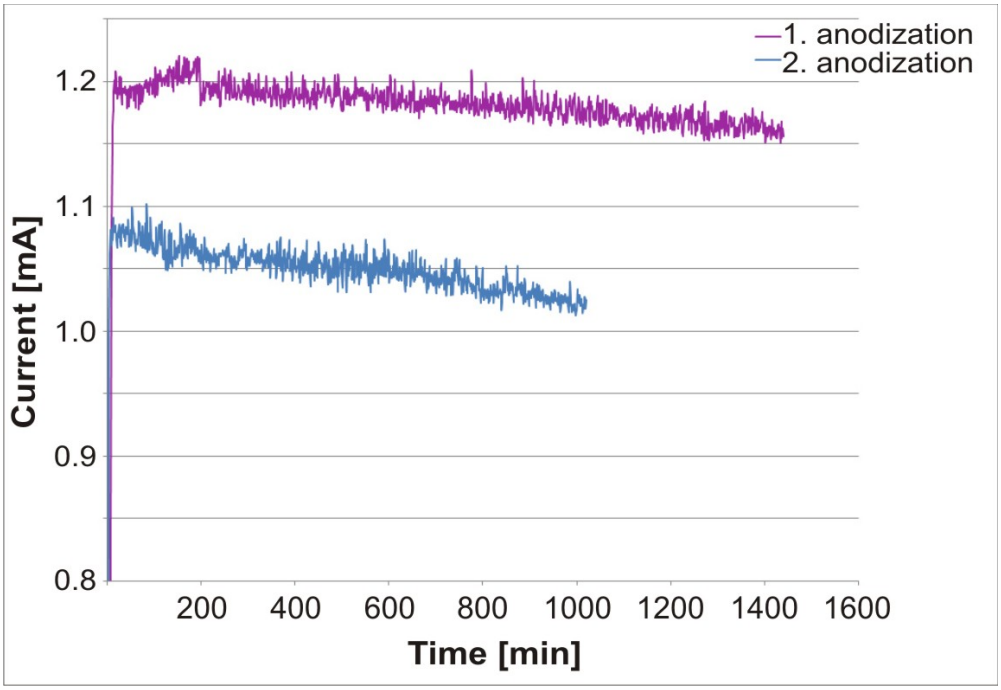

Figure 18. Anodization current as a function of time during the anodization of Al foil. The first anodization (top line) was conducted at 40 V in a 0.3-M oxalic acid solution at 5-7 °C using an electropolished Al foil. Second anodization (bottom line) was carried out at the same electrochemical conditions using the textured Al that was obtained after removal of Al_2O_3 layer after the first anodization.

After the second anodization step the AAO membrane is obtained which remains attached to the Al substrate. However, to use the AAO membrane as a template for EPD of BT and ST sols, the AAO membrane must be separated from the Al foil. Furthermore, the removal of the thin barrier layer in AAO is required to obtain an open channel membrane. Separation of the AAO membrane from the Al substrate was accomplished by complete dissolving of the Al in the $CuCl_2$ solution where Al is oxidized into Al^{3+}. Figure 19(a) and (b) show side-view and bottom-view images of the barrier layer observed after the removal of the remaining Al foil. It can be seen that the bottom of the membrane, which is at the metal/oxide interface, is capped by a thin u-shaped barrier layer. The barrier layer was removed by immersing AAO membranes into a 5 % H_3PO_4 solution. Dissolution of barrier layer is accompanied by widening the pore diameter from an initial pore diameter $D_p \sim 0.3\ D_{int}$ up to $D_p > 0.8\ D_{int}$ (D_p = pore diameter, D_{int} = the interpore distance).[66] The degree of pore widening during the barrier layer opening process can be minimized by selective removal.

Figure 19 (c) and (d) show the side- and bottom-view of the AAO membrane after the removal of the barrier layer and pore widening. The as-prepared AAO membranes had pore diameters ranging between 80 and 200 nm and were 10-25 μm thick. These membranes were then used as templates for EPD of $BaTiO_3$ and ST sols into the AAO pores in order to fabricate $BaTiO_3$ and $SrTiO_3$ nanostructures.

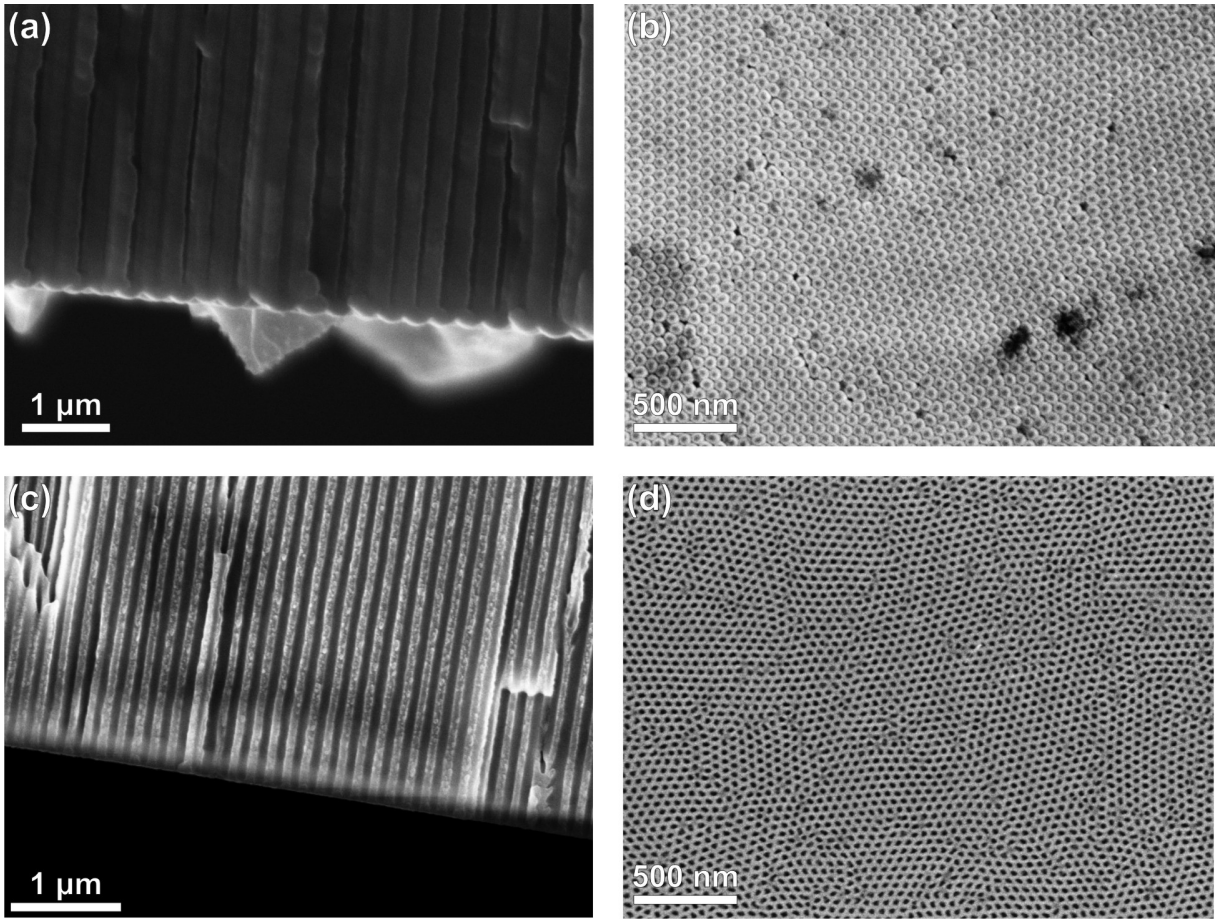

Figure 19. FSEM (a) side-view and (b) bottom-view image of barrier layer observed after removal of un-anodized Al foil in $CuCl_2/HCl/H_2O$ solution. FSEM (c) side-view and (d) bottom-view image observed after removal of the barrier layer and pore widening using 5 % H_3PO_4 solution.

X-ray powder diffraction (XRD) of the AAO membranes was performed on an anodized and annealed AAO membrane (Figure 20). The XRD spectrum of the as-anodized membranes and of the membranes annealed at 700 °C showed presence of amorphous Al_2O_3.

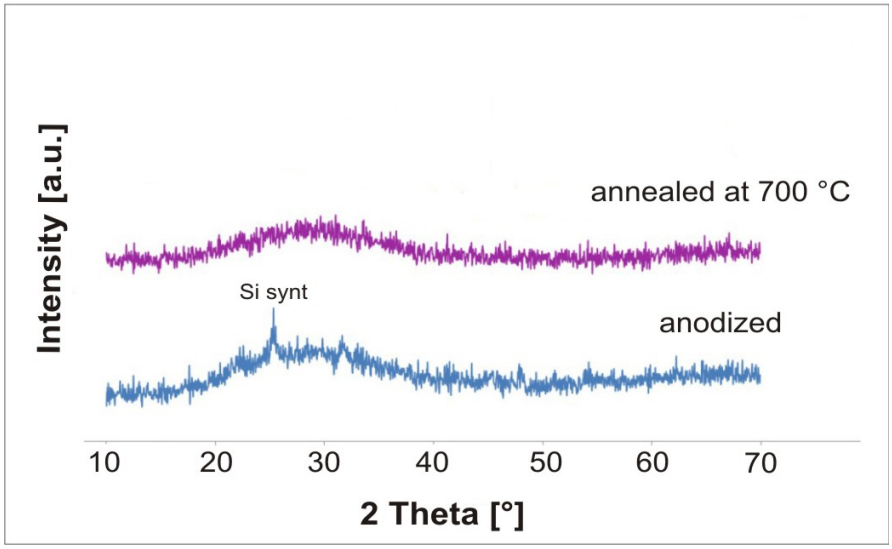

Figure 20. XRD spectra recorded from AAO membranes. Bottom spectrum (blue line) shows amorphous Al_2O_3 obtained after anodization. The peaks present in the background are from synthetic Si since AAO membranes were for XRD deposited on a single Si crystal. Top spectrum (purple line) shows Al_2O_3 obtained after annealing at 700 °C which is still amorphous.

4.2 Fabrication of $BaTiO_3$ nanorods

$BaTiO_3$ nanorods were processed by a sol-gel electrophoretic deposition (EPD) of BT sol into anodic aluminium oxide (AAO) membranes and polycarbonate membranes (PC). The use of both AAO and PC membranes as templates is implemented, followed by optimization of the processing parameters. Resulting $BaTiO_3$ nanorods had diameters ranging from 150 to 200 nm, with an average length of 10-25 μm. By using various electron microscopy techniques we showed that $BaTiO_3$ nanorods were homogeneous regarding their chemical composition. The $BaTiO_3$ nanorods were polycrystalline, composed of well-crystallized pseudo-cubic $BaTiO_3$ grains. A hexagonal polymorph that is coherently intergrown with the $BaTiO_3$ perovskite matrix was also observed as a minor phase. When annealing the AAO templates containing the BT sol in an oxygen atmosphere the presence of the hexagonal polymorph was reduced. Furthermore, two- and four-probe electrical DC measurements were performed on single $BaTiO_3$ nanorods, which were also tested as proof-of-concept humidity sensors. Detailed procedure is explained in the following sections.

4.2.1 Comparison of $BaTiO_3$ nanorods formed in AAO membranes versus $BaTiO_3$ nanorods formed in PC membrane

In order to fabricate rod-like sub-micron structures of crystalline $BaTiO_3$ using EPD of BT sol, track-etched hydrophilic polycarbonate (PC) (Figure 21 (a)) and anodized aluminium oxide (AAO) membranes (Figure 21 (b)) were used as templates. A top-view of the AAO template membranes used in our experiments shows an almost ideal hexagonal close-packed arrangement of the pores with uniform diameters. The cross-section of the AAO membrane shown in the right corner of Figure 21 (b) illustrates that the pores are parallel and straight. The pore size of templates was approximately 200 nm and the size of the nanorods depended on that diameter.

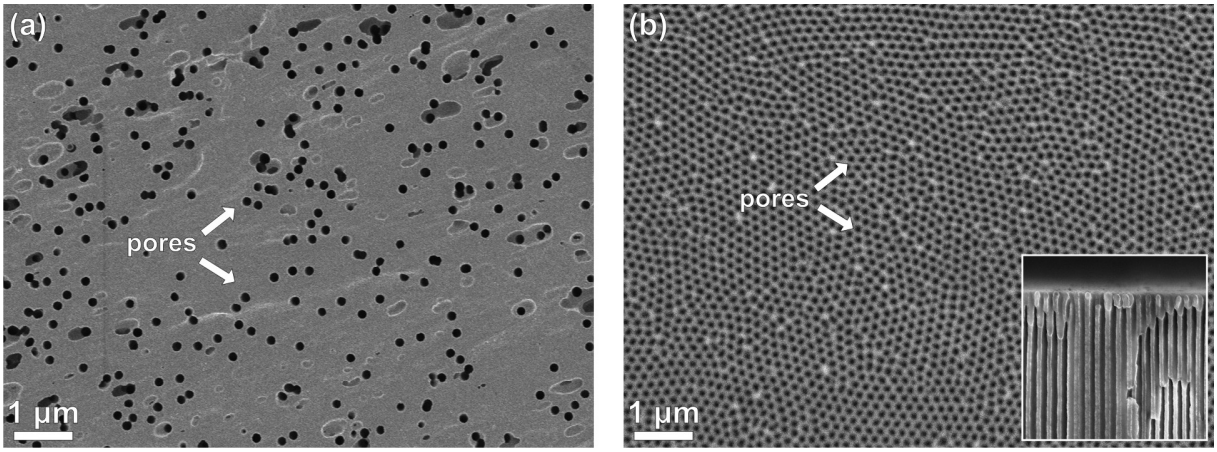

Figure 21. (a) Top-view FSEM image of 25-µm-thick PC membrane with pore diameter of approximately 200 nm. (b) Top-view FSEM image of 25-µm-thick AAO membrane fabricated by two-step anodization process with pore diameter of approximately 200 nm. The inset in the right corner shows a side-view of AAO membrane after removal of barrier layer and pore widening.

Figure 22(a) shows a typical cross-section of $BaTiO_3$ nanostructures formed by EPD and after annealing the filled PC template membranes at 700 °C for 1 h. Although the PC membrane starts to decompose at around 400 °C, according to the DTA results, a higher temperature of 700 °C was used in order to densify and crystallize the $BaTiO_3$ nanostructures within the pores. FSEM micrograph in Figure 22(a) shows that the material grown in the PC template membrane exhibits a fibrous texture. When comparing these nanorods at higher magnification we observed that they all have comparable lengths and diameters. The diameters of $BaTiO_3$ nanorods are around 200 nm, which is approximately the same as the size of the PC template pores. Also the length of the nanorods is comparable with the thickness of the PC membranes, which is approximately 25 µm. It is worth pointing out that when an empty PC template was dipped into the sol without applying an external electric field no nanorods were obtained so implying that no capillary action took place due to immersion into the sol. The drawback when using the PC membrane in the template-based sol-deposition method is that a large number of nanorods are distorted and broken. This is mainly a consequence of burning off the PC membrane during the annealing treatment, as shown in a bright-field TEM micrograph (Figure 22(c)). At the decomposition temperature for the PC membranes (400 °C), $BaTiO_3$ nanorods are not fully dense and not crystalline, and thus they have a limited mechanical strength, since they are held together by the van der Waals force and weak chemical bonds (through surface condensation).[57]

The AAO template membranes, on the other hand, have a rigid pore structure and can also withstand much higher annealing temperatures than the PC templates. This is why it is reasonable to expect that they would be more suitable for processing complex oxide nanostructures that require higher annealing temperatures for crystallization. A low-magnification FSEM image of $BaTiO_3$ material that was obtained after the AAO template was removed by NaOH solution is shown in Figure 22(b). One can observe typical rod-like-shaped $BaTiO_3$ nanostructures that form bundles (and clusters) of various dimensions. Few loose single $BaTiO_3$ nanorods can also be observed. $BaTiO_3$ nanorods exhibit a regular shape and a uniform diameter. Bright-field, low-magnification TEM image in Figure 22(d) shows a typical isolated $BaTiO_3$ nanorod with a diameter of approximately 200 nm, which is comparable to the diameter of the AAO template pores. The regular longitudinal shape of $BaTiO_3$ nanorods indicates that the pores within the AAO template retain their shape even after annealing at 700 °C.

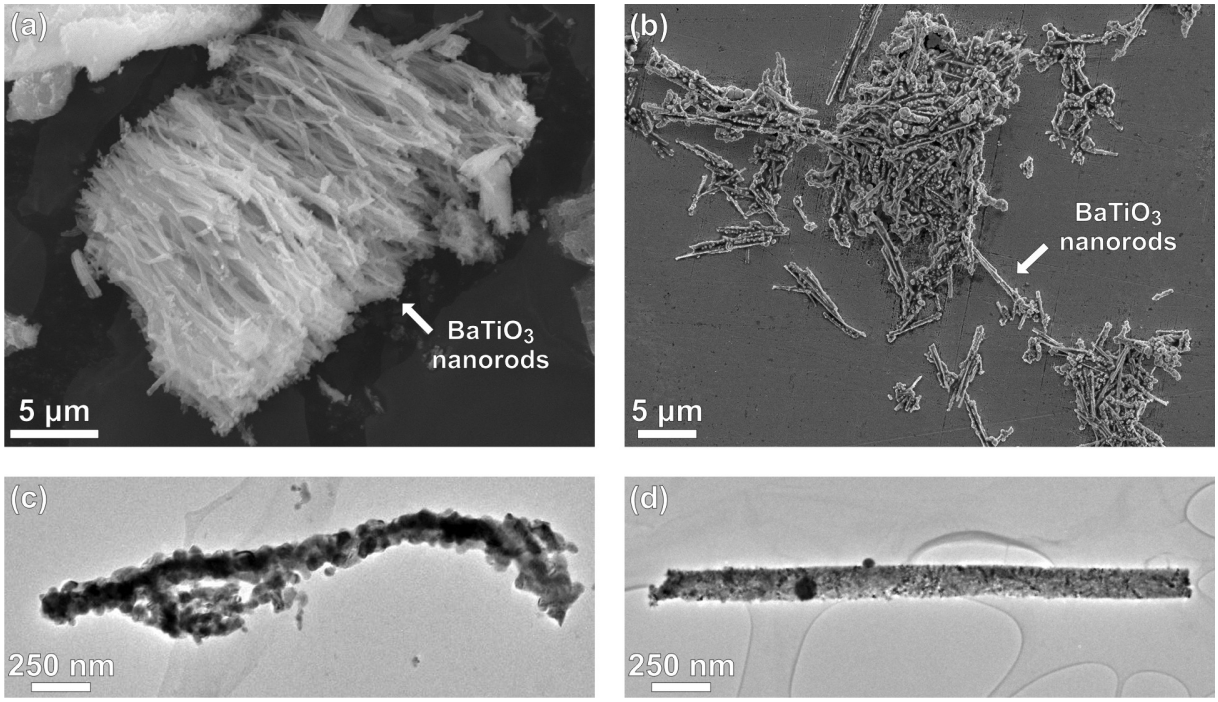

Figure 22. Morphology of $BaTiO_3$ nanorods. (a) Cross-section SEM images of $BaTiO_3$ nanorods prepared in PC template by sol-gel EPD and annealed at 700 °C for 1 h. (b) FSEM image of isolated and bundled $BaTiO_3$ nanorods prepared by sol-gel EPD in AAO template and annealed at 700 °C for 1 h. (c) Bright-field TEM image of a typical nanorod obtained from PC template and (d) bright-field TEM image of an individual uniformly shaped polycrystalline $BaTiO_3$ nanorod grown in AAO template.

Our experimental results showed that both templates, the PC and the AAO membranes, are generally suitable for use in the synthesis of $BaTiO_3$ nanorods. However, each template exhibits certain advantages and disadvantages (Table 5). The main advantage of using the PC membrane is the easy handling and removal by means of pyrolysis at elevated temperatures. On the other hand, the flexibility and the large thermal expansion coefficient may lead to deformation and fracture of $BaTiO_3$ nanorods during the thermal treatment (Figure 22(c)). At the temperature of PC membranes decomposition $BaTiO_3$ nanorods are not yet fully dense nor crystalline. As a consequence $BaTiO_3$ nanorods are usually deformed and partially intergrown which strongly degrades the quality of the product. The main advantage of using AAO membranes as the template material is their rigidity and chemical inertness at temperatures below 750 °C, which allows the $BaTiO_3$ nanorods to densify and crystallize without any noticeable deformation. Also, AAO templates possess a much higher pore density, and thus allow processing of a larger number of nanorods per unit area of the template. The main disadvantage of using the AAO templates however is that they are rather brittle and break easily during experimental handling. Moreover, since wet-chemical etching is the only method to remove the AAO membrane, it is difficult to determine the best etching conditions for dissolving the AAO template without etching the nanorods at the same time.[57] After all, the use of the AAO membrane as the templates proved to be more efficient and suitable for the template-assisted synthesis of perovskite nanorods with uniform diameters and with a relatively smooth surface over much of their length. For this reason AAO templates were used in the rest of our experiments.

Table 5. Advantages and disadvantages of PC and AAO template membranes.

	Polycarbonate membrane (PC)	**Anodic aluminium oxide membrane (AAO)**
Advantages	easy handling	rigidity and resistance to elevated temperatures
	easy removal by means of pyrolysis at elevated temperatures	high pore density
Disadvantages	flexibility and large thermal expansion coefficient	brittle and easily broken during routine handling
		wet chemical etching is the only method to remove the template

4.2.2 Optimization of processing parameters

In order to determine the optimum processing conditions and to ensure the synthesis of dense and fully crystalline $BaTiO_3$ nanorods we systematically varied the following processing parameters:

- applied electric potential during EPD of BT sol into AAO templates,
- annealing temperature,
- and annealing time of deposited material in AAO templates (Table 6).

Table 6. Overview of processing parameters.

Applied electric potential	5 V for 30 min	10 V for 30 min	30 V for 30 min	50 V for 5 min
Annealing temperature at constant time	500 °C for 1 h	600 °C for 1 h	700 °C for 1 h	800 °C for 1 h
Annealing time at constant temperature	700 °C for 1 h	700 °C for 12 h	700 °C for 24 h	700 °C for 48 h

The influence of an applied electric potential on deposition can be seen in the growth of $BaTiO_3$ grains in nanorods inside 200 nm AAO template pores as shown in Figure 23. The variation of the applied electric potential during EPD showed that by increasing the potential the grain size, when annealed at the same temperature, increases as well. Figure 23 and Figure 24 show the difference in grain sizes as a function of applied voltages. When the potential of 5 V was applied for 30 min the size of the grains was in the range 5-10 nm in diameter, when the potentials of 10 or 30 V were applied for 30 min, the size of grains increased to an average diameter of 15 nm. When a potential of 50 V was applied, an undesired reaction of sol decomposition started at the contact between the AAO template and the Al working electrode which prevented further template filling. This is why the EPD was stopped after only 5 min. The size of grains was increased to 20-25 nm at an applied voltage of 50 V. Also the nanorods themselves were no longer uniform and smooth throughout their length but rather discontinuous, bent and less dense (Figure 25).

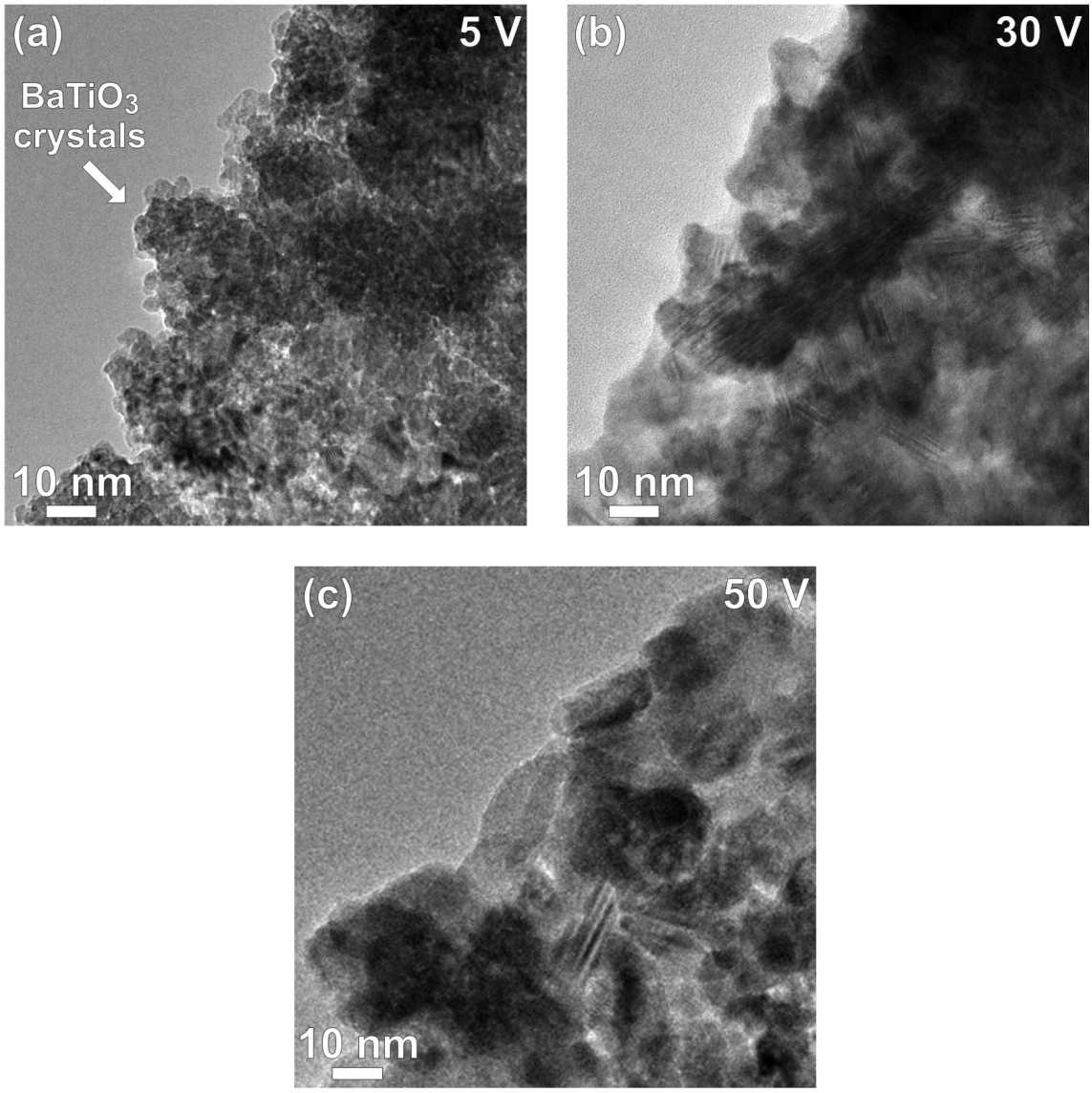

Figure 23. Bright-field TEM images of polycrystalline $BaTiO_3$ nanorods formed in AAO template by sol-gel EPD, annealed at 700 °C for 1 h and leached from AAO template. During EPD different electric potentials were applied (a) 5 V for 30 min, (b) 30 V for 30 min and (c) 50 V for 5 min.

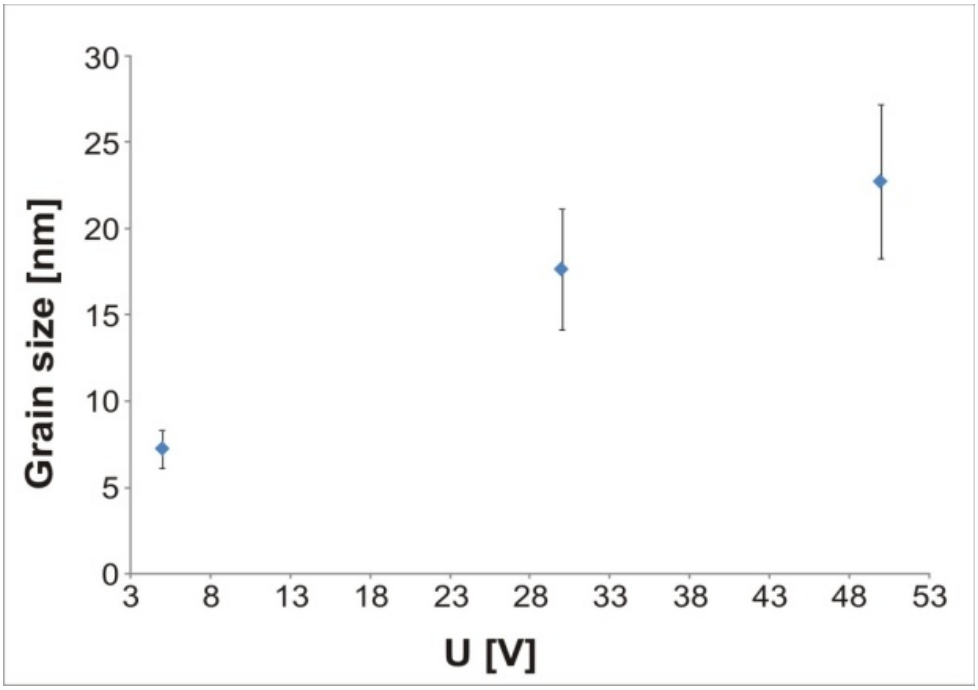

Figure 24. Grain size as a function of applied potential during EPD. Higher potential during EPD is leading to bigger grains.

In general, for the formation of oxide nanorods by electrophoresis, it is expected that the applied potential for formation would have a significant influence on the synthesized product. It is postulated that the mobility, μ, (Eq. 17) equals velocity, v, per unit field and therefore the particle velocity can be expressed in terms of the charge on the particle, q, and the applied electric field, E:[4,8,57]

$$v = \frac{qE}{6\pi\eta r} \qquad (20)$$

Where η is the viscosity of the solvent and r is the radius of the particle. According to Eq. 20, the velocity of the particles (and thus the deposition rate) is proportional to the electric potential. Therefore, at smaller applied voltages, slower deposition rates are expected and at higher voltages, the particles move faster and the deposition rate may be too fast to form high-quality deposit material. In addition, separation of nanoparticles by size under the applied electric potential could also influence the deposition of sol.[4,75] If there is a distribution of nanoparticle sizes present in the sol, then there will be, according to Eq. 20, a distribution in velocities of the particles as well. This effect is more evident at higher potentials, leading to the larger differences in deposition rate for small particles versus large particles.

There are three competing processes that can affect the quality of deposited nanorods:

- speed of nanoparticles arrival to the deposition surface,
- rearrangement of nanoparticles to positions of lower free energy,
- and rate of condensation reactions between the particles

As the moving nanoparticles arrive at the formation surface, they need some time to rearrange to a location of lower energy.[57] If the applied potential is too high, then nanoparticles arrive at a faster rate than they could rearrange on the surface, causing them to become locked into higher energy positions reducing the quality of the deposit. Figure 25 shows polycrystalline $BaTiO_3$ nanorods formed in the AAO template and annealed at two different applied potentials. At the lower potential (Figure 25(a)) the nanorods are smooth and dense all over their surface while at the higher potential (Figure 25(b)) the nanorods are discontinuous and porous while the crystal size is larger. Therefore, we can conclude that if the deposition rate is slow with respect to the condensation rate, then increasing the field increases the deposit density. If the deposition is faster than the condensation rate, a less dense deposit is produced. Since the optimum filling of the template was achieved at the potential of 30 V, this potential was used in all the following experiments.

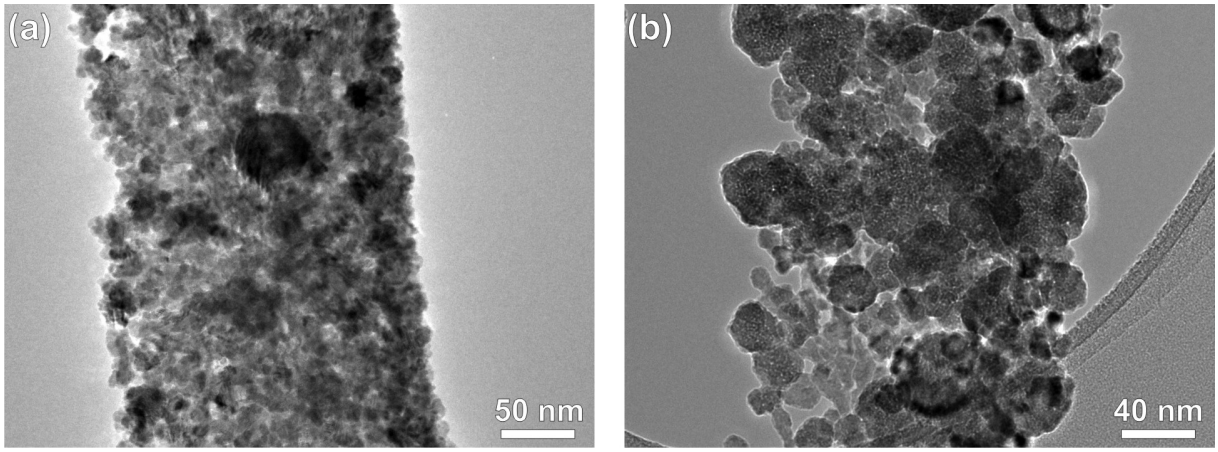

Figure 25. Bright-field TEM image of polycrystalline $BaTiO_3$ nanorods formed in AAO template at applied potentials of (a) 30 V for 30 min (b) 50 V for 5 min and annealed. At higher potential, the nanorods become discontinuous and less dense.

Annealing in AAO membranes was conducted after the EPD at temperatures from 500 °C to 800 °C and annealing times from 1 h to 24 h were changed in order to observe any further differences in density and crystallinity of the nanorods. Figure 26 shows bright-field TEM micrographs with the corresponding SAED patterns showing the state of crystallinity of the $BaTiO_3$ nanorods that were annealed at different temperatures and leached from the AAO templates. The optimal annealing temperature for crystallizing the $BaTiO_3$ nanorods was 700 °C (Figure 26(c)), which turned out to be the best compromise for producing fully dense and well crystallized $BaTiO_3$ nanorods with no chemical reaction occurring between the alumina (AAO) template and $BaTiO_3$. At higher annealing temperatures (Figure 26(d)) $BaTiO_3$ starts to react with the Al_2O_3 template and its removal becomes increasingly difficult due to the nanorod-template bonding. At annealing temperatures below 600 °C (Figure 26(a) and (b)), however the crystallization was not yet completed and remaining amorphous phase was abundant within the $BaTiO_3$ nanorods.

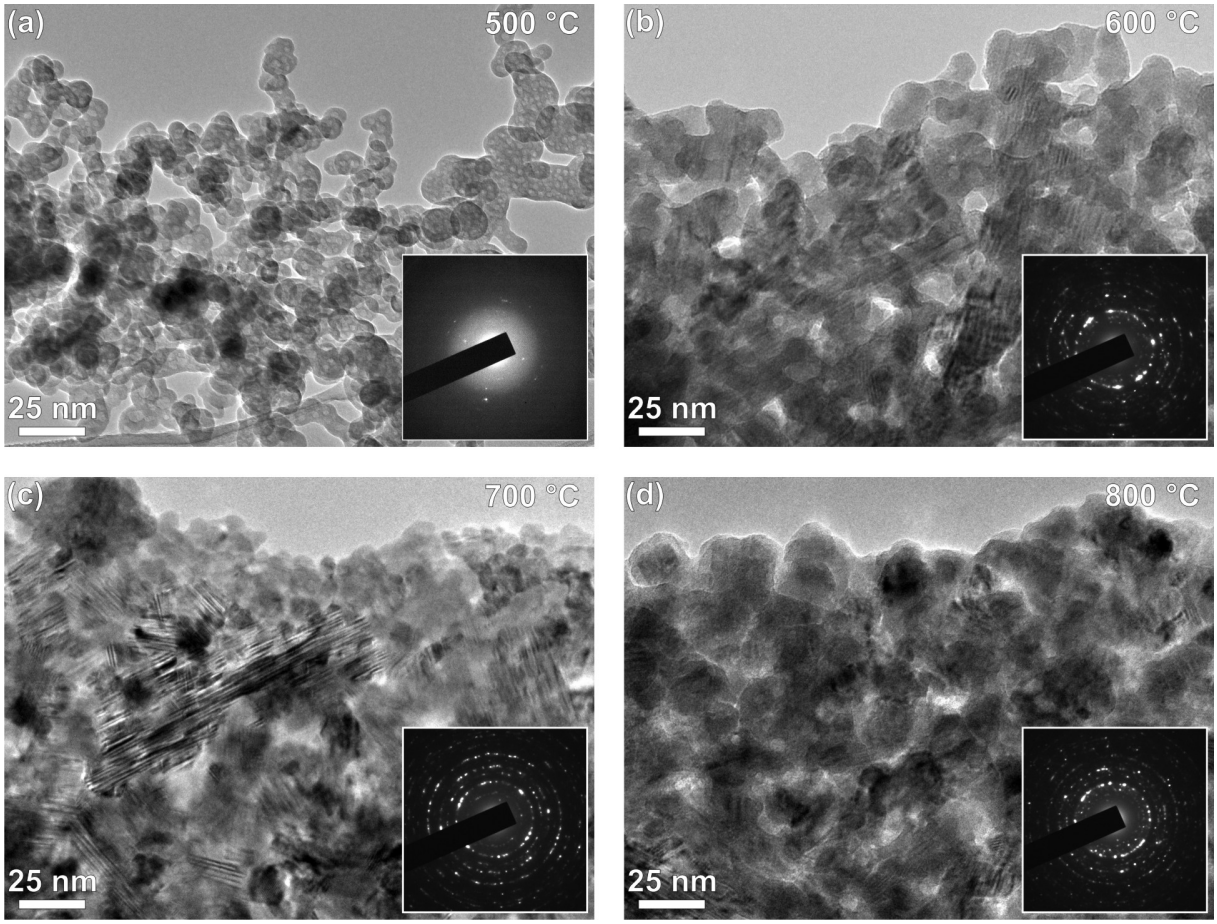

Figure 26. Bright-field TEM images of polycrystalline $BaTiO_3$ nanorods annealed at (a) 500 °C, (b) 600 °C, (c) 700 °C and (d) 800 °C for 1 h. The insets show the corresponding SAED patterns. At 500 °C (a) material is mainly amorphous, at 600 °C (b) is partially nanocrystalline. At 700 °C (c) and 800 °C (d) material is well crystallized.

Prolonged annealing at 700 °C (Figure 27 and Figure 28) did not significantly increase the grain size of the nanosized $BaTiO_3$ grains. It was observed that it is not possible to transform polycrystalline nanorods to single-crystalline nanorods even after prolonged heating. It was concluded that the annealing time of 1h at 700 °C produces the best overall quality of the product.

Based on these observations in all further experiments an applied electrical potential of 30 V was used, which was maintained for 30 min. Afterwards the deposited material in the AAO template was annealed at 700 °C for 1 h.

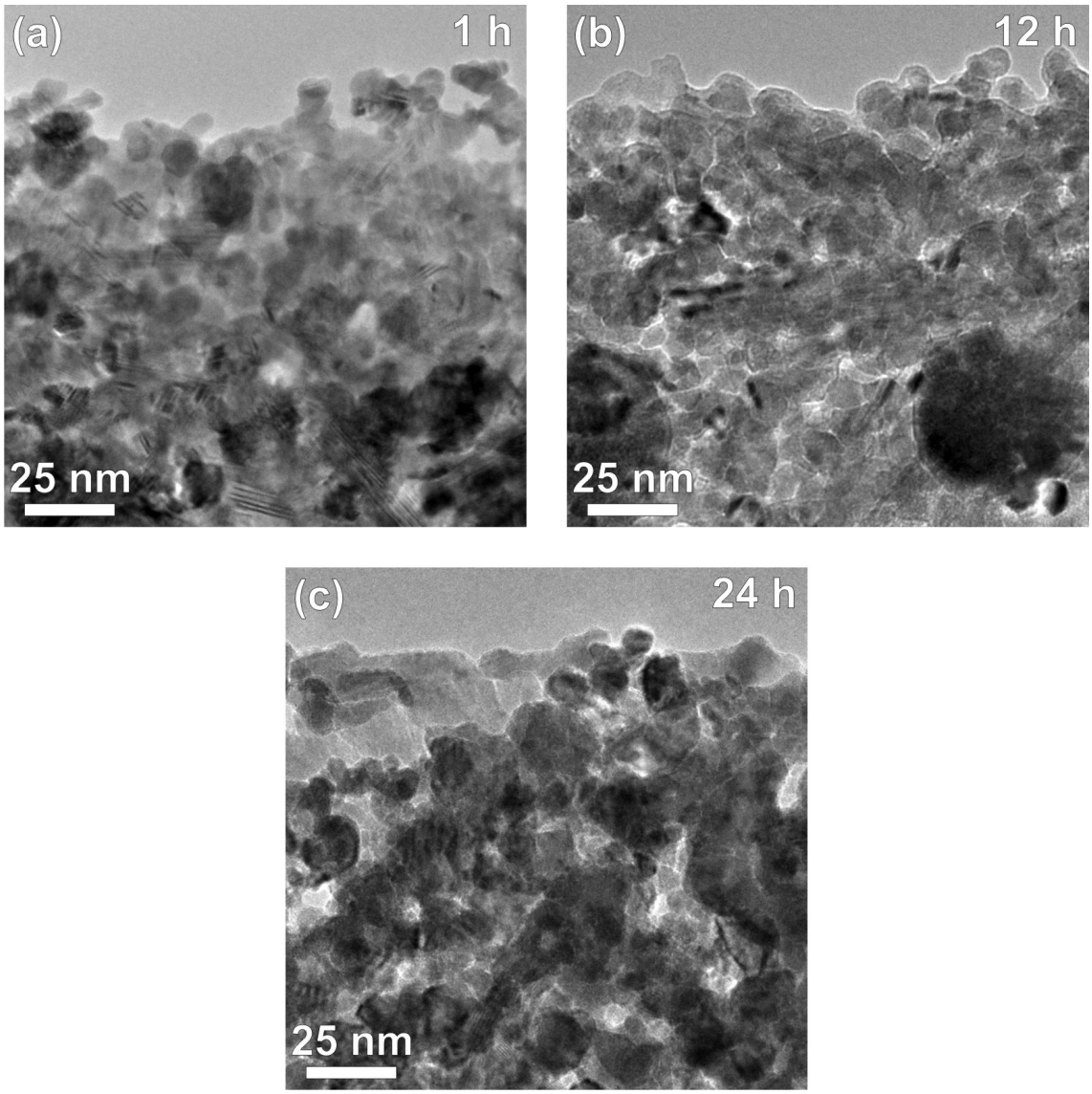

Figure 27. Bright-field TEM images of polycrystalline $BaTiO_3$ nanorods annealed at 700 °C for (a) 1 h, (b) 12 h and (c) 24 h.

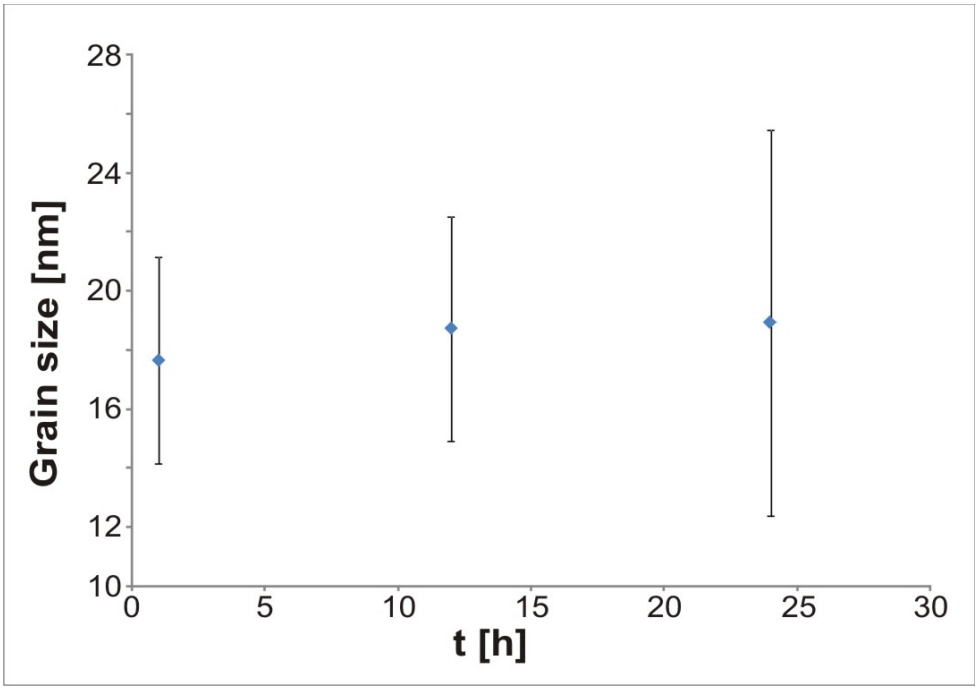

Figure 28. Grain size as a function of annealing time at constant annealing temperature of 700 °C. The grains do not coarsen after a longer annealing time. However, the size distribution becomes wider.

4.2.3 X-ray powder diffraction

After the EPD of the BT sol into the AAO pores at a selected potential and after the removal of the AAO templates in the NaOH solution, the remaining material was first examined by X-ray powder diffraction (XRD). In order to obtain a sufficient amount of material for the XRD measurements, the material was collected from many dissolved AAO templates in NaOH solution and concentrated by means of centrifugation. The XRD pattern of the so-obtained material shows only the presence of diffraction peaks that can be assigned to cubic $BaTiO_3$, according to the JCPSD card No. 89-2475 (Figure 29). After annealing the AAO templates with filled BT sol at 700 °C the transformation of the sol into crystalline $BaTiO_3$ was complete.

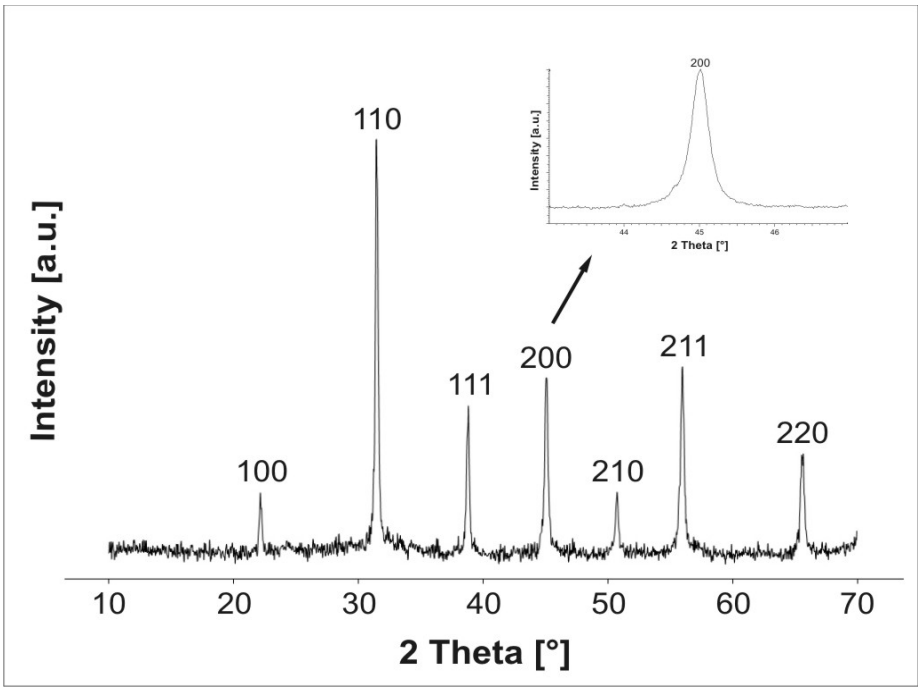

Figure 29. XRD spectrum recorded from the material after AAO template removal showing only the presence of diffraction peaks corresponding to cubic $BaTiO_3$. No splitting of the characteristic (200) peak is observed. The relatively poor peak-to-noise ratio of the recorded spectrum is due to the small amount of available material.

4.2.4 Raman spectroscopy

The transition between the tetragonal and the cubic $BaTiO_3$ naturally takes place at the Curie temperature (120 °C). However, when the size of the $BaTiO_3$ crystallites approaches a nanometre range, the relaxation of the tetragonal unit cell occurs and the unit cell becomes cubic even at the room temperature.[102,114-116] Since no splitting of the characteristic diffraction peaks was observed by XRD, which would confirm the presence of the tetragonal $BaTiO_3$ polymorph, Raman spectroscopy (RS) was used for an additional structural characterization. The characteristic Raman spectrum of $BaTiO_3$ material recorded at room temperature is shown in Figure 30. Although for a cubic structure the symmetry group does not predict the Raman active modes of the first order, in cubic perovskites two broad bands of the second order at about 225 and 520 cm^{-1} can generally be observed[117], which is also the case in the recorded Raman spectrum in Figure 30. Such Raman activity can be explained by the disorder of titanium in a nominally cubic phase. In addition to the broad bands that can be assigned to the cubic $BaTiO_3$ polymorph, the characteristic bands for the tetragonal structure at 250, 307, 515 and 715 cm^{-1} are also observed in the recorded Raman spectrum. However, to confirm the extent of the tetragonal nature of the processed $BaTiO_3$ material, the relative intensity of those bands should also be taken into account. According to Upendra *et al.* the reduction of the intensity and sharpness of the band at 307 cm^{-1} indicates that the tetragonal phase is not dominant in the synthesized $BaTiO_3$.[118] Such a reduction of the 307 cm^{-1} band intensity was observed in all samples. This result is a consequence of the intrinsic phase transition from tetragonal to cubic structure caused by reducing the crystallite sizes below critical.[102,114-116] As Yashima *et al.* reported, with decreasing of the particle size from 430 to 140 nm, the *c*/*a* ratio decreases and the particle size approaches the critical size where the *c*/*a* ratio becomes unity.[116] Based on the combined results of XRD and Raman spectroscopy it was concluded that the synthesized $BaTiO_3$ has a predominately cubic structure, nevertheless some tetragonality is also present. Nearly cubic structure of obtained nanostructure is most likely the consequence of the larger crystallite sizes. This is why we refer to the crystal structure of synthesized $BaTiO_3$ as “pseudo-cubic” instead of “cubic” throughout the text.

Raman spectroscopy showed an additional interesting phenomenon. Namely, the observed band at 630 cm^{-1} indicates the presence of hexagonal $BaTiO_3$ polymorph,[102,119] which is a high-temperature $BaTiO_3$ polymorph and which, according to the phase diagram $BaO\text{-}TiO_2$,[120-122] should form above 1432 °C. Since hexagonal polymorph was also observed by transmission electron microscopy, the detailed structural characterization of this polymorph, existing in synthesized $BaTiO_3$, is described in Section 4.2.8.

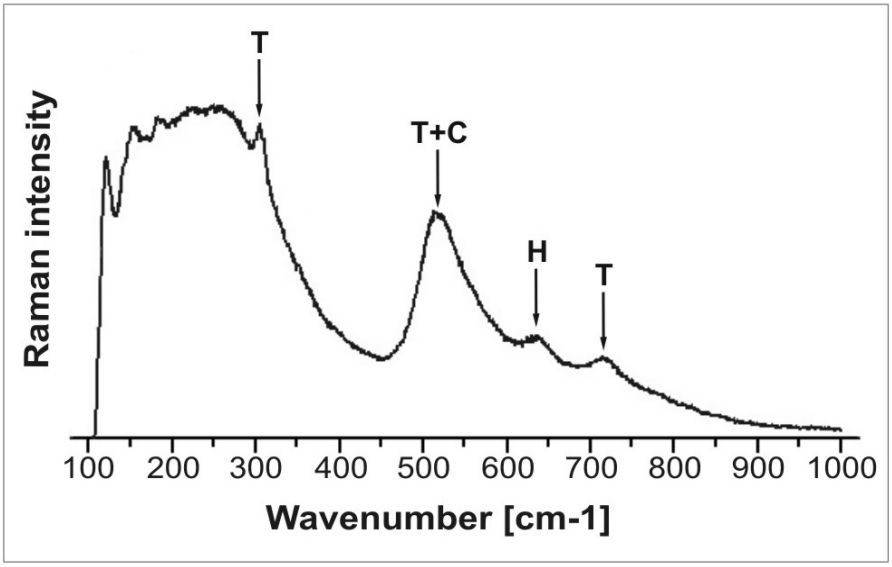

Figure 30. Raman scattering spectrum recorded from the $BaTiO_3$ after annealing and removal of the AAO template. T, C and H denote the Raman bands characteristic for the tetragonal, cubic and hexagonal $BaTiO_3$ polymorphs, respectively.

4.2.5 Chemical composition of $BaTiO_3$ nanorods

Chemical composition of the individual annealed $BaTiO_3$ nanorods was studied by energy-dispersive X-ray analysis (EDXS) in TEM. The EDXS spectra were acquired from marked regions along a single $BaTiO_3$ nanorod, as shown in Figure 31(a). A typical EDXS spectrum acquired from one of the regions is shown in Figure 31(b). Apart from the peaks corresponding to Ba and Ti, the spectrum additionally revealed very low intensity peaks for Al, Na and Si. The Al peak originates from an incomplete removal of the AAO template. Na and Si originate from the NaOH etching solution. Due to very small amount of these elements, they were omitted from the quantification of the EDXS spectra. The results of quantitative EDXS analysis from the

marked regions using pure $BaTiO_3$ as a reference material show that the measured Ba:Ti atomic ratios correspond to the stoichiometric composition of $BaTiO_3$, *i.e.*, the BaO/TiO_2=1:1. Statistical errors are shown in Table 7. The observed homogeneous chemical composition of $BaTiO_3$ nanorods is consistent with our XRD and Raman results. This further implies that the of EPD process into the AAO template membranes is statistical process and that stoichiometric BT sol is already formed therefore there is no change in the chemical composition during annealing.

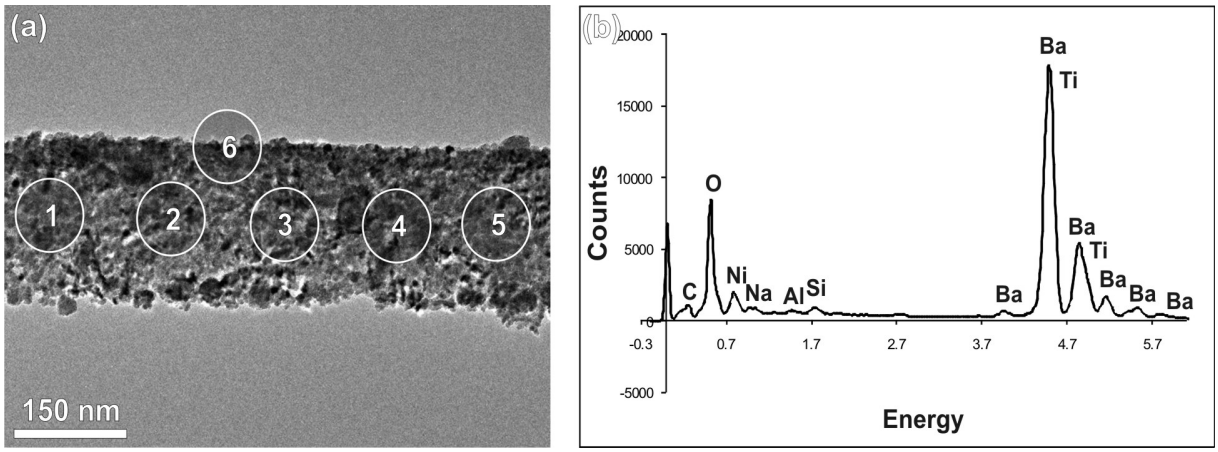

Figure 31. EDXS analysis from a single annealed $BaTiO_3$ nanorod. (a) Marked regions for the acquisition of the EDXS spectra, and (b) a typical EDXS spectrum from the marked region.

Table 7. Results of quantitative EDX analysis from marked regions (Figure 31) on $BaTiO_3$ nanorod.

Region	1	2	3	4	5	6
Ti K (at. %)	19.7±0.3	19.4±0.3	19.7±0.3	19.6±0.3	19.3±0.3	19.1±0.3
Ba L (at. %)	20.4±0.5	20.7±0.5	20.4±0.5	20.2±0.5	20.8±0.5	21.0±0.5
Ba/Ti	1.04±0.6	1.07±0.6	1.04±0.6	1.01±0.6	1.08±0.6	1.1±0.6

4.2.6 Morphology of $BaTiO_3$ nanorods

Since it is not possible to unambiguously determine the cross-sectional shape of 1-D nanostructures by conventional bright-field TEM imaging due to various contributions to the image contrast, we used HAADF-STEM to additionally demonstrate that $BaTiO_3$ nanorods are indeed solid. Namely, in HAADF-STEM, the intensity in the experimental image is proportional to TDS, *i.e.* the specimen's thickness, assuming homogeneous chemical composition.[123] An experimental HAADF-STEM image recorded from part of a single $BaTiO_3$ nanorod shows that the intensity in the centre of the nanorod is higher than the intensity at the nanorod edges (Figure 32(a)). An average intensity profile across the nanorod reveals that intensity profile has a roughly semi-cylindrical shape (Figure 32(b)) which confirms that $BaTiO_3$ nanorods are indeed rods and not tubes, where central part would show lower intensity. However, this discrepancy from the ideal semi-circular intensity profile also implies that the nanorods are probably not ideally cylindrical in shape. In addition, the surface of the nanorods is rough due to their relatively coarse crystalline nature, which additionally contributes to the intensity fluctuations of the measured intensity profile.

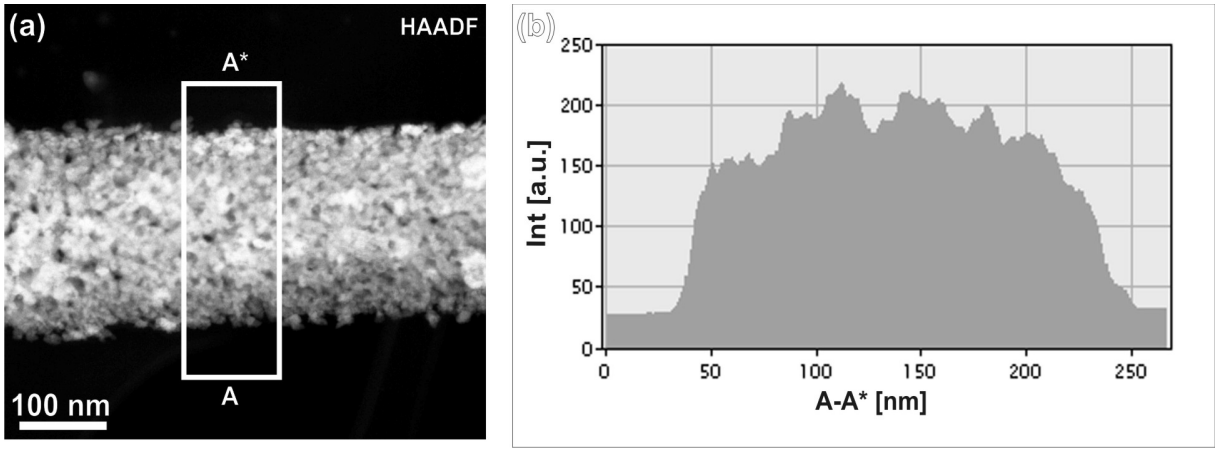

Figure 32. (a) HAADF-STEM image of a single $BaTiO_3$ nanorod. (b) The corresponding average intensity profile taken from the marked region across the nanorod.

The consistency of the nanorods was additionally investigated by preparing cross-sections of $BaTiO_3$ nanorods by ultra-microtomy. Radial cut through the $BaTiO_3$ nanostructures showed different morphologies (Figure 33). Apart from fully dense more or less ideal nanorods, we could also observe half-hollow and hollow tubes. Nevertheless, more than 80 % of the product was observed to be in the form of nanorods.

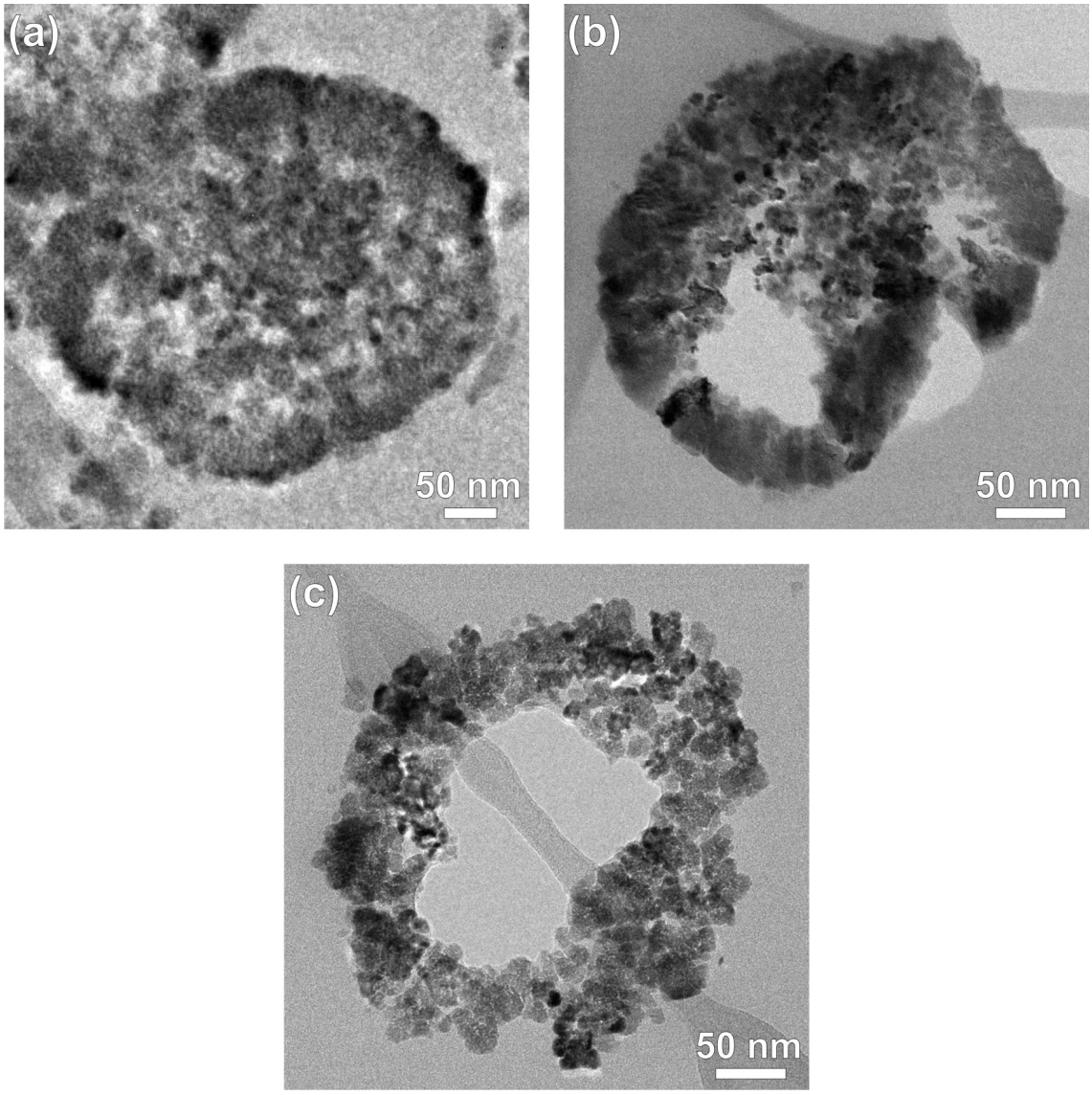

Figure 33. Bright-field TEM image of a radial ultra-microtomic cross-section of polycrystalline $BaTiO_3$ nanostructures. Different morphologies can be observed. (a-c) Rod-like and tubular shaped $BaTiO_3$ 1-D nanostructures.

4.2.7 Formation mechanism of $BaTiO_3$ nanorods

A schematic drawing of the deposition process during the EPD is shown in Figure 34. It demonstrates the steps that were stated by other authors[57] and that we also believe occur in the deposition process. When an electric potential is applied to the sol, the positively charged nanoparticles in the sol are drawn through the pores of the template towards the cathode placed behind the template. It has been stated that the charged nanoparticles from the sol fill the pores of the template, starting at the bottom, where the template is directly connected to the working electrode, while the negatively charged counter-ions move in the opposite direction.[4,8,54,88] In this manner, as time increases, all the pores are eventually completely filled (Figure 34).

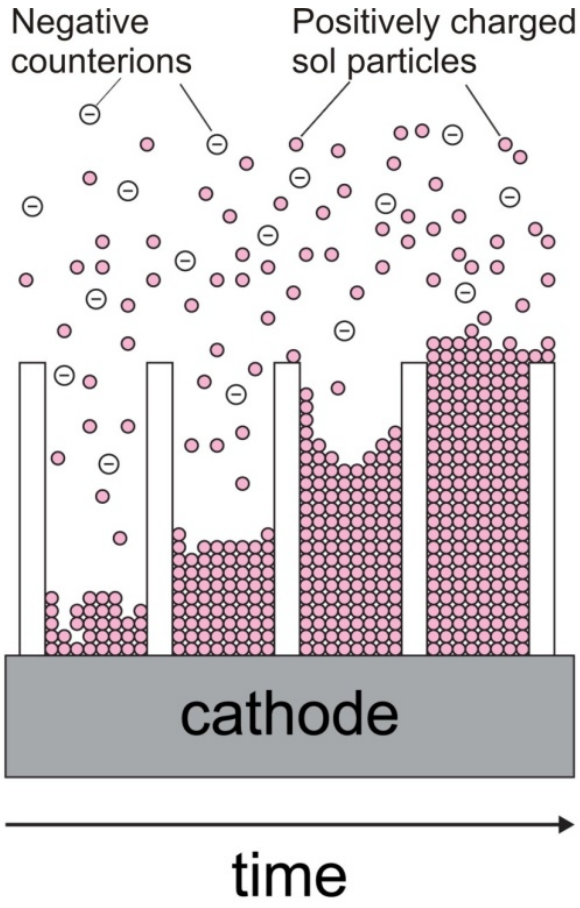

Figure 34. Schematic illustration of the nanorod formation process during deposition. Positively charged particles are moving electrophoretically towards the negative electrode (cathode), depositing at the bottom of the AAO pore, while negatively charged counter ions are moving in the opposite direction. As time increases, the densely packed sol particles fill more of the pore, until the pore is completely filled.

The main reason for a specific nanorod- and/or nanotube-shaped morphology after annealing the deposited BT sol lies in the crystallization process that takes place inside the AAO pore channels during the annealing of the sol-gel. The infiltrated material after the EPD was found to be amorphous by X-ray analysis. During heat treatment of the AAO templates with the BT sol-gel at elevated temperatures, the decomposition of the amorphous organic components and the densification of the $BaTiO_3$ nanorods occur. After initial dehydration, chelated precursors start to decompose with a significant release of H_2O, CO and CO_2 gases at higher temperatures. The release of these gases can also form local reductive atmosphere. As a result of the pyrolysis and calcinations with a further release of gaseous products, $BaTiO_3$ crystallizes in the form of nanosized crystals. As the precursor material is being slowly consumed for crystal growth, they gradually approach the tube walls together with the depleting mass of the remaining sol-gel, which acts as a viscous semi-fluid medium. Therefore, $BaTiO_3$ nanorods and/or nanotubes can be formed as shown in Figure 35 (b) and (c). The reason why in $BaTiO_3$ a much larger fraction of the observed nanostructures exhibit nanorod morphology still needs to be elucidated, however it is reasonable to assume that the attraction forces between the $BaTiO_3$ crystals during densification are stronger than the forces between the $BaTiO_3$ crystals and the AAO membrane surface.

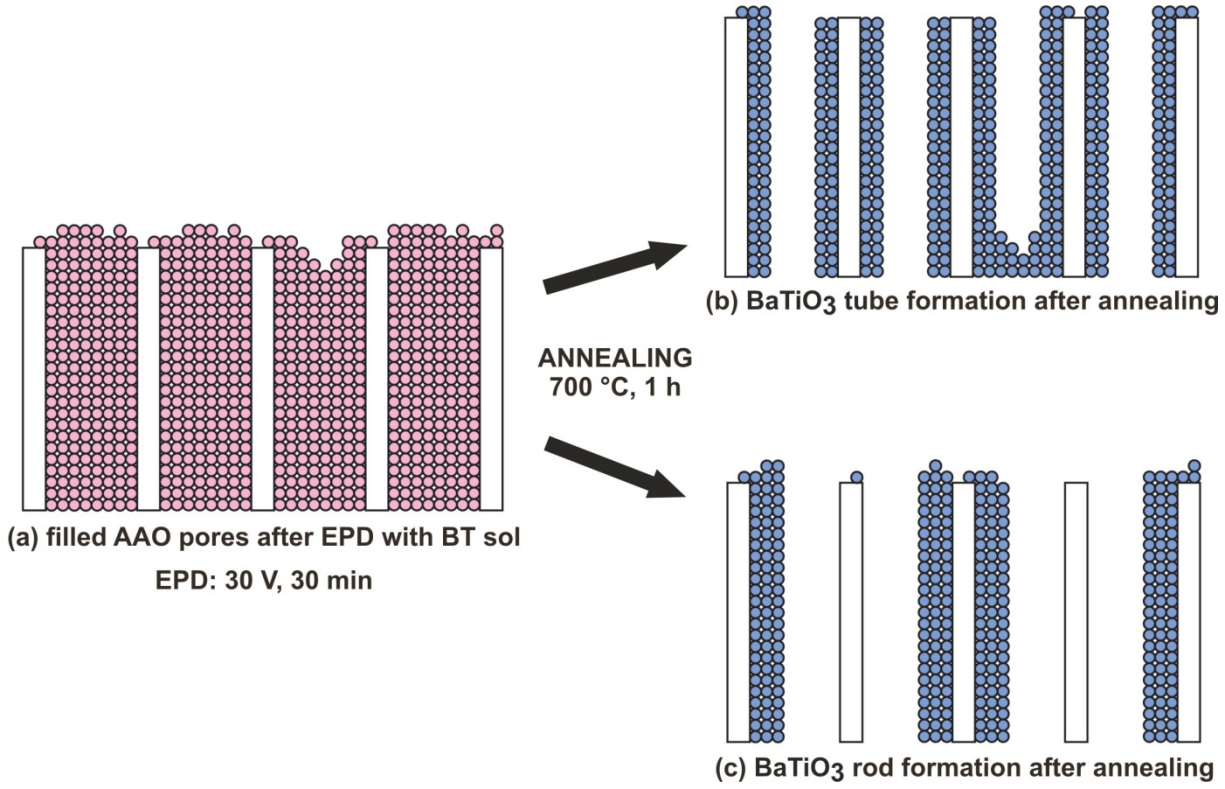

Figure 35. (a) Completely filled AAO pores after EPD. (b,c) Nucleation and crystallization processes during annealing. The illustration shows the resulting morphologies after annealing at 700 °C for 1 h. The possible morphologies are rod-like or tube-like nanostructures.

4.2.8 Hexagonal $BaTiO_3$ polymorph

In order to prove the existence of hexagonal polymorph of $BaTiO_3$, we studied the samples by TEM. The selected-area electron-diffraction (SAED) pattern taken from a few hundred grains in a $BaTiO_3$ nanorod showed that the experimental diffraction pattern corresponds to the calculated electron-diffraction pattern for the cubic $BaTiO_3$ crystal structure, which is in accordance with the results of the XRD (Figure 29). However, additional weak diffraction rings with lattice spacing values of D_1=0.47 nm, D_2=0.34 nm and D_3=0.28 nm (Table 8) were also observed in the experimental electron-diffraction pattern (Figure 36). These d-values correspond to the high-temperature, hexagonal $BaTiO_3$ polymorph (JCPDS 82-1175) consistently with the observed Raman spectra (Figure 30). The weak diffraction rings (D_1 and D_2) for the hexagonal phase indicate that the hexagonal polymorph is a minor phase within the $BaTiO_3$ nanorods.

Table 8. Measured d-values (from SAED) for marked regions in Figure 36 and comparison with reported crystallographic data (JCPDS 82-1175) for hexagonal modification.

SAED	d_{exp}	d_h	hkl_h	Modific.
D_1	0.466	0.46714	{101}	hex
D_2	0.342	0.33933	{103}	hex
D_3	0.284	0.28543	{104}	hex

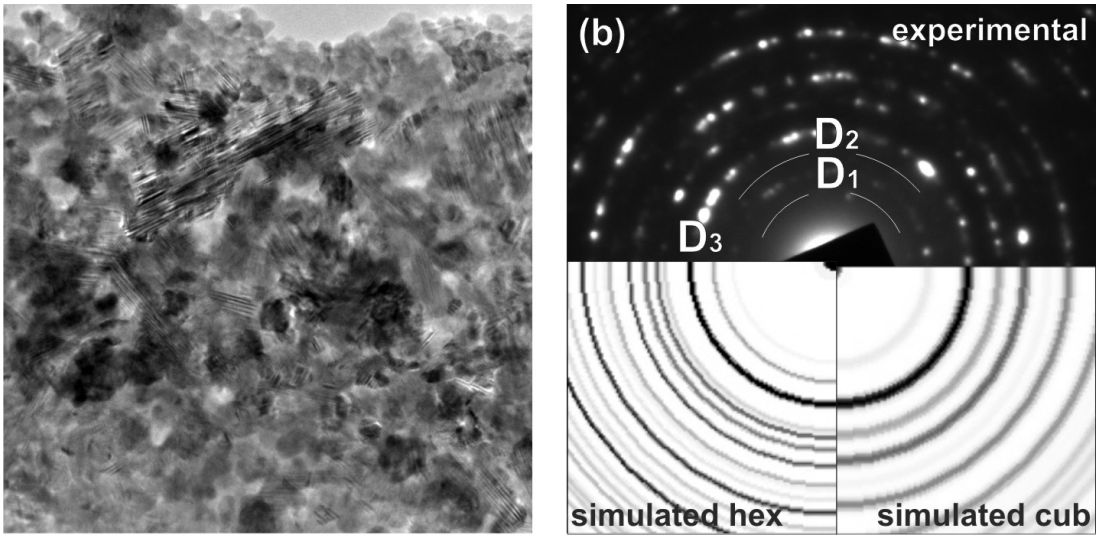

Figure 36. (a) Bright-field TEM image of polycrystalline $BaTiO_3$ nanorod with the (b) corresponding SAED pattern. Diffraction rings corresponding to the hexagonal polymorph are marked as D_1, D_2 and D_3. The inset shows simulated SAED pattern for hexagonal (left corner) and cubic (right corner) polymorph.

$BaTiO_3$ grains with a pseudo-cubic crystal structure were additionally examined by high-resolution transmission electron microscopy (HRTEM). It was found out that two types of $BaTiO_3$ grains were observed, namely smaller, defect free grains, which showed no faceting and larger, sometimes elongated grains that also contained intergrown hexagonal polymorph (Figure 37). It was additionally observed that the grain boundaries between the $BaTiO_3$ grains showed the presence of remaining amorphous phase.

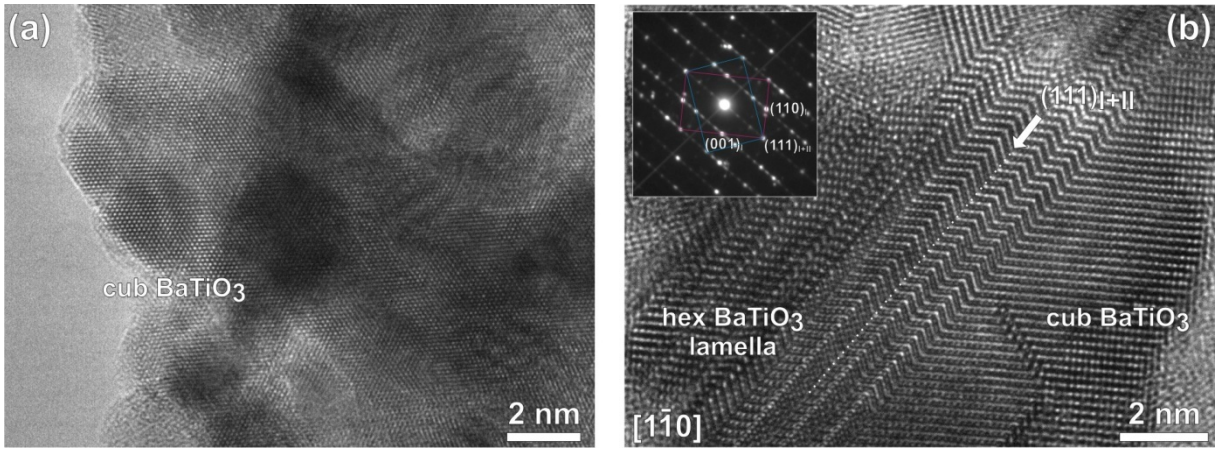

Figure 37. (a) Bright-field HRTEM image of pseudo-cubic $BaTiO_3$ grains. (b) Bright-field HRTEM image of slabs of hexagonal $BaTiO_3$ polymorph intergrown with cubic $BaTiO_3$ as seen in the $[1\bar{1}0]$ zone axis. The inset presents the SAED corresponding to the hexagonal polymorph.

The hexagonal polymorph of $BaTiO_3$ can be structurally viewed as an ideal 6H ordering of double (111) twins. This is why the observed reflections in the SAED patterns must arise from the regions of ordered (111) twins. However, the ordering of the (111) twins in nanosized $BaTiO_3$ is not ideal and also regions of more-or-less ordered twins can be observed, as shown in the HRTEM image in Figure 37(b). The observed hexagonal polymorph of $BaTiO_3$ was never observed as a stand-alone phase in the form of single, nanosized grains, as one would expect according to the corresponding BaO-TiO_2 phase-equilibrium diagram. A high-resolution HRTEM image taken from a region containing only few (111) twins is shown in Figure 38(a).

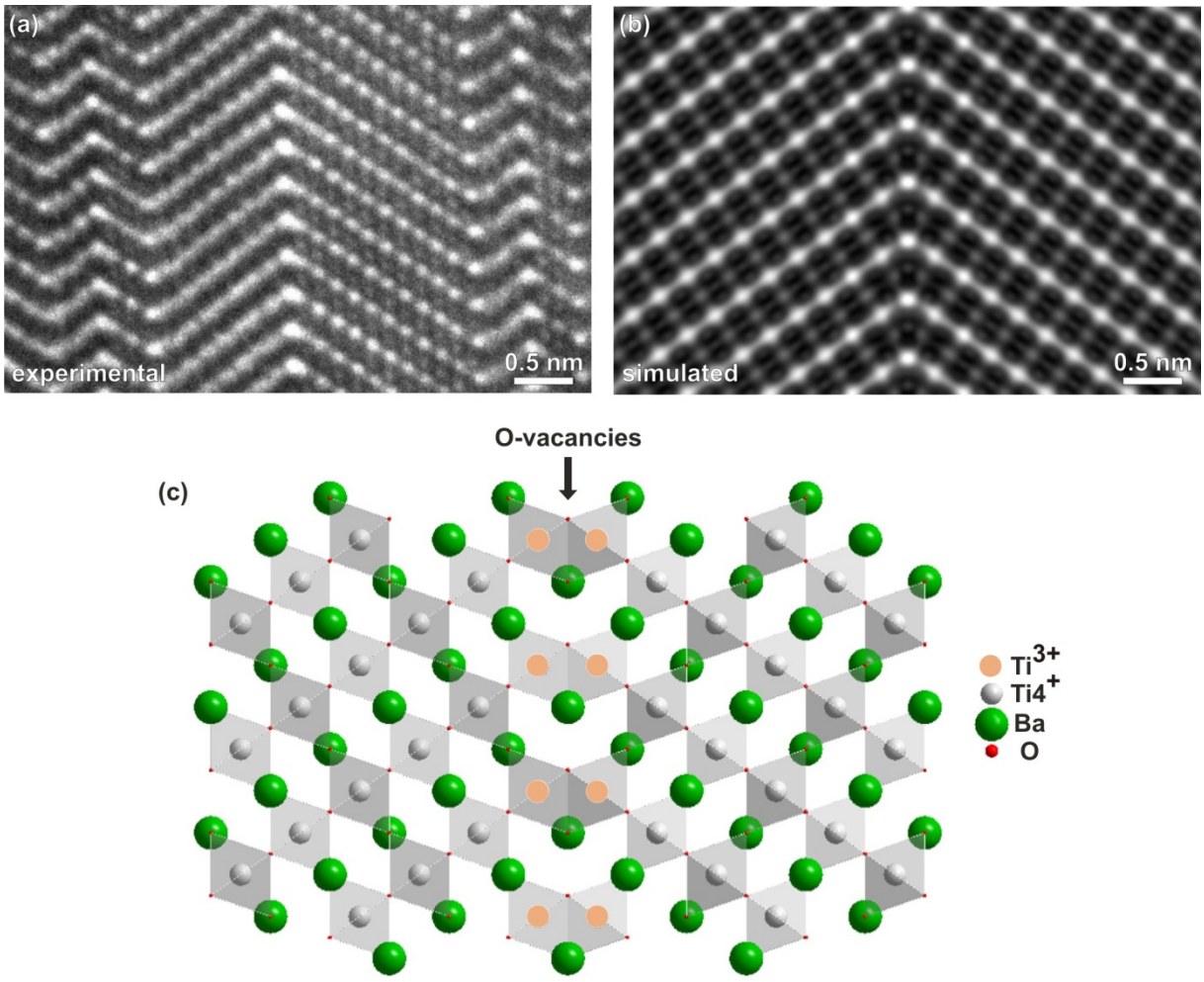

Figure 38. (a) High-resolution HRTEM image of few (111) twins within the slab of disordered hexagonal $BaTiO_3$ polymorph. Bright dots correspond to the Ba-O atom columns. (b) Simulated high-resolution TEM image of a single (111) twin for a thickness of 4 nm and a defocus value of 60 nm. (c) The corresponding structural model of a (111) twin.[124-126]

Bright spots in the HRTEM image correspond to the mixed Ba-O atom columns. The HRTEM image was simulated for a sample thickness of 4 nm and a defocus value of 60 nm (Figure 38(b)). The corresponding structural model of a single (111) twin in Figure 38(c) matched with the experimental image.

The existence of the hexagonal polymorph was previously reported for $BaTiO_3$ particles synthesized by a sol-gel procedure,[119,127] but was so far never observed and reported for $BaTiO_3$ nanostructures obtained by the template-assisted EPD synthesis. According to Rečnik *et al*. the most plausible mechanism for the formation of the hexagonal polymorph is the reduction of Ti^{4+} to Ti^{3+}, resulting from the local reducing atmosphere caused by the decomposition of the organic components of the sol at annealing temperature of 700 °C.[125,126] Namely, Ti^{3+} ions are supposed to initiate the formation of face sharing octahedral in the form of Ti_2O_9 groups which are nucleation sites for hexagonal stacking. As long as the firing atmosphere allows the formation of oxygen vacancies that induce the creation of Ti^{3+} ions, the nucleation of hexagonal stacking would be preferred. In order to confirm that the presence of hexagonal polymorph is really a consequence of the reductive atmosphere during annealing, the AAO templates filled with the BT sol were annealed in a pure-oxygen atmosphere at 10 bar (Figure 39). In this way the annealed $BaTiO_3$ nanorods show an absence of $BaTiO_3$ hexagonal grains (Figure 39(b)).

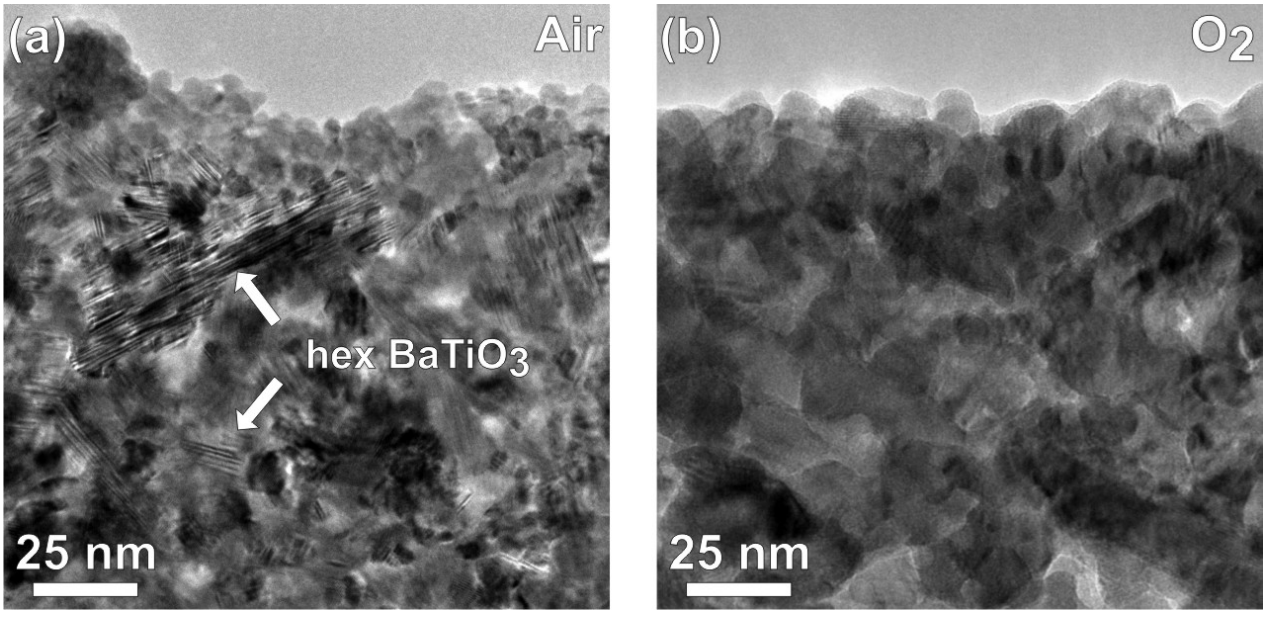

Figure 39. (a) Bright-field TEM image of $BaTiO_3$ nanorod annealed in air showing the presence of pseudo-cubic and hexagonal polymorphs. (b) Bright-field TEM image of $BaTiO_3$ nanorod annealed in a pure-oxygen atmosphere. No hexagonal polymorph is present.

4.2.9 Electrical measurements and device prototyping

Two- and four-probe electrical DC measurements were performed on single $BaTiO_3$ nanorods contacted by FIB nanolithography in the temperature range from 25 ºC to 320 ºC (Figure 40). Linear I-V curves were observed in all cases, demonstrating that ohmic contacts were formed between the platinum electrodes and the nanorods (Figure 41). This point was validated by the good correspondence between the two- and four-probe measurements, which confirmed the low contact resistance R_c arising from the metal-semiconductor interface. Resistivity values between 10 and 100 ohm·cm were found for the ten tested devices. This result is in excellent agreement with typical values reported in the past for oxygen-deficient barium titanate films,[128] and confirms the above-mentioned key role of the vacancies in the formation of hexagonal phase traces in some of the nanocrystals, as well as on the modulation of the electrical response. Actually, the expected resistivity for the intrinsic $BaTiO_3$ is much higher (10^{10} ohm·cm), and it is widely accepted that non-stoichiometric oxygen is a major source of variation for this value. Nevertheless, it remains unclear as to whether these vacancies are compensated by intrinsic Ba, Ti or even acceptor-type impurities.[15,17,18,20,24]

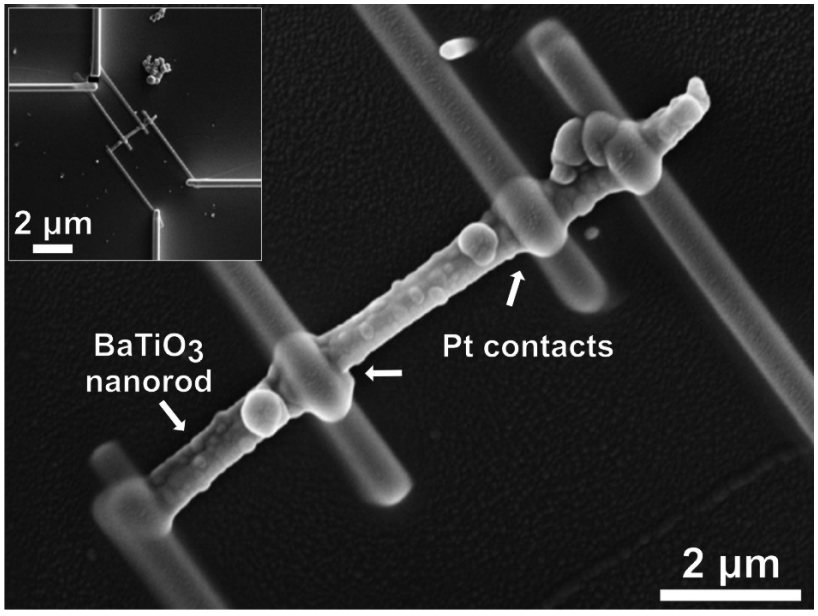

Figure 40. Detail of a $BaTiO_3$ nanorod contacted with FIB nanolithography in a 4-probe configuration. The inset in the upper left corner shows a low-magnification image of the same device. The platinum strips deposited with the FIB are shown.

Increasing the temperature from 25 ºC to 200 ºC did not affect this electrical response largely great deal. However, a sharp drop of the resistance (R) was observed beyond this temperature limit. Figure 41 shows that R follows a reverse S-shape as a function of temperature with two plateaus, the first being located between 25 ºC and 180 ºC, and the second one from 280 ºC and above. It should be pointed out that the response to higher temperatures than 320 ºC was not evaluated herein in order to prevent damaging the pre-patterned Au/Ti/Ni microelectrodes of our chips. This temperature-resistance dependence is explained in terms of the thermally activated electron conduction mechanisms among the nanograins that compose the nanorods. The single-crystal $BaTiO_3$ shows a pure electronic conductivity at temperatures below 535 ºC.[129] Furthermore, each oxygen vacancy is expected to provide two electrons to the material.[130] Therefore, electrons are likely to be the main charge carriers in our samples and the most responsible for the observed resistance behaviour. Actually, they must overcome grain-boundary barriers that dominate the current transport. Thus, free electrons with enough energy overcome the potential barriers at elevated temperatures, improving the effective conductivity of these devices, as the experimental evidence shows.

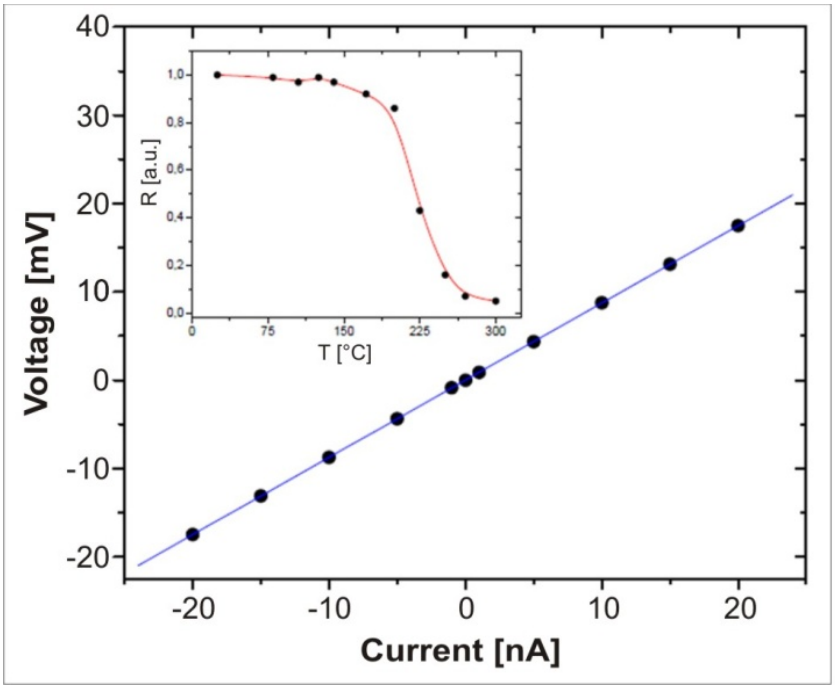

Figure 41. Four-probe I-V response of an individual $BaTiO_3$ nanorod measured at room temperature. A perfect ohmic behaviour is observed. The inset in the upper left corner shows the temperature dependence of the electrical resistance (R) of a $BaTiO_3$ nanorod. A sharp drop of R is observed above 200 °C.

Finally, the feasibility of prototyping functional devices based on individual $BaTiO_3$ nanorods was successfully evaluated. Some of them were tested as proof-of-concept humidity sensors, showing reproducible and scalable responses to different moisture concentrations (Figure 42) and good long-term stability and fast response times. A sharp reduction of R was found in a water-rich atmosphere, which is in excellent agreement with previous results reported in the literature,[20] due to the contribution of the dominant charge carrier (H^+) that is present in high-moisture environments. This result demonstrates that single $BaTiO_3$ nanorod-based devices may be integrated into complex circuit architectures with the functional capacities of a humidity nano-sensor.

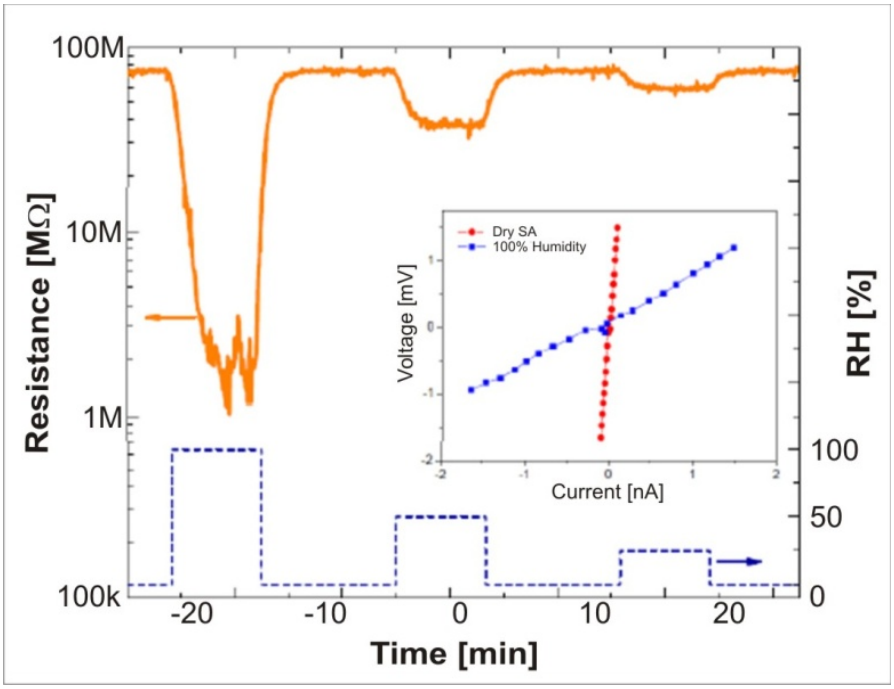

Figure 42. Sensing response of a $BaTiO_3$ nanorod to pulses of 100, 50 and 25 % of relative humidity measured at room temperature. Synthetic air was used herein as a carrier gas. The inset shows I-V curves obtained in dry and humid (100 % relative humidity) air. A sharp and reversible modulation of the electrical response was observed.

4.3 Formation of $SrTiO_3$ nanotubes

4.3.1 Pure $SrTiO_3$ nanotubes

Our procedure of synthesizing perovskite 1-D nanostructures was also implemented on $SrTiO_3$. The processing parameters for EPD process were similar as for the synthesis of $BaTiO_3$ nanorods. EPD was conducted at 30 V for 30 min followed by annealing at 700 °C for 1 h and the removal of the AAO template. $SrTiO_3$ nanotubes grown within the AAO template membranes were polycrystalline and had inner diameters ranging from 150 to 180 nm, outer diameters ranging from 200 to 250 nm and an average length of 10-25 μm. After characterization of the formed $SrTiO_3$ nanotubes by various electron-microscopy techniques we observed an unusual crystallization phenomenon that manifested itself in the self-assembly of $SrTiO_3$ nanocrystallites. This unique mechanism of self-assembly of (001)-oriented $SrTiO_3$ nanocrystals self-organized in a tubular morphology was not yet observed in any materials grown by template-assisted EPD.

4.3.1.1 Processing of $SrTiO_3$ nanotubes by sol-gel EPD into AAO templates and subsequent annealing

As a template for the electrophoretic deposition of a ST sol into the pores AAO membranes were used. After annealing and the removal of the AAO template, isolated fibres tend to cluster into bundles and flakes of various dimensions (Figure 43).

X-ray powder diffraction (Figure 44) of the product after removing the AAO template confirmed the presence of crystalline cubic $SrTiO_3$ (JCPSD card No. 89-4934). Since no other compounds were detected by XRD apart from $SrTiO_3$, it can be concluded that there no chemical reactions took place between the Al_2O_3 template and $SrTiO_3$ at the annealing temperature of 700 °C. At first glance the nanotubes have a uniform diameter and relatively smooth surface over much of their length. They are generally shorter than the actual thickness of the template, which is due to fracturing during the template removal. The inset of Figure 43 is a high-magnification FSEM image of fractured tubes, showing that the $SrTiO_3$ crystallized in the AAO templates has indeed a tube-like morphology.

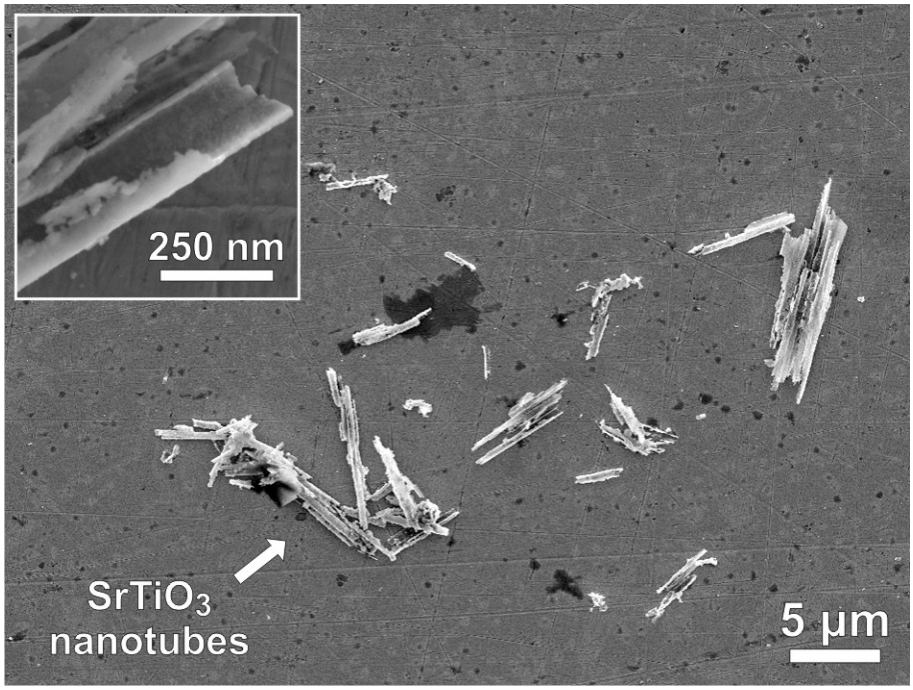

Figure 43. FSEM image of isolated and bundled $SrTiO_3$ nanostructures prepared by sol-gel EPD in AAO template and annealed at 700 °C for 1 h. Higher magnification in the upper left corner (inset) shows fractured $SrTiO_3$ tubes.

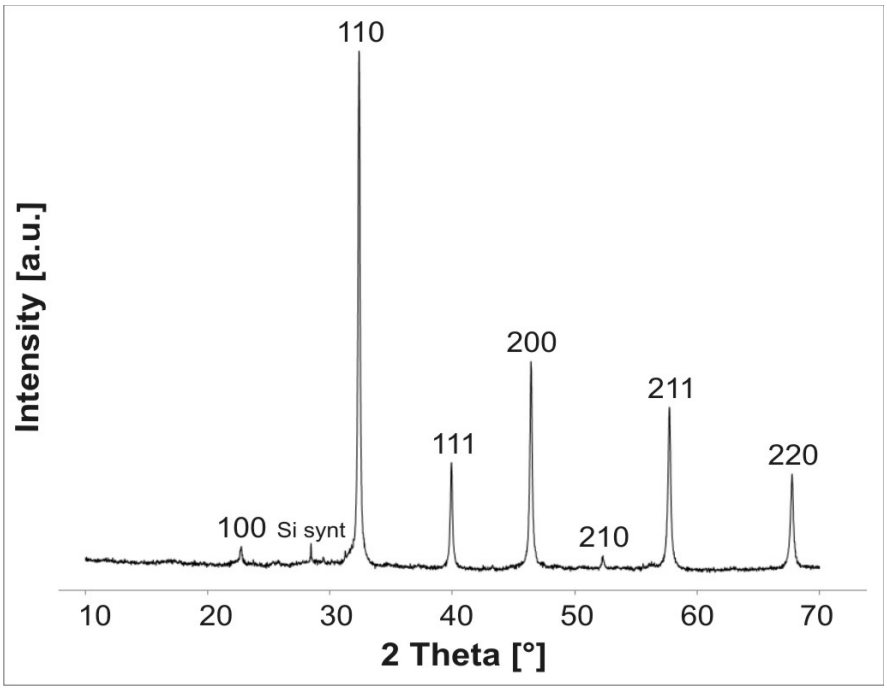

Figure 44. XRD spectrum recorded from tube-like $SrTiO_3$ nanostructures after annealing and removal of the AAO template showing only the presence of diffraction peaks corresponding to cubic $SrTiO_3$. For XRD measurements $SrTiO_3$ nanotubes were deposited on a single Si crystal. No residual Al_2O_3 from the template could be detected in the spectra.

The $SrTiO_3$ samples were further studied by TEM. Figure 45 shows a low-magnification bright-field TEM image of a typical $SrTiO_3$ nanotube after annealing and removal from the AAO template. The nanotubes have diameters of approximately 200 nm, which is comparable to the diameter of the AAO template pores. The nanotube walls are composed of polycrystalline $SrTiO_3$, which occasionally appears in the form of cube-like nanocrystals of various sizes. The darker contrast of the walls implies that these nanostructures are indeed hollow. To additionally confirm that the product possesses a tubular morphology, the samples were sliced with an ultra-microtome; the random cross-sections through the bundles of $SrTiO_3$ nanotubes confirmed our expectations. In Figure 45(b) and (c) axial and radial cross-sections of $SrTiO_3$ nanotubes deposited on a lacy carbon-coated Cu-grid are shown, respectively. An axial cut through a particle of $SrTiO_3$ nanotubes in Figure 45(b) shows that the nanotube walls can be relatively thin, however even in thicker segments of nanotubes the thickness of the deposited $SrTiO_3$ never exceeds one tenth of their diameter.

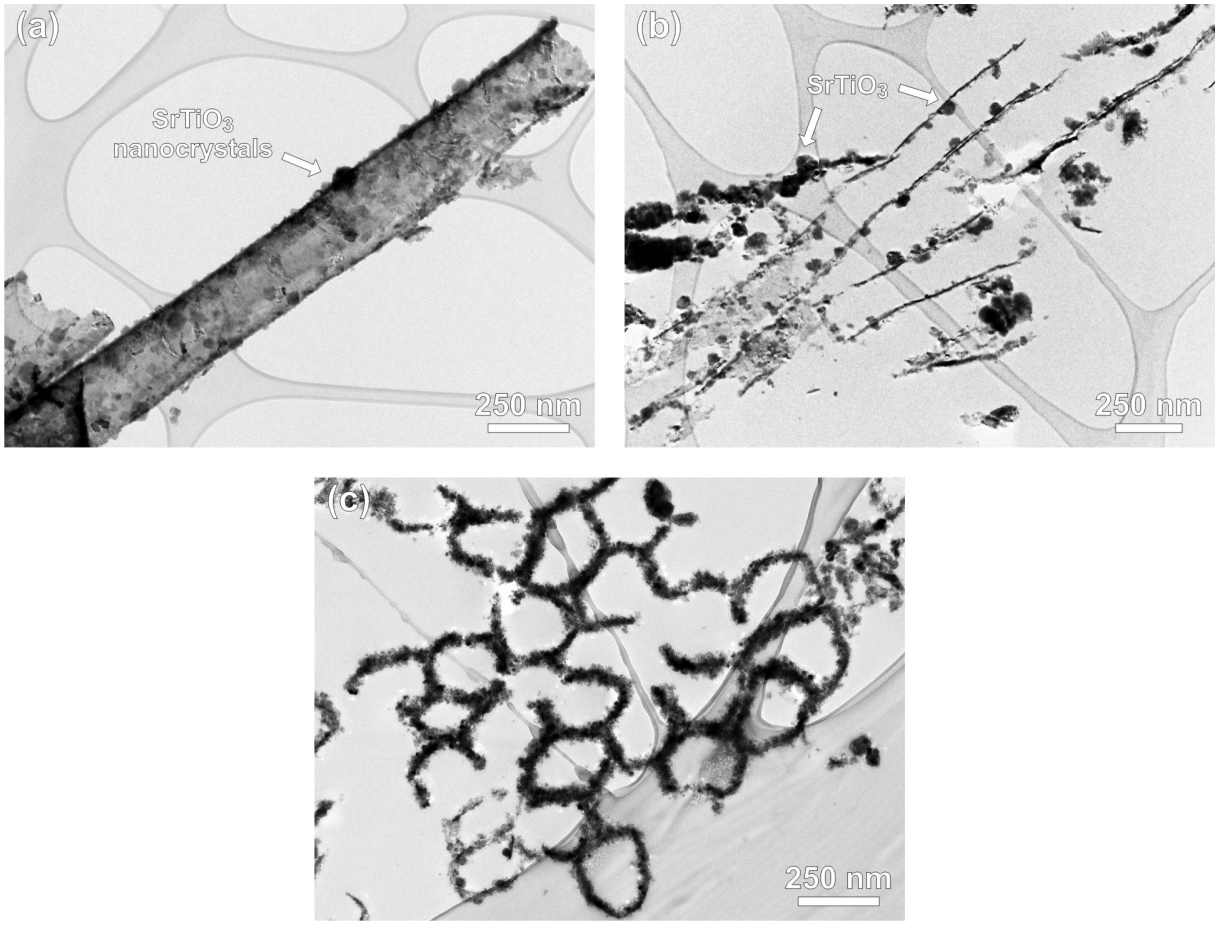

Figure 45. TEM micrographs of $SrTiO_3$ nanotubes after annealing and leaching from the Al_2O_3 membrane. (a) Typical uniformly shaped nanotube with a thin wall composed of $SrTiO_3$ nanocrystals of various sizes and orientations. Bright-field TEM image of an (b) axial and (c) radial ultra-microtomic cross-section of inhomogeneously crystallized segment of multiple $SrTiO_3$ nanotubes deposited on a lacy-carbon coated TEM grid.

The low-magnification bright-field TEM image in Figure 46 shows the presence of Y-junctions and branches after leaching of the $SrTiO_3$ nanotubes from the AAO templates. The reason for the existence of the Y-junctions and "branches" lies in the morphology of AAO pores.[113] The AAO template has a complex channel structure (see Figure 17(d)) and the $SrTiO_3$ nanotubes perfectly copy this three-dimensional structure of the AAO template. Therefore, not only straight nanotubes can be formed in AAO templates but also nanotubes in the shape of Y-junctions and branches are present in small amounts as well.

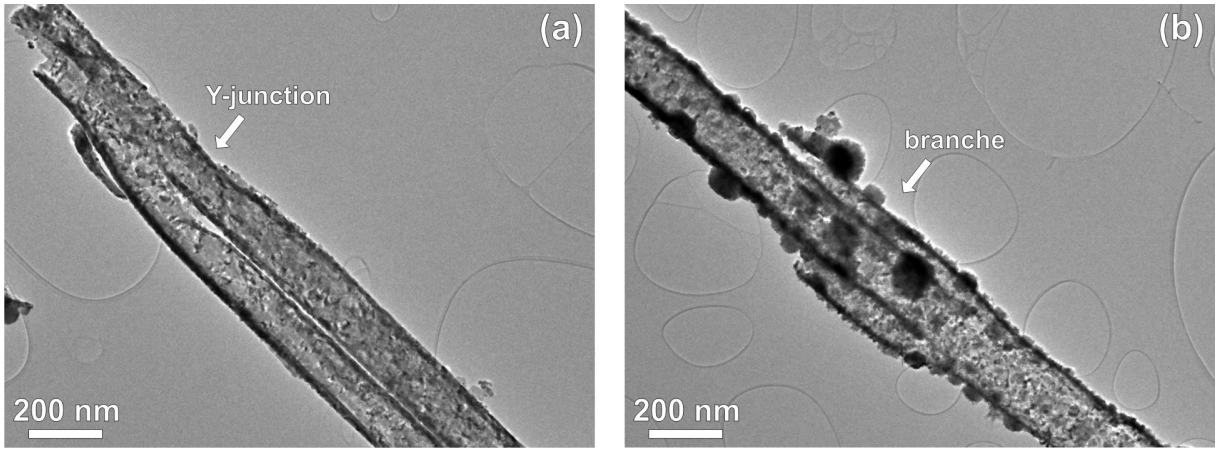

Figure 46. Bright-field TEM image of an (a) Y-junction and (b) "branched" $SrTiO_3$ nanotubes deposited on a lacy-carbon coated TEM grid.

4.3.1.2 Chemical composition of $SrTiO_3$ nanotubes

The chemical composition of the $SrTiO_3$ nanotubes was studied by EDXS. EDXS spectra were recorded from 5 regions along the nanotubes shown in Figure 47(a). Apart from Sr and Ti peaks no additional peaks for Al, Na and Si that could originate from the incomplete removal of the AAO template could be observed. The chemical composition listed in Table 9 suggests that $SrTiO_3$ nanoparticles are stoichiometric. No faults such as antiphase boundaries or Maguelli phases could be observed at higher magnifications.

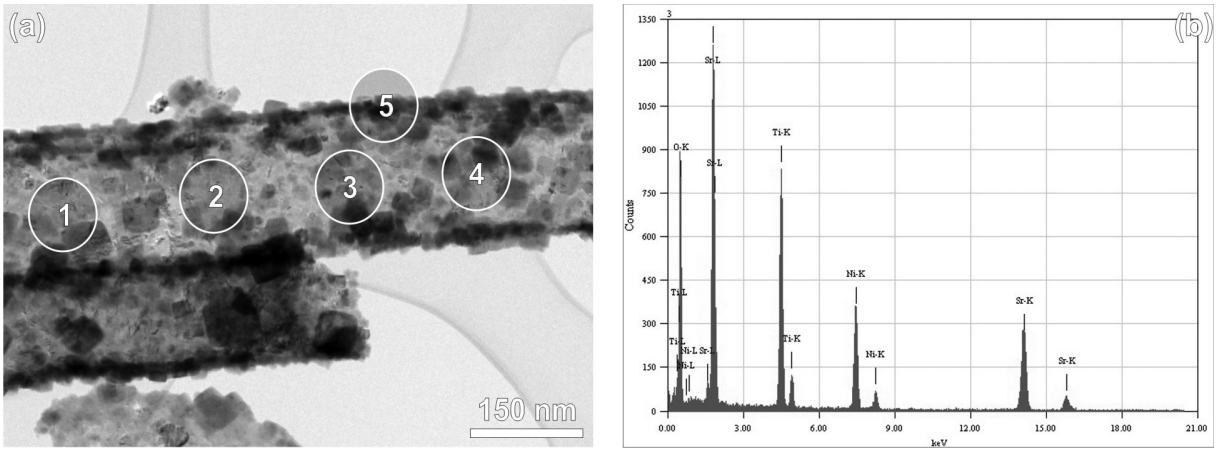

Figure 47. EDXS analysis from a single $SrTiO_3$ nanotube. (a) Positions of acquisition of the EDXS spectra. (b) EDXS spectrum showing only the presence of Sr and Ti. Ni peak corresponds to the carbon-coated Ni-grid where the $SrTiO_3$ tubes were dispersed.

Table 9. Results of the quantitative EDX analysis from the marked regions on the $SrTiO_3$ nanotube (Figure 47).

Region	1	2	3	4	5
Ti K (at. %)	20.0±0.1	19.6±0.1	20.0±0.1	20.0±0.1	19.8±0.1
Sr L (at. %)	20.0±0.2	20.5±0.2	19.9±0.2	19.9±0.2	20.3±0.2

4.3.1.3 Oriented cube-on-cube nanocrystal assembly within the $SrTiO_3$ tubes

Depending on the annealing temperature and the rate of nucleation, smaller or larger crystals are formed from the amorphous ST sol-gel. At an annealing temperature of 700°C we have observed an optimum crystallization of $SrTiO_3$ in the AAO pores; at lower temperatures the material is found to be amorphous, whereas at higher temperatures the $SrTiO_3$ strongly binds to the Al_2O_3 template and its removal becomes increasingly difficult. In order to allow the efficient condensation and subsequent dehydration a very slow heating rate was used. Similar processing conditions have been suggested by previous authors.[50] Because of the turbulent release of gaseous products at higher heating rates the nanotubes tend to crack, and moreover, homogeneous nucleation and the self-assembly of $SrTiO_3$ nanocrystals does not take place. Therefore, the heating rate appears to be the most critical processing parameter in the nucleation stage. Different annealing times were found to influence the degree of $SrTiO_3$ crystallization. After too short annealing times the product remained amorphous-to-nanocrystalline without evident self-arrangement of $SrTiO_3$ nanocrystals, whereas prolonged annealing did not significantly affect the further crystallization or rearrangement of $SrTiO_3$ nanocrystals. A quick inspection of the sample shows that the $SrTiO_3$ nanotubes are quite inhomogeneously crystallized after a selected annealing time. Often, only some parts of the nanotube display large idiomorphic $SrTiO_3$ crystals, whereas the other parts are finely crystalline or even amorphous.

Figure 48 illustrates such a gradual transition from fine crystalline $SrTiO_3$ without any distinct morphology or orientation relationship towards the coarse crystalline $SrTiO_3$ with a evident cube morphology and special crystallographic relation among the crystals within a single nanotube. The $SrTiO_3$ cubes are well discernable at the right end of the nanotube in Figure 48(a). Their size progressively decreases towards the central part of the micrograph, where they fade in the finely crystallized section. Selected-area electron diffraction (SAED) patterns (Figure 48(b)-(e)) recorded on marked areas in Figure 48(a) demonstrate the degree of crystallinity, as well as ordering of the $SrTiO_3$ nanocrystals. The first pattern from the poorly crystallized area of the nanotube, shown in Figure 48(b), reveals that $SrTiO_3$ is nanocrystalline without any preferential orientation, neither among the crystals nor relative to the nanotube. The diffraction rings match the *d*-values of the $SrTiO_3$, implying that this section corresponds to one of the outer ends of the nanotube. The next diffraction pattern, shown in Figure 48(c), already reveals quite interesting crystallographic features. While in general, we are still observing diffraction rings originating from nanocrystalline $SrTiO_3$, the intensities related to the (200) and (020) reflections show a peculiar angular spread, implying that particles (domains) of cube nanocrystals in a

cube-on-cube orientation are present, however with no other preferential alignment. In the next pattern, shown in Figure 48(d), the angular spread of the (200) and (020) reflections becomes narrower. This condition corresponds to a situation where domains of cube-on-cube oriented crystals make a touch-down to the nanotube walls. In films thinner than the cube diameter the crystals tend to orient with their faces towards the nanotube walls, while any kind of edge- and corner-to-wall orientations are no longer permitted. The last step of self-alignment takes place when the size of the crystals becomes comparable with the curvature of the nanotube. The pattern in Figure 48(e) reveals sharp diffraction spots that normally would result from a single crystal and not a polycrystalline material. Such a diffraction pattern can only be produced when all the nanocrystals are aligned in a more or less identical crystallographic orientation. Minor spot splitting indicates that some of the nanocrystals may be slightly rotated from the general orientation of the crystallites, *i.e.,* parallel to the nanotube axis. Even more surprisingly, not only that the nanocrystals within the selected area (marked in Figure 48(a)) are met in a common orientation, but they are apparently aligned along the nanotube axis.

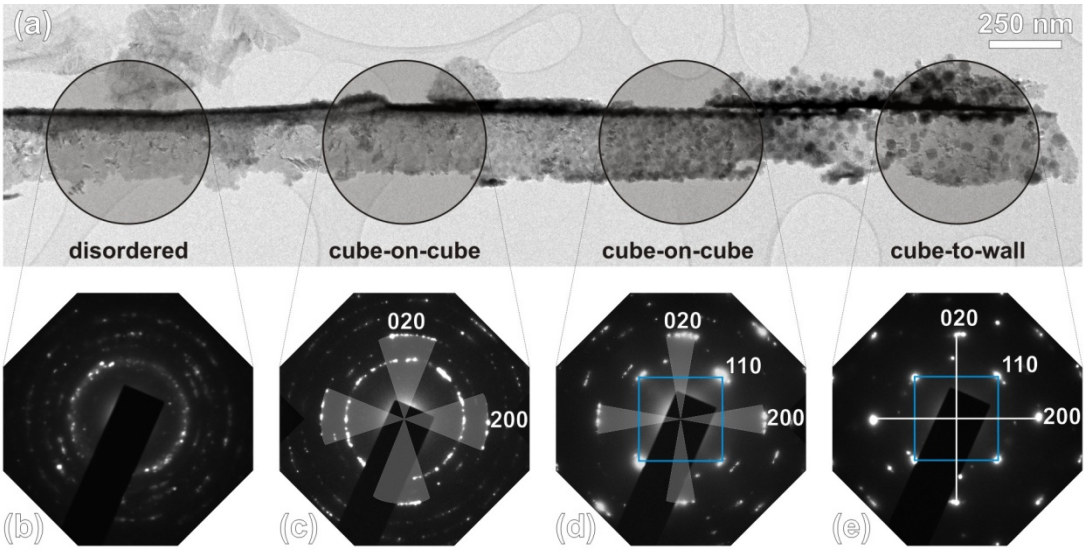

Figure 48. (a) Bright-field TEM image of polycrystalline $SrTiO_3$ nanotube grown in AAO template with the corresponding SAED patterns recorded on four sections of the nanotube (shown in the TEM image): (b) Area of completely disordered nanocrystalline material; the diffraction rings correspond to the d-values of $SrTiO_3$. (c) Nanocrystalline $SrTiO_3$ with partial cube-on-cube orientation evident from the angular spread of the (020) and (200) reflections. (d) Cube-on-cube and alignment and (e) complete alignment of the cubes along the nanotube axis.

The reason for the tubular morphology of $SrTiO_3$ nanotubes lies in the crystallization process that takes place inside the one-dimensional pore channels during the annealing of the AAO templates infiltrated with the ST sol-gel. Sol-gel processing consists of the hydrolysis and condensation reactions of precursors, where surface-charged nanoparticles with the desired stoichiometry are formed. Electrostatic stabilization of the nanoparticles in the sol prevents their agglomeration.[69] After the application of an external electric field, positively charged sol particles start to move due to electrophoresis towards the working electrode, while counter ions move in the opposite direction.[8] Depending on the applied voltage and the duration of the deposition the pores of the membrane are gradually filled-up with a precursor sol-gel. The infiltrated material was found to be amorphous by X-ray analysis, and only upon annealing $SrTiO_3$ starts to form inside the AAO template pores. After initial dehydration, chelated precursors start to decompose with a significant release of H_2O, CO and CO_2 at higher temperatures. As a result of the pyrolysis and calcination with a further release of gaseous products, ST sol-gel starts to crystallize in form of nanosized crystals. $SrTiO_3$ crystals nucleate

homogeneously near the free surface of the yet unreacted sol-gel, whereas in the centre of the pores, the free path for the outlet of gaseous reaction products is gradually widening. Near the open ends of the pores, where the gas exhaust is most efficient, the nucleation rate is the highest, while towards the tube interior the $SrTiO_3$ nucleation rate drops drastically because of the reduced backflow of gases. An increasing partial pressure of gaseous products slows down the reaction rate, which is readily reflected through limited nucleation of $SrTiO_3$. Because of this non-equilibrium condition many more nuclei are formed near the open ends than deep in the interior during the initial stages of annealing. In the nucleation stage the crystals have no preferential orientation, neither with respect to the nanotube axis nor among themselves. Near the outlets most of the precursor material is used for $SrTiO_3$ crystallization already in the nucleation stage and not much of the reactants are left for a subsequent crystal growth. In these sections of the nanotubes we therefore observe randomly oriented nanocrystalline $SrTiO_3$ grains with no distinct morphology. Only when the crystals undergo a growth process their morphology starts to evolve into idiomorphic cubes. Such conditions can be found in the nanotube interior where the increasing large counter-pressure of gaseous products hinders the rapid crystallization. In the interior, less nuclei are formed and therefore more material is available for crystal growth. During growth the $SrTiO_3$ crystals adopt perfect cube morphology. As the precursor material is being slowly consumed they gradually approach the nanotube walls together with the depleting mass of the un-reacted sol-gel, which acts as a viscous semi-fluid medium. On their path towards the nanotube walls the crystals progressively gain in size to a point when they are brought into such close contacts that the repulsive electrostatic forces become significant. Under steric constraints of a thin layer the significance of these interactions becomes dominant and crystals start to locally arrange themselves into a simple cube-on-cube orientation, allowing the most efficient packing within the available space. If at the touch-down to the nanotube walls the crystals are relatively small the curvature of the nanotube does not have any special effect on the crystal orientation, however if their diameters are comparable with the tube curvature radius before they completed their growth they will tend to adjust and orient parallel with the nanotube axis. This mechanism is illustrated in Figure 49.

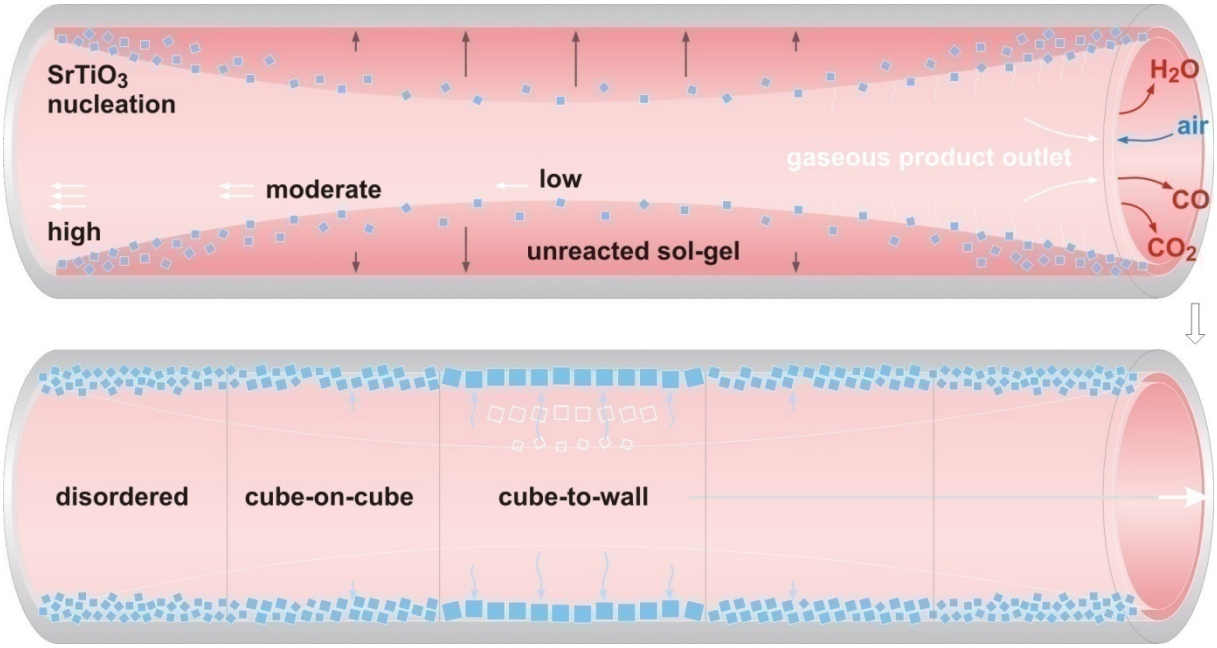

Figure 49. Nucleation and crystallization processes during annealing. The illustration shows simultaneous pyrolysis and nucleation processes that take place during the annealing of $SrTiO_3$ nanotubes. A high nucleation rate at the nanotube outlets leads to the formation of numerous randomly oriented $SrTiO_3$ nanocrystals. In the nanotube, interior crystals continue with their growth and adopt special cube-on-cube and cube to-wall orientations.

The concerted self-assembly of $SrTiO_3$ nanocrystals is further demonstrated by selected close-up images in Figure 50. A typical domain arrangement of nanocrystals is presented in Figure 50(a), where the larger crystals at the upper wall of the nanotube are aligned normal to the nanotube axis, whereas smaller crystals at the lower right side form two separate domains with their own local orientation. A more perfect cube-to-wall alignment is shown in Figure 50(b), where all the larger cubes of $SrTiO_3$ are almost ideally lined along the tube axis. If $SrTiO_3$ crystals have ample time for crystallization (central segments of nanotubes) they grow into perfect cubes. Such a perfectly defined crystal shape is one of the fundamental prerequisites for cube-on-cube and for the cube-to-wall alignment. At higher magnifications we regularly observe an about 1-nm-thick amorphous layer between the cube-on-cube oriented $SrTiO_3$ crystals. Amorphous precursors serve as a common medium for crystal translations during annealing. A relatively high population of fully grown cubic crystals perfectly self-organized along the cube-on-cube orientation along the nanotube axis, is shown in Figure 51 (a) and (b).

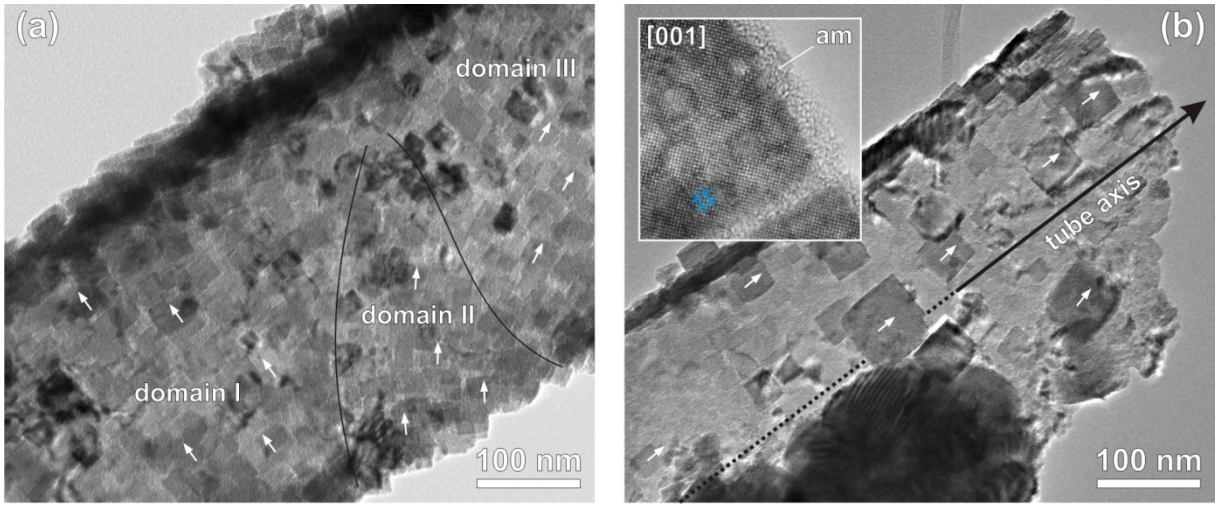

Figure 50. Bright-field TEM images of self-organized sections of $SrTiO_3$ nanotubes. (a) High-population of cubic crystals where domains of self-assembled $SrTiO_3$ nanocrystals can be observed. (b) Larger cubic crystals almost perfectly aligned into a cube-on-cube orientation parallel to the nanotube walls. The inset presents a HRTEM detail from a $SrTiO_3$ nanocrystal in the [001] zone axis with frozen intercrystalline amorphous phase over which the crystals are aligned and receive nutrients for their growth.

Homogeneous nucleation that produces a critical number of crystallites leads to their self-organization when the crystals reach the sizes that are equal the mean free distance between the nuclei. Due to steric constraints the crystals start to self-organize in order to most efficiently fill the available surface of the pore walls. This process leads to the formation of domains containing large numbers of nanocrystals, which are self-aligned in more or less identical crystallographic orientation (Figure 50(a)). When the size of the crystals is increased the diameter of the pore in which they are growing becomes an important parameter in their alignment. If the crystal size is comparable to the pore diameter the curvature of the pore walls influences the alignment in such a manner that the crystal edges orient parallel with the nanotube axis (Figure 50(b)). In this way the contact area between the crystal and the wall is maximized. The larger crystals thus align parallel with the nanotube walls while the smaller adopt the orientation of the larger ones according to the self-organizing mechanism described above (see illustration in Figure 52). The observed priority of cube-to-wall alignment indicates that there must be some attractive force (adhesion) between the $SrTiO_3$ nanocrystals and the AAO pore walls, whereas the mechanism of cube-on-cube alignment of $SrTiO_3$ nanocrystals is controlled by the inter-crystal repulsion forces.

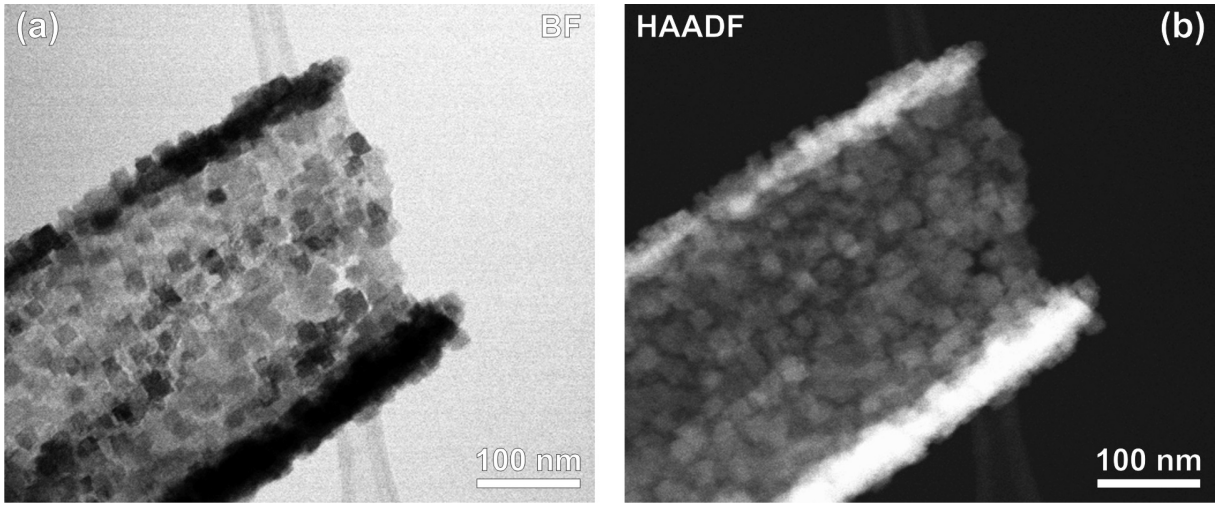

Figure 51. (c) Bright-field STEM and (d) HAADF-STEM image of highly organized $SrTiO_3$ nanotube.

An almost perfect alignment suggests a high level of self-organization of $SrTiO_3$ nanocrystals during their nucleation and growth following a sequence of successive mechanisms illustrated in Figure 52 whereas Figure 53 shows a schematic structural model of ideally self-assembled nanotube consisting of numerous $SrTiO_3$ nanocrystals perfectly aligned with each other and parallel to the nanotube axis. The whole process is best compared with a drying drop of saline water, where tiny cubes of halite form at the drop surface, where water evaporation is most intense and local concentration of the brine is the highest.[131] As the drop dries the crystals at the meniscus grow and descend towards the base. During their descent growing cubes start to align into a cube-on-cube orientation. On a flat support the crystals in the thin film will tend to align with their faces parallel to the underlying surface. In a concave, tubular geometry, however, the two-dimensional (rotational) degree of freedom is reduced to one dimension and the crystals line-up along the nanotube axis. While in the case of a saline drop we only have simple evaporation/crystallization process the background reactions that trigger the crystallization of $SrTiO_3$ nanocrystals in pores of the AAO template is more complex, but nevertheless the self-assembly mechanisms of crystallizing solids are in both instances comparable.

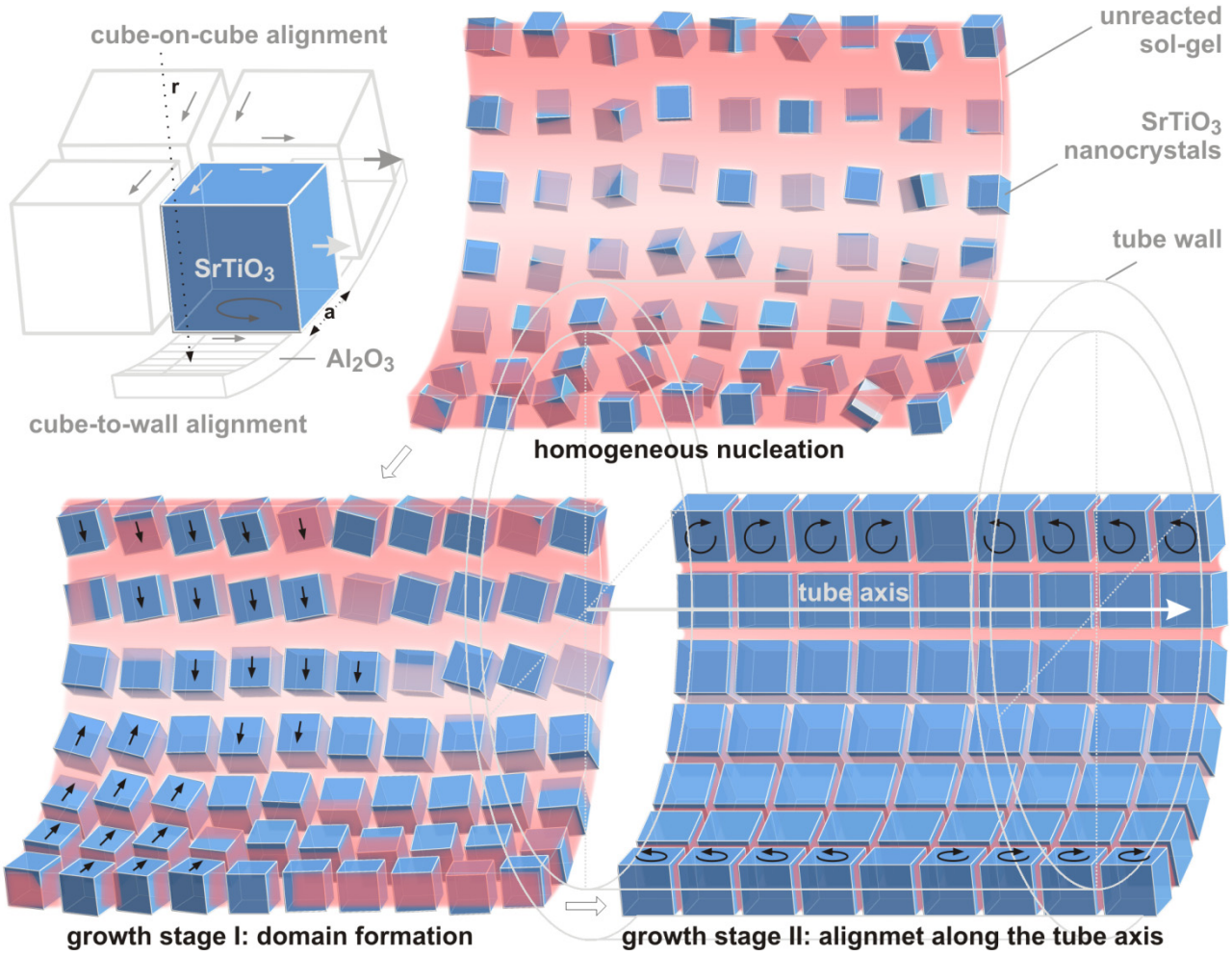

Figure 52. Self-assembly of $SrTiO_3$ nanocrystals in tubular geometry. The process of self-assembly of $SrTiO_3$ nanocrystals in AAO templates comprises three basic mechanisms: (i) homogeneous nucleation of $SrTiO_3$ crystals in the thin film of the precursor sol-gel, (ii) domain formation due to cube-on-cube alignment of $SrTiO_3$ nanocrystals and (iii) final cube-to-wall alignment. The nucleation mechanism is controlled by the reaction of chelate precursors and the efficiency of the removal of gaseous products. Under relatively high counter-pressure of gaseous products the nucleation rate is slow. The crystals nucleate in random orientations near the open surface of the unreacted sol-gel where the evaporation of the gases is most efficient. During growth the crystals are brought into close contacts and begin to align in simple cube-on-cube orientations due to short-range inter-crystal repulsion forces. During growth domains of more or less ordered $SrTiO_3$ nanocrystals are formed. In the final stage of growth when most of the precursor material is used for crystallization the crystals touch the nanotube walls. Due to adhesion forces large crystals orient parallel with the nanotube axis, while smaller crystals adopt their orientations according to the cube-on-cube repulsion forces.

By optimizing the processing parameters to control the rates of nucleation and growth as well as the morphology of nanocrystals one should be able to design layers of any desired material in a chosen crystallographic orientation in virtually any kind of geometry. The synthesis conditions will have to be optimized to achieve conditions of homogeneous nucleation and the assembly will be dictated by the crystallography of the nanocrystal units and their oriented attachment in constrained geometries.

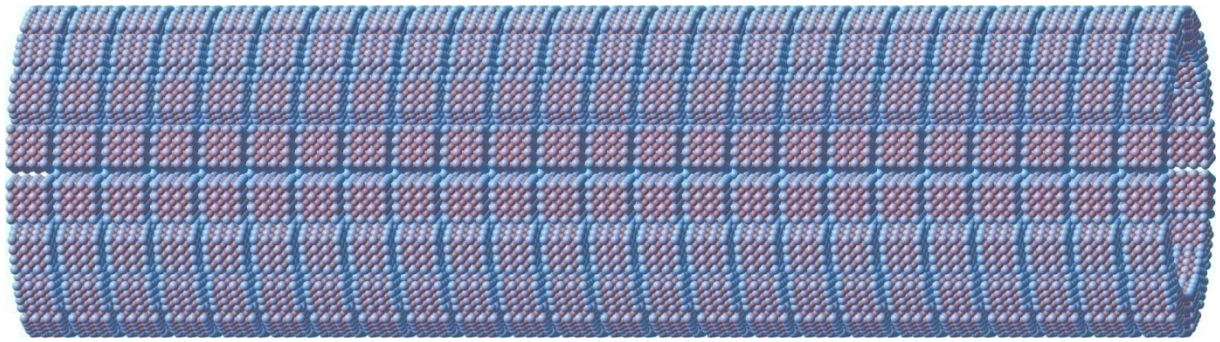

Figure 53. An idealized model of self-assembled $SrTiO_3$ nanotube: A schematic structural model of an ideal self-assembled nanotube consisting of numerous $SrTiO_3$ nanocrystals perfectly aligned with each other and parallel to the nanotube axis.

4.3.1.4 Scanning transmission electron tomography

For 3-D characterization of the nanotubes, electron tomography using HAADF-STEM images was applied. In order to reconstruct a 3-D object using an electron tomography approach, a series of images (projections) must be acquired at angular increments by tilting the nanotubes about the eucentric axis of the specimen holder rod, from one extreme of the tilt range to the other. Each projection in real space is equivalent to a central slice in Fourier space and thus, by recording images at subsequent tilts, the 3-D Fourier space of the object is built up slice by slice. The reconstruction is achieved by using the back-projection method. Using a sufficient number of projections, recorded from different tilt angles, the superposition of all back-projections produces a 3D image of the original object.[132]

Figure 54 shows three voltex projections of $SrTiO_3$ nanotube from the SIRT reconstructions of this tilt series. The 3D reconstruction was built from a series of 73 HAADF-STEM images taken at 200 kV from -74° to +72° in 2° steps. $SrTiO_3$ nanocrystals observed in the nanotube are well resolved and one can see that the cubes are orientated into cube-to-cube domains.

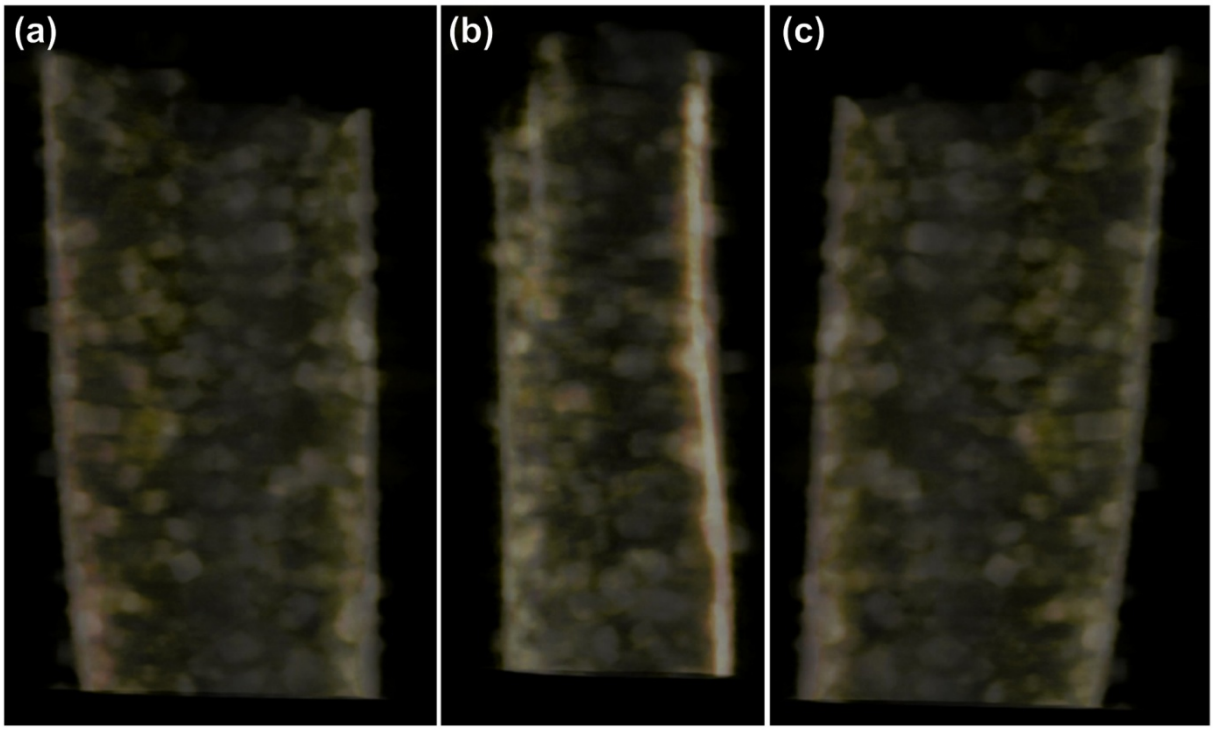

Figure 54. Several voltex projections of a $SrTiO_3$ nanotube using the 3D reconstructed volume at (a) 0, (b) 90 and (c) 180 degrees.

4.3.2 Fe-doped $SrTiO_3$ nanotubes

4.3.2.1. Synthesis and microstructural characterization of Fe-doped $SrTiO_3$ nanotubes

In addition to stoichiometric $SrTiO_3$ nanotubes, Fe-doped $SrTiO_3$ nanotubes were also prepared. Namely, it is known that Fe^{3+} can replace Ti^{4+} on the B sites in the perovskite structure and as a result, oxygen vacancies are formed.[133,134] In this way $SrTiO_3$ becomes an n-type semiconductor and it has many potential applications, among which it can also be used as an oxygen sensor.[35] In view of this, the main objective of preparation of $SrTiO_3$ nanotubes with small amounts of iron was to obtain the material with increased electrical conductivity and to explore the possibility of functionalizing this material by measurements of the electrical properties on Fe-doped $SrTiO_3$ nanotubes.

The Fe-doped $SrTiO_3$ nanotubes were prepared by the same route as the un-doped $SrTiO_3$ nanotubes. Iron, titanium and strontium contents in the starting sol were adjusted so that the final composition of the nanotubes after annealing would give the material with iron replacing approximately 2 mol% of Ti in $SrTiO_3$ according to the formula $Sr(Ti_{0.98}Fe_{0.02})O_{3-y}$. Bright-field TEM revealed that iron-doped $SrTiO_3$ nanotubes exhibit a similar shape to the pure $SrTiO_3$ nanotubes (Figure 55). A typical Fe-doped nanotube had a diameter of approximately 200 nm with a very small grain size ranging from 5 to 10 nm. The EDXS analysis showed only the presence of Sr, Ti and Fe (Figure 55). Quantification of the EDXS confirmed that iron was preferentially incorporated on the B sites in the $SrTiO_3$ structure.

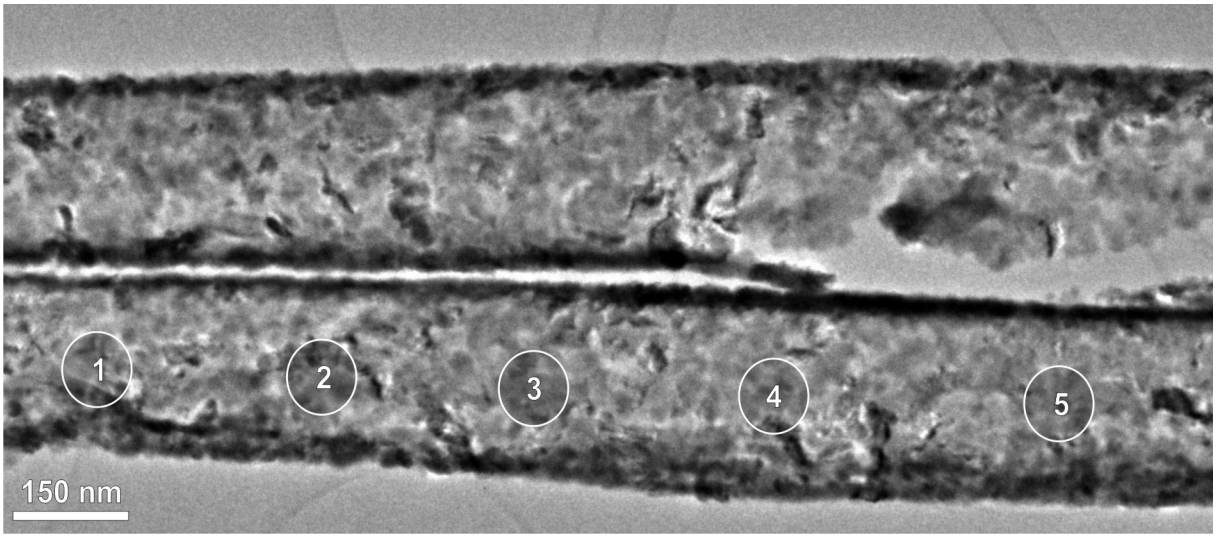

Figure 55. Bright-field TEM micrograph of two Fe-doped $SrTiO_3$ nanotubes with marked regions of EDXS analysis.

Table 10. Results of quantitative EDXS analysis from marked regions on Fe-doped $SrTiO_3$ nanotube.

Region	1	2	3	4	5
Ti K (at. %)	16.8±0.2	17.1±0.2	16.9±0.2	17.1±0.2	17.3±0.2
Sr L (at. %)	21.5±0.3	21.5±0.3	21.7±0.3	21.5±0.3	21.3±0.3
Fe K (at%)	2.6±0.1	2.3±0.1	2.3±0.1	2.2±0.1	2.2±0.1
Sr/Ti+Fe	1.10±0.04	1.10±0.04	1.13±0.04	1.10±0.04	1.09±0.04

4.3.2.2. Electrical and photoresponse characterization of individual Fe-doped $SrTiO_3$ nanotubes

Electrical measurements performed at room temperature revealed linear I-V characteristics, without any direct evidence of a self-heating due to the probing current through the nanotubes (Figure 56). Therefore, it can be asserted that such devices behave almost as perfect ohmic resistors in this temperature range.

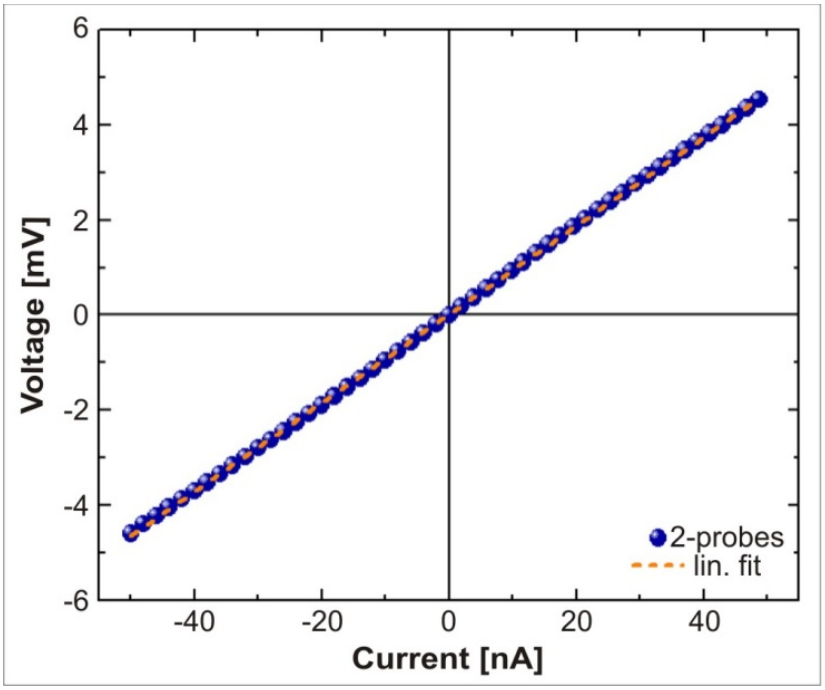

Figure 56. I-V curve of the Fe-doped $SrTiO_3$ nanotube shown in Figure 15. An almost perfect ohmic response is observed at room temperature.

No significant degradation in the above-mentioned properties was observed after several tests, demonstrating that such devices may offer a good reproducibility and prolonged lifespan for future device integration. The electrical resistivity of these nanotubes was estimated for nanotubes with a wall thickness of approximately 20 nm. In the case of the device shown in the Figure 15, a length of 6.4 microns and an external thickness (outer diameter) of 205 nm for Fe-doped $SrTiO_3$ was taken measured by SEM. These dimensions together with the I-V curve in Figure 56 allowed us to determine an electrical resistivity value of 35 ohm·cm (conductivity of 0.0286 ohm·cm^{-1}). This is significantly lower than previous estimations for the bulk resistivity reported in the literature (Figure 57), [135] clearly indicating that the doping of $SrTiO_3$ with iron increases the electrical conductivity. However, possible surface phenomena in the overall electrical response of these devices also cannot be excluded. Namely, it is possible that the

adsorbed moisture on the nanotubes surface changes their electrical conductivity. This possible contribution to increased conductivity will be investigated in future studies.

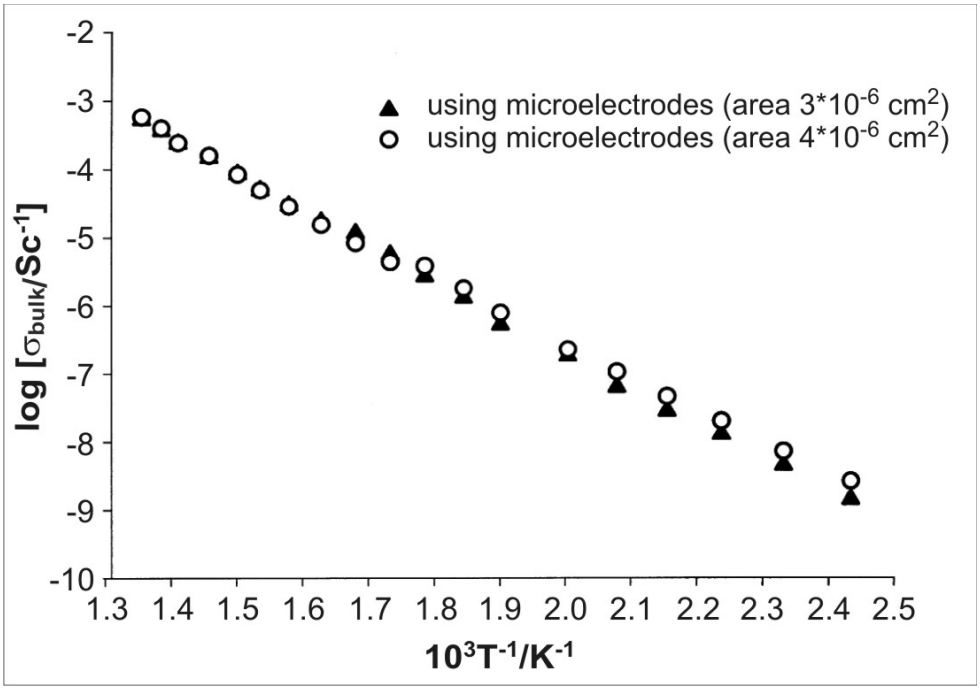

Figure 57. Bulk conductivity of Fe-doped $SrTiO_3$ grains.[135]

Fe-doped $SrTiO_3$ nanotube-based devices were further tested as UV photodetectors in order to assess their potential applications in optoelectronics and gas sensing.[136] Despite the photoresponse of n-type metal oxide nanomaterials, such as ZnO and SnO_2, which have been widely studied, there are no existing studies on titanate nanomaterials. Herein, the theoretical background formalism reported by Prades *et al.* was used to describe and analyze the experimental data.[137]

In Figure 58, the dynamic behaviour of the photoresponse (where I_{ph} is photocurrent) obtained with a single Fe-doped $SrTiO_3$ nanotube as a function of different UV photon fluxes is shown. Repeatable and reversible responses were found in all cases, demonstrating the feasibility of using such prototypes for this purpose. I_{ph} was defined as the change of the total current due to generated carriers by impinging photons.

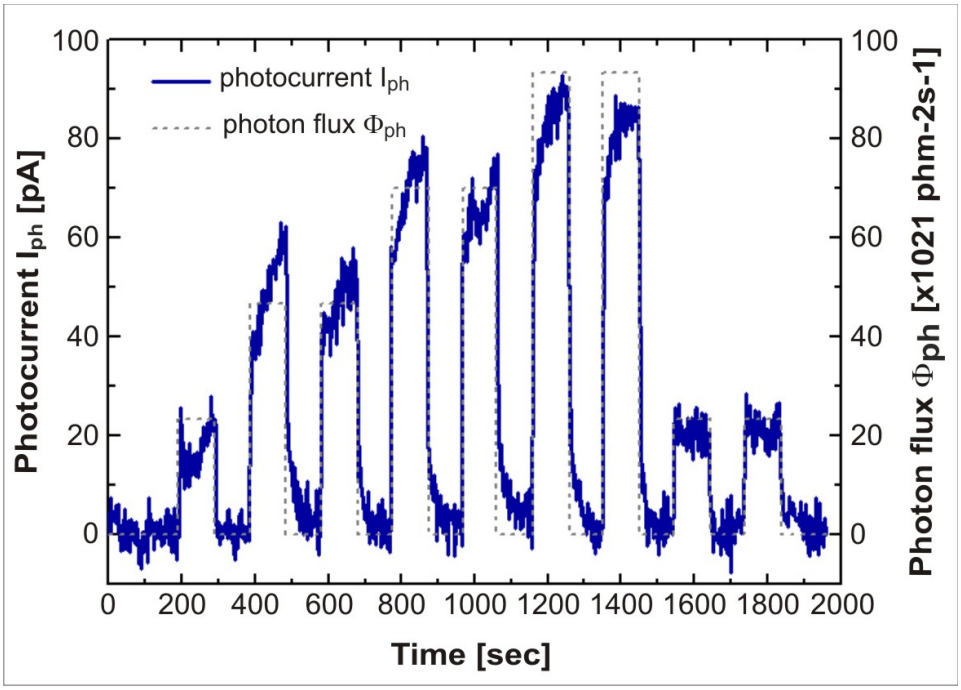

Figure 58. Dynamic behaviour of I_{ph} in a single nanotube as a function of different UV photon fluxes.

A more detailed analysis of photocurrent versus time (Figure 58) reveals response and recovery times in the second range, but always shorter than the 10-second threshold. It is widely accepted that photo-carrier generation-recombination dynamics in nano-oxides like this consists of an initial decay process in the nanosecond range, explained by the fast carrier thermalization and hole-trapping by surface states, followed by a slow decay dependent on the surrounding atmosphere. On the other hand, I_{ph} was found to be directly proportional to the flux of impinging photons on the Fe-doped $SrTiO_3$ nanotubes (Figure 59). This is in good agreement with the theoretical model of Prades *et al.* [137] for nanowire-based photodetectors, and paves the way to the use of these materials in more complex nanodevices.

The performance of these devices can also be analyzed in terms of their normalized photoconductivity gain, g_{ph}, which takes values between 10^{-11} to 10^{-12} m^2/V. [137] These results are poorer than those obtained for crystalline metal oxide nanowires (10^{-5}) and traditional thin film photodectors (10^{-8}).[137] To analyze this value in detail, we must use the definition of g_{ph}, which is given by,

$$g_{ph} = \frac{L^2 G_{ph}}{V} \approx \eta \tau \mu^* \qquad (21)$$

Where L is the length of the nanotubes, G_{ph} is the photoconductive gain, V is the applied voltage, η is the quantum efficiency of the carrier generation by one photon, τ is the carrier lifetime and μ^* is the effective carrier mobility inside the nanorod. According to the experimental data plotted in Figure 58, τ takes values around 90 s.

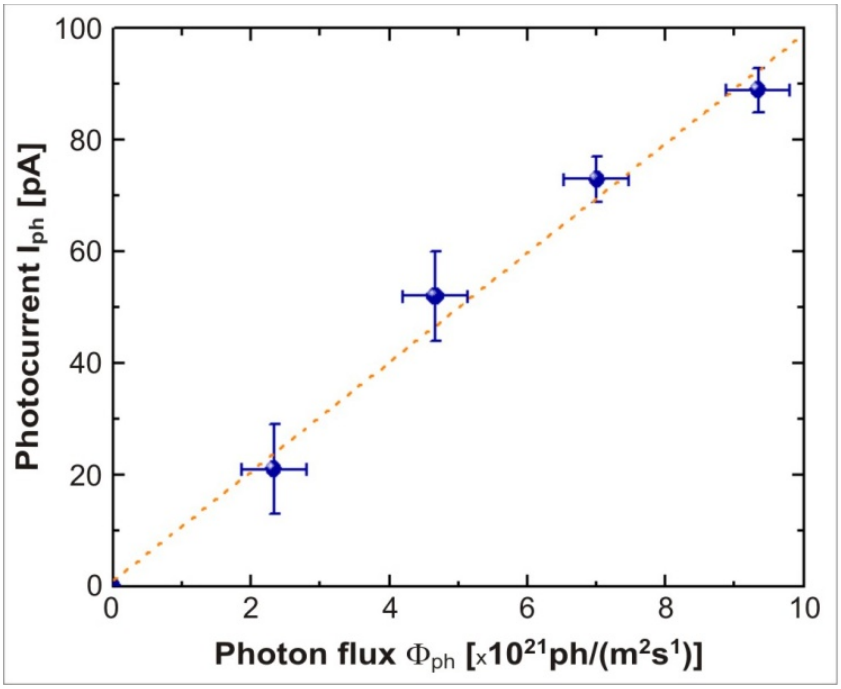

Figure 59. Photoresponse Iph of an individual Fe-doped $SrTiO_3$ nanotube under different photon fluxes at a constant polarization voltage.

Therefore, the huge difference of g_{ph} between values reported for monocrystalline nanowires and our nanorods are expected to arise from their poor carrier mobility μ^*. In fact, carriers inside polycrystalline structures are strongly slowed up by grain-boundary contributions, in which significant potential barriers may arise. Since η and $\mu^*$are the key parameters to evaluate the overall performance of photodetectors,[137] we should point out that our devices are nice proof-of-concept systems to show that an Fe-doped $SrTiO_3$ nanotube can be used as a UV photodetector.

5 Conclusions

Highly ordered anodic aluminium oxide membranes

Highly ordered stand-alone AAO membranes prepared by anodic oxidation of aluminium foil and used as templates for the EPD deposition of $BaTiO_3$ and ST sols exhibited highly ordered hexagonal arrays of nanopores with pore diameters ranging between 80 and 200 nm. The thickness of the AAO membranes was between 10 and 25 μm depending on the anodization time. Cross-sections of the AAO membranes showed that the open pores were parallel and straight throughout the whole membrane cross-section.

$BaTiO_3$ nanorods

$BaTiO_3$ nanorods were synthesized by the electrophoretic deposition (EPD) of a stoichiometric BT sol into AAO templates. Electron microscopy investigations showed that $BaTiO_3$ nanorods were dense and polycrystalline with diameters of approximately 200 nm, which is comparable with the pore diameters of the AAO templates. The lengths of $BaTiO_3$ nanorods ranged up to a few tens of micrometres. For optimization of the processing parameters for the $BaTiO_3$ nanorods synthesis the processing parameters, such as applied electric potential, time of EPD, annealing temperature and annealing time, were varied. It was found that the $BaTiO_3$ nanorods exhibited the most regular morphology when an electric potential of 30 V was applied for 30 min during EPD. The formation of the $BaTiO_3$ nanorod in a single AAO pore begins at the bottom of the template, which is in a direct contact with the cathode. Once the process of template-pore filling with the sol has started it proceeds until the whole pore is filled with the sol particles. Deposition was afterward followed by annealing the filled AAO templates for 1 hour at 700 °C. During thermal treatment, decomposition of organic precursors occurs with subsequent nucleation and growth of the $BaTiO_3$ grains. Annealing is accompanied by 25-30 % shrinkage. After annealing longer than 1 h $BaTiO_3$ grain size did not increase significantly. EDXS analysis showed that the chemical composition of $BaTiO_3$ nanorods was homogeneous,

which indicates that the targeted stoichiometry of the sol was retained throughout the whole synthesizing process.

TEM investigations showed that $BaTiO_3$ nanorods were composed of well-crystallized, defect-free, nanosized $BaTiO_3$ grains with a pseudo-cubic structure and larger grains that also contained a high population of (111) twins and disordered sequences of hexagonal $BaTiO_3$. The formation of the hexagonal polymorph was interpreted as a consequence of local reducting environment during decomposition of organic precursors in annealing process. This leads to the reduction of Ti^{4+} to Ti^{3+} and results in the formation of face-sharing octahedral, which nucleation sites for hexagonal stacking in $BaTiO_3$. In a oxygen atmosphere annealed $BaTiO_3$ nanorods contained no hexagonal polymorph.

For functionalization of $BaTiO_3$ nanorods prototype device was constructed by the integration of a single $BaTiO_3$ nanorod into simple circuit architecture. Two- and four-probe electrical DC measurements performed on $BaTiO_3$ nanorod, showing that the resistivity was between 10 and 100 ohm·cm, while the temperature-dependent experiments showed a sharp drop of electrical resistivity above 200 °C, which was attributed to the activation of electron conduction mechanisms among the grains inside the nanorod. Finally, such a prototype device composed of a single $BaTiO_3$ nanorod was tested as a proof-of-concept humidity sensor showing a large and reversible response in a varying humidity environment. It was suggested that a single $BaTiO_3$ nanorod device can be used as a humidity nanosensor.

$SrTiO_3$ nanotubes

$SrTiO_3$ nanotubes were synthesized via the controlled EPD of metal-organic precursors into AAO membranes using similar processing parameters as for the synthesis of $BaTiO_3$ nanorods. $SrTiO_3$ nanotubes were dense and polycrystalline with outer diameters of approximately 200 nm, inner diameters of approximately 150 nm and with lengths ranging up to a few tens of micrometres. In $SrTiO_3$ we observed a unique self-organizing of nanocrystals which is not yet reported for any other material prepared such procedure. Namely, after annealing the $SrTiO_3$ nanotubes were found to be composed of highly organized $SrTiO_3$ nanocrystals in an almost perfect cylindrical geometry. The resulting architecture is a consequence of three consecutive processes that took place during the firing of precursors:

- homogeneous nucleation of $SrTiO_3$ nanocrystals with a release of gaseous products,
- crystal growth and their cube-on-cube self-alignment in the thin film,
- cube-to-wall alignment during the last growth stages and their adhesion to the tube walls.

The identified mechanism of nucleation, nanocrystal growth and their self-assembly can be utilized to produce highly organized arrays of nanocrystals. The final product, demonstrated for a tubular geometry in this work, most closely mimics a $SrTiO_3$ single crystal, may be applicable in the production nanodevices as nanotemplates for the epitaxial growth of functional materials in desired geometries.

For the functionalization of Fe-doped $SrTiO_3$ nanorods the prototype device was constructed by the integration of single Fe-doped $SrTiO_3$ nanorod into a simple circuit architecture. The intrinsic properties of individual Fe-doped $SrTiO_3$ nanotubes were analyzed by investigating their current-voltage characteristics at room temperature. The electrical test performed at room temperature showed linear I-V characteristics with an electrical resistivity of a single Fe-doped $SrTiO_3$ nanotube of 35 ohm·cm. Additionally, a single Fe-doped $SrTiO_3$ nanotube-based device was tested for UV photodetector. Repeatable and reversible response under UV radiation was found with a short response and recovery times shorter than the 10 second-threshold. The measured photconductivity gain g_{ph}, between 10^{-11} to 10^{-12} m^2/V shows that such prototype devices can be used as UV photodetectors.

6 Acknowledgements

Firstly, I would like to thank my Ph.D. supervisor, Prof. Dr Miran Čeh, for his constant guidance and the valuable discussions during my work, and for the encouragement, understanding and support during my graduate study at the Jožef Stefan Institute.

I would like to thank Assist. Prof. Dr. Aleksander Rečnik for his fruitful discussions as well as for his useful remarks and suggestions about my work and also for teaching me how to operate the TEM.

I would also like to thank Assist. Prof. Dr. Sašo Šturm for his useful comments, suggestions and discussions about my research work.

My thanks also go to Prof. Dr. Andrew Bleloch (SuperSTEM Laboratory, Daresbury, UK), for fruitful discussions and teaching me how to operate the Cs-corrected STEM during my one-month scientific exchange; to Assist. Prof. Dr. Francisco Hernandez-Ramirez (Catalonia Institute for Energy Research (IREC), Barcelona, Spain), for help with the electrical measurements during my one-week scientific exchange; to Dr. Juan-Carlos Hernandez (Cambridge University, Cambridge, London), for help with tomography during my one-week scientific exchange; to Dr. Andreja Gajović (Ruđer Bošković Institute, Zagreb, Croatia), for help with the Raman measurements; to Medeja Gec, with the assistance of Birgit Bussmann, for the ultramicrotomy cross-section TEM specimen preparation (Specimen preparation was performed at StEM, MPI in Stuttgart under the ESTEEM Transnational Access to MPI (TA7).

Thanks to my colleagues in the Department for Nanostructured Materials for all their support and the nice moments that we have shared together over the past five years. Especially to Luka Suhadolnik , for help in the laboratory, to Aljaž Ivekovič, for help with the graphic design and to Assist. Prof. Dr. Paul McGuiness for the proofreading of my thesis.

Finally, I would like to thank my family for their moral support, encouragement and patience.

6 References

1 Lines, M. G. Nanomaterials for practical functional uses. *Journal of Alloys and Compounds* **449**, 242-245, (2008).

2 Xia, Y. N. *et al.* One-dimensional nanostructures: Synthesis, characterization, and applications. *Advanced Materials* **15**, 353-389 (2003).

3 Ashby, M. F., Ferreira, P., J. & Schodek, D. L. *Nanomaterials, nanotechnologies and design: An introduction for engineers and architects*. (2009).

4 Cao, G. *Nanostructures & nanomaterials : synthesis, properties & applications*. (Imperial College Press, 2004).

5 Lieber, C. M. One-dimensional nanostructures: Chemistry, physics & applications. *Solid State Communications* **107**, 607-616 (1998).

6 Lee, W., Scholz, R., Niesch, K. & Gosele, U. A template-based electrochemical method for the synthesis of multisegmented metallic nanotubes. *Angewandte Chemie-International Edition* **44**, 6050-6054, (2005).

7 Kline, T. R. *et al.* Template-grown metal nanowires. *Inorganic Chemistry* **45**, 7555-7565, (2006).

8 Cao, G. Z. Growth of oxide nanorod arrays through sol electrophoretic deposition. *Journal of Physical Chemistry B* **108**, 19921-19931, (2004).

9 Lakshmi, B. B., Dorhout, P. K. & Martin, C. R. Sol-gel template synthesis of semiconductor nanostructures. *Chemistry of Materials* **9**, 857-862 (1997).

10 Li, L., Koshizaki, N. & Li, G. H. Nanotube arrays in porous anodic alumina membranes. *Journal of Materials Science & Technology* **24**, 550-562 (2008).

11 Rorvik, P. M., Tadanaga, K., Tatsumisago, M., Grande, T. & Einarsrud, M. A. Template-assisted synthesis of $PbTiO_3$ nanotubes. *Journal of the European Ceramic Society* **29**, 2575-2579, (2009).

12 Lee, W., Ji, R., Ross, C. A., Gosele, U. & Nielsch, K. Wafer-scale Ni imprint stamps for porous alumina membranes based on interference lithography. *Small* **2**, 978-982, (2006).

13 Patzke, G. R., Krumeich, F. & Nesper, R. Oxidic nanotubes and nanorods - Anisotropic modules for a future nanotechnology. *Angewandte Chemie-International Edition* **41**, 2446-2461 (2002).

14 Moulson, A. J. & Herbert, J. M. *Electroceramics : materials properties applications*. (Chapman & Hall, 1990).

15 Spanier, J. E. *et al.* Ferroelectric phase transition in individual single-crystalline $BaTiO_3$ nanowires. *Nano Letters* **6**, 735-739, (2006).

16 Luo, J. H. & Maggard, P. A. Hydrothermal synthesis and photocatalytic activities of $SrTiO_3$-coated Fe_2O_3 and $BiFeO_3$. *Advanced Materials* **18**, 514-518, (2006).

17 Luo, Y. *et al.* Nanoshell tubes of ferroelectric lead zirconate titanate and barium titanate. *Applied Physics Letters* **83**, 440-442, (2003).

18 Wang, Z. Y., Hu, J., Suryavanshi, A. P., Yum, K. & Yu, M. F. Voltage generation from individual $BaTiO_3$ nanowires under periodic tensile mechanical load. *Nano Letters* **7**, 2966-2969, (2007).

19 Wang, Z. Y., Hu, J. & Yu, M. F. One-dimensional ferroelectric monodomain formation in single crystalline $BaTiO_3$ nanowire. *Applied Physics Letters* **89**, 2966-2969 (2007)

20 Yuk, J. & Troczynski, T. Sol-gel $BaTiO_3$ thin film for humidity sensors. *Sensors and Actuators B-Chemical* **94**, 290-293, (2003).

21 Huybrechts, B., Ishizaki, K. & Takata, M. The Positive Temperature-Coefficient of Resistivity in Barium-Titanate. *Journal of Materials Science* **30**, 2463-2474 (1995).

22 Kim, J. *et al.* Ferroelectricity in highly ordered arrays of ultra-thin-walled $Pb(Zr,Ti)O_{-3}$ nanotubes composed of nanometer-sized perovskite crystallites. *Nano Letters* **8**, 1813-1818, (2008).

23 Seo, B. I. *et al.* $Bi_{3.25}La_{0.75}Ti_3O_{12}$ (BLT) nanotube capacitors for semiconductor memories. *Physica E-Low-Dimensional Systems & Nanostructures* **37**, 274-278, (2007).

24 Urban, J. J., Spanier, J. E., Lian, O. Y., Yun, W. S. & Park, H. Single-crystalline barium titanate nanowires. *Advanced Materials* **15**, 423-426 (2003).

25 Urban, J. J., Yun, W. S., Gu, Q. & Park, H. Synthesis of single-crystalline perovskite nanorods composed of barium titanate and strontium titanate. *Journal of the American Chemical Society* **124**, 1186-1187, (2002).

26 Yun, W. S., Urban, J. J., Gu, Q. & Park, H. Ferroelectric properties of individual barium titanate nanowires investigated by scanned probe Microscopy. *Nano Letters* **2**, 447-450, (2002).

27 Zhang, X. Y. *et al.* Synthesis and piezoresponse of highly ordered $Pb(Zr_{0.53}Ti_{0.47})O_{-3}$ nanowire arrays. *Applied Physics Letters* **85**, 4190-4192, (2004).

28 Peña, M. A. & Fierro, J. L. G. Chemical Structures and Performance of Perovskite Oxides. *Chemical Reviews* **101**, 1981-2018, (2001).

29 Kholkin, A. L. *et al.* PZT-based piezoelectric composites via a modified sol-gel route. *Journal of the European Ceramic Society* **21**, 1535-1538 (2001).

30 Zhao, L. L., Steinhart, M., Yu, J. & Gosele, U. Lead titanate nano- and microtubes. *Journal of Materials Research* **21**, 685-690, (2006).

31 Tak, Y.-H., Kim, K.-B., Park, H.-G., Lee, K.-H. & Lee, J.-R. Criteria for ITO (indium-tin-oxide) thin film as the bottom electrode of an organic light emitting diode. *Thin Solid Films* **411**, 12-16, (2002).

32 Stathatos, E., Lianos, P., Lavrencic-Stangar, U. & Orel, B. A High-Performance Solid-State Dye-Sensitized Photoelectrochemical Cell Employing a Nanocomposite Gel Electrolyte Made by the Sol–Gel Route. *Advanced Materials* **14**, 354-357, (2002).

33 Bae, C. *et al.* Template-directed synthesis of oxide nanotubes: Fabrication, characterization, and applications. *Chemistry of Materials* **20**, 756-767, (2008).

34 Richerson, D. W. *Modern ceramic engineering : properties, processing, and use in design*. 2nd ed., rev. and expanded. edn, (M. Dekker, 1992).

35 Hu, Y., Tan, O. K., Cao, W. & Zhu, W. A low temperature nano-structured $SrTiO_3$ thick film oxygen gas sensor. *Ceramics International* **30**, 1819-1822, (2004).

36 Kang, S. O., Park, B. H. & Kim, Y. I. Growth mechanism of shape-controlled barium titanate nanostructures through soft chemical reaction. *Crystal Growth & Design* **8**, 3180-3186, (2008).

37 Pilania, G., Alpay, S. P. & Ramprasad, R. Ab initio study of ferroelectricity in $BaTiO_3$ nanowires. *Physical Review B* **80**, 014113-014113-7, (2009)

38 Zhao, Z. *et al.* Grain-size effects on the ferroelectric behavior of dense nanocrystalline BaTiO3 ceramics. *Physical Review B* **70**, 024107-1-024107-8, (2004)

39 Shyue, J. J., Cochran, R. E. & Padture, N. P. Transparent-conducting, gas-sensing nanostructures (nanotubes, nanowires, and thin films) of titanium oxide synthesized at near-ambient conditions. *Journal of Materials Research* **21**, 2894-2903, (2006).

40 Bach, U. *et al.* Solid-state dye-sensitized mesoporous TiO_2 solar cells with high photon-to-electron conversion efficiencies. *Nature* **395**, 583-585 (1998).

41 Liu, J. W., Chen, G., Li, Z. H. & Zhang, Z. G. Electronic structure and visible light photocatalysis water splitting property of chromium-doped $SrTiO_3$. *Journal of Solid State Chemistry* **179**, 3704-3708, (2006).

42 Xin, Y. C., Jiang, J., Huo, K. F., Hu, T. & Chu, P. K. Bioactive $SrTiO_3$ Nanotube Arrays: Strontium Delivery Platform on Ti-Based Osteoporotic Bone Implants. *Acs Nano* **3**, 3228-3234, (2009).

43 Impens, N. R. E. N., van der Voort, P. & Vansant, E. F. Silylation of micro-, meso- and non-porous oxides: a review. *Microporous and Mesoporous Materials* **28**, 217-232, (1999).

44 Joshi, U. A. & Lee, J. S. Template-free hydrothermal synthesis of single-crystalline barium titanate and strontium titanate nanowires. *Small* **1**, 1172-1176, (2005).

45 Fuentes, S. *et al.* Preparation of $SrTiO_3$ nanomaterial by a sol-gel-hydrothermal method. *Journal of Materials Science* **45**, 1448-1452, (2010).

46 Pan, Z. W., Dai, Z. R. & Wang, Z. L. Nanobelts of Semiconducting Oxides. *Science* **291**, 1947-1949, (2001).

47 Li, Y., Cheng, G. S. & Zhang, L. D. Fabrication of highly ordered ZnO nanowire arrays in anodic alumina membranes. *Journal of Materials Research* **15**, 2305-2308 (2000).

48 Liu, J. *et al.* Templateless Assembly of Molecularly Aligned Conductive Polymer Nanowires: A New Approach for Oriented Nanostructures. *Chemistry – A European Journal* **9**, 604-611, (2003).

49 Tian, Z. R. *et al.* Complex and oriented ZnO nanostructures. *Nat Mater* **2**, 821-826 (2003).

50 Chen, Y. Y., Yu, B. Y., Wang, J. H., Cochran, R. E. & Shyue, J. J. Template-Based Fabrication of SrTiO3 and BaTiO3 Nanotubes. *Inorganic Chemistry* **48**, 681-686, (2009).

51 Huczko, A. Template-based synthesis of nanomaterials. *Applied Physics a-Materials Science & Processing* **70**, 365-376 (2000).

52 Hulteen, J. C. & Martin, C. R. A general template-based method for the preparation of nanomaterials. *Journal of Materials Chemistry* **7**, 1075-1087 (1997).

53 Limmer, S. J. & Cao, G. Z. Sol-gel electrophoretic deposition for the growth of oxide nanorods. *Advanced Materials* **15**, 427-431 (2003).

54 Limmer, S. J. *et al.* Template-based growth of various oxide nanorods by sol-gel electrophoresis. *Advanced Functional Materials* **12**, 59-64 (2002).

55 Cheng, B. & Samulski, E. T. Fabrication and characterization of nanotubular semiconductor oxides InO and GaO. *Journal of Materials Chemistry* **11**, 2901-2902 (2001).

56 Adachi, M. & Lockwood, D. J. *Self-organized nanoscale materials*. (Springer, 2006).

57 Limmer, S. J., Chou, T. P. & Cao, G. Z. A study on the influences of processing parameters on the growth of oxide nanorod arrays by sol electrophoretic deposition. *Journal of Sol-Gel Science and Technology* **36**, 183-195 (2005).

58 Masuda, H. & Fukuda, K. Ordered Metal Nanohole Arrays Made by a 2-Step Replication of Honeycomb Structures of Anodic Alumina. *Science* **268**, 1466-1468 (1995).

59 Masuda, H., Hasegwa, F. & Ono, S. Self-ordering of cell arrangement of anodic porous alumina formed in sulfuric acid solution. *Journal of the Electrochemical Society* **144**, L127-L130 (1997).

60 Masuda, H., Yada, K. & Osaka, A. Self-ordering of cell configuration of anodic porous alumina with large-size pores in phosphoric acid solution. *Japanese Journal of Applied Physics Part 2-Letters* **37**, L1340-L1342 (1998).

61 Jessensky, O., Muller, F. & Gosele, U. Self-organized formation of hexagonal pore arrays in anodic alumina. *Applied Physics Letters* **72**, 1173-1175 (1998).

62 Lee, W., Ji, R., Gosele, U. & Nielsch, K. Fast fabrication of long-range ordered porous alumina membranes by hard anodization. *Nature Materials* **5**, 741-747, (2006).

63 Schwirn, K. *et al.* Self-ordered anodic aluminum oxide formed by H2SO4 hard anodization. *Acs Nano* **2**, 302-310, (2008).

64 Wu, Z., Richter, C. & Menon, L. A study of anodization process during pore formation in nanoporous alumina templates. *Journal of the Electrochemical Society* **154**, E8-E12 (2007).

65 Diggle, J. W., Downie, T. C. & Goulding, C. W. Anodic oxide films on aluminum. *Chemical Reviews* **69**, 365-405 (1969).

66 Kumar, A. *Fabrication of nanoporous alumina template for ultrahigh density magnetic recording application*. (2005).

67 Yasuda, K., Macak, J. M., Berger, S., Ghicov, A. & Schmuki, P. Mechanistic aspects of the self-organization process for oxide nanotube formation on valve metals. *Journal of the Electrochemical Society* **154**, C472-C478, (2007).

68 Montero-Moreno, J. M., Sarret, M. & Muller, C. Influence of the aluminum surface on the final results of a two-step anodizing. *Surface & Coatings Technology* **201**, 6352-6357, (2007).

69 Brinker, C. J. & Scherer, G. W. *Sol-gel science : the physics and chemistry of sol-gel processing*. (Academic Press, 1990).

70 Matsuda, H., Kobayashi, N., Kobayashi, T., Miyazawa, K. i. & Kuwabara, M. Room-temperature synthesis of crystalline barium titanate thin films by high-concentration sol-gel method. *Journal of Non-Crystalline Solids* **271**, 162-166, (2000).

71 Haruta, M. & Delmon, B. Preparation of Homodisperse Solids. *Journal De Chimie Physique Et De Physico-Chimie Biologique* **83**, 859-868 (1986).

72 Nielsen, A. E. *Kinetics of precipitation*. (Pergamon, 1964).

73 Stein, A. & Schroden, R. C. Colloidal crystal templating of three-dimensionally ordered macroporous solids: materials for photonics and beyond. *Current Opinion in Solid State and Materials Science* **5**, 553-564, (2001).

74 Oldenburg, S. J., Averitt, R. D., Westcott, S. L. & Halas, N. J. Nanoengineering of optical resonances. *Chemical Physics Letters* **288**, 243-247, (1998).

75 Besra, L. & Liu, M. A review on fundamentals and applications of electrophoretic deposition (EPD). *Progress in Materials Science* **52**, 1-61, (2007).

76 Fukada, Y. *et al.* Electrophoretic deposition - mechanisms, myths and materials. *Journal of Materials Science* **39**, 787-801 (2004).

77 Sarkar, P. & Nicholson, P. S. Electrophoretic deposition (EPD): Mechanisms, kinetics, and application to ceramics. *Journal of the American Ceramic Society* **79**, 1987-2002 (1996).

78 De, D. & Nicholson, P. S. Role of ionic depletion in deposition during electrophoretic deposition. *Journal of the American Ceramic Society* **82**, 3031-3036 (1999).

79 Attar, A. S. *et al.* Synthesis and characterization of anatase and rutile TiO_2 nanorods by template-assisted method. *Journal of Materials Science* **43**, 5924-5929, (2008).

80 Feng, M., Wang, W., Zhou, Y. & Jia, D. C. Synthesis and characterization of ferroelectric $SrBi_2Ta_2O_9$ nanotubes arrays. *Journal of Sol-Gel Science and Technology* **52**, 120-123, (2009).

81 Lin, Y., Wu, G. S., Yuan, X. Y., Xie, T. & Zhang, L. D. Fabrication and optical properties of TiO_2 nanowire arrays made by sol-gel electrophoresis deposition into anodic alumina membranes. *Journal of Physics-Condensed Matter* **15**, 2917-2922, (2003).

82 Wang, F., Wang, J. B., Zhong, X. L., Li, B. & Zhou, Y. C. Synthesis and characterization of $Bi_{3.15}Nd_{0.85}Ti_3O_{12}$ nanotube arrays. *Journal of Crystal Growth* **311**, 4495-4498, (2009).

83 Wang, J., Manivannan, A. & Wu, N. Q. Sol-gel derived $La_{0.6}Sr_{0.4}CoO_3$ nanoparticles, nanotubes, nanowires and thin films. *Thin Solid Films* **517**, 582-587, (2008).

84 Singh, S. & Krupanidhi, S. B. Synthesis and structural characterization of $Ba_{0.6}Sr_{0.4}TiO_3$ nanotubes. *Physics Letters A* **367**, 356-359, (2007).

85 Hernandez, B. A., Chang, K. S., Fisher, E. R. & Dorhout, P. K. Sol-gel template synthesis and characterization of $BaTiO_3$ and $PbTiO_3$ nanotubes. *Chemistry of Materials* **14**, 480-482, (2002).

86 Hsu, M. C., Leu, I. C., Sun, Y. M. & Hon, M. H. Template synthesis and characterization of PbTiO3 nanowire arrays from aqueous solution. *Journal of Solid State Chemistry* **179**, 1421-1425, (2006).

87 Wen, T. L., Zhang, J., Chou, T. P., Limmer, S. J. & Cao, G. Z. Template-based growth of oxide nanorod arrays by centrifugation. *Journal of Sol-Gel Science and Technology* **33**, 193-200 (2005).

88 Limmer, S. J., Chou, T. P. & Cao, G. Z. A study on the growth of TiO_2 nanorods using sol electrophoresis. *Journal of Materials Science* **39**, 895-901 (2004).

89 Hunter, R. J. *Zeta potential in colloid science : principles and applications*. (Academic Press, 1981).

90 Callister, W. D. *Materials science and engineering : an introduction*. 4th ed. edn, (Wiley, 1997).

91 Limmer, S. J., Cruz, S. V. & Cao, G. Z. Films and nanorods of transparent conducting oxide ITO by a citric acid sol route. *Applied Physics a-Materials Science & Processing* **79**, 421-424, (2004).

92 Limmer, S. J. *et al.* Electrophoretic growth of lead zirconate titanate nanorods. *Advanced Materials* **13**, 1269-1272 (2001).

93 Zagar, K., Recnik, A., Ajayan, P. M. & Ceh, M. Oriented cube-on-cube nanocrystal assembly of $SrTiO_3$ tubules. *Nanotechnology* **21**, 375605-375612, (2010).

94 Lin, Y., Sun, F. Q., Yuan, X. Y., Geng, B. Y. & Zhang, L. D. Sol-gel electrophoretic deposition and optical properties of Fe_2O_3 nanowire arrays. *Applied Physics a-Materials Science & Processing* **78**, 1197-1199, (2004).

95 Nourmohammadi, A., Bahrevar, M. A., Schulze, S. & Hietschold, M. Electrodeposition of lead zirconate titanate nanotubes. *Journal of Materials Science* **43**, 4753-4759, (2008).

96 Zagar, K., Recnik, A., Sturm, S., Gajovic, A. & Ceh, M. Structural and chemical characterization of $BaTiO_3$ nanorods. *Materials Research Bulletin* **46**, 366-371, (2011).

97 Wang, Y. C., Leu, I. C. & Hon, M. H. Preparation of nanosized ZnO arrays by electrophoretic deposition. *Electrochemical and Solid State Letters* **5**, C53-C55, (2002).

98 Wang, Y. C., Leu, I. C. & Hon, M. H. Preparation and characterization of nanosized ZnO arrays by electrophoretic deposition. *Journal of Crystal Growth* **237**, 564-568, (2002).

99 Wang, Y. C., Leu, I. C. & Hon, M. H. Effect of colloid characteristics on the fabrication of ZnO nanowire arrays by electrophoretic deposition. *Journal of Materials Chemistry* **12**, 2439-2444, (2002).

100 Wang, Y. C., Leu, I. C. & Hon, M. H. Size control of ZnO nanofibril within template by electrophoretic deposition. *Electrochemical and Solid State Letters* **7**, D15-D18, (2004).

101 Miao, J., Hu, C. G., Xiong, Y. F., Han, X. Y. & Yi, X. Self-assembly behavior of $SrTiO_3$ nano-sheets and conversion of sheets into cubes. *Acta Physico-Chimica Sinica* **23**, 1599-1602 (2007).

102 Wada, S. *et al.* Preparation of nm-sized barium titanate fine particles and their powder dielectric properties. *Japanese Journal of Applied Physics Part 1-Regular Papers Short Notes & Review Papers* **42**, 6188-6195, (2003).

103 Picard, E., Vermogen, A., Gerard, J. F. & Espuche, E. Barrier properties of nylon 6-montmorillonite nanocomposite membranes prepared by melt blending: Influence of the clay content and dispersion state - Consequences on modelling. *Journal of Membrane Science* **292**, 133-144, (2007).

104 Quintana, C. Ultramicrotomy for cross-sections of nanostructure. *Micron* **28**, 217-219 (1997).

105 Cliff, G. & Lorimer, G. W. The quantitative analysis of thin specimens. *Journal of Microscopy* **103**, 203-207 (1975).

106 Hernandez-Ramirez, F. *et al.* Characterization of metal-oxide nanosensors fabricated with focused ion beam (FIB). *Sensors and Actuators B-Chemical* **118**, 198-203, (2006).

107 Hernandez-Ramirez, F. *et al.* Electrical properties of individual tin oxide nanowires contacted to platinum electrodes. *Physical Review B* **76**, 0854929-1-085429-5 (2007)

108 Hernandez-Ramirez, F. *et al.* Fabrication and electrical characterization of circuits based on individual tin oxide nanowires. *Nanotechnology* **17**, 5577-5583, (2006).

109 Prades, J. D. *et al.* Ultralow power consumption gas sensors based on self-heated individual nanowires. *Applied Physics Letters* **93**, 123110, (2008)

110 Prades, J. D. *et al.* Direct observation of the gas-surface interaction kinetics in nanowires through pulsed self-heating assisted conductometric measurements. *Applied Physics Letters* **95**, 053101, (2009)

111 Hernandez-Ramirez, F. *et al.* Portable microsensors based on individual $SnO_{(2)}$ nanowires. *Nanotechnology* **18**, 495501, (2007).

112 Guo, D. Z. *et al.* Preparation and annealing-induced structural transition of self-organized nanostripes on the electropolished aluminium surface. *Chinese Physics Letters* **19**, 385-388 (2002).

113 Sui, Y. C., Gonzalez-Leon, J. A., Bermudez, A. & Saniger, J. M. Synthesis of multi branched carbon nanotubes in porous anodic aluminum oxide template. *Carbon* **39**, 1709-1715 (2001).

114 Shiratori, Y., Pithan, C., Dornseiffer, J. & Waser, R. Raman scattering studies on nanocrystalline BaTiO3 - Part I - isolated particles and aggregates. *Journal of Raman Spectroscopy* **38**, 1288-1299, (2007).

115 Shiratori, Y., Pithan, C., Dornseiffer, J. & Waser, R. Raman scattering studies on nanocrystalline BaTiO3 - Part II - consolidated polycrystalline ceramics. *Journal of Raman Spectroscopy* **38**, 1300-1306, (2007).

116 Yashima, M. *et al.* Size effect on the crystal structure of barium titanate nanoparticles. *Journal of Applied Physics* **98**, (2005)

117 Pasha, U. M. *et al.* In situ Raman spectroscopy of A-site doped barium titanate. *Applied Physics Letters* **91**, (2007)

118 Joshi, U. A., Yoon, S. H., Baik, S. G. & Lee, J. S. Surfactant-free hydrothermal synthesis of highly tetragonal barium titanate nanowires: A structural investigation. *Journal of Physical Chemistry B* **110**, 12249-12256, (2006).

119 Cho, W. S. Structural evolution and characterization of $BaTiO_3$ nanoparticles synthesized from polymeric precursor. *Journal of Physics and Chemistry of Solids* **59**, 659-666 (1998).

120 Kirby, K. W. & Wechsler, B. A. Phase-Relations in the Barium Titanate-Titanium Oxide System. *Journal of the American Ceramic Society* **74**, 1841-1847 (1991).

121 Lee, S., Randall, C. A. & Liu, Z. K. Modified phase diagram for the barium oxide-titanium dioxide system for the ferroelectric barium titanate. *Journal of the American Ceramic Society* **90**, 2589-2594, (2007).

122 Rase, D. E. & Roy, R. Phase Equilibria in the System $BaO–TiO_2$. *Journal of the American Ceramic Society* **38**, 102-113, (1955).

123 Wang, Z. L. & Cowley, J. M. Simulating High-Angle Annular Dark-Field Stem Images Including Inelastic Thermal Diffuse-Scattering. *Ultramicroscopy* **31**, 437-454 (1989).

124 Recnik, A. Twins in barium titanate. *Acta Chimica Slovenica* **48**, 1-50 (2001).

125 Recnik, A., Bruley, J., Mader, W., Kolar, D. & Ruhle, M. Structural and Spectroscopic Investigation of (111) Twins in Barium-Titanate. *Philosophical Magazine B-Physics of Condensed Matter Statistical Mechanics Electronic Optical and Magnetic Properties* **70**, 1021-1034 (1994).

126 Recnik, A. & Kolar, D. Exaggerated growth of hexagonal barium titanate under reducing sintering conditions. *Journal of the American Ceramic Society* **79**, 1015-1018 (1996).

127 Hamada, E., Cho, W. S. & Takayanagi, K. Nanotwins in $BaTiO_3$ nanocrystals. *Philosophical Magazine a-Physics of Condensed Matter Structure Defects and Mechanical Properties* **77**, 1301-1308 (1998).

128 Chen, Y. C. Annealing effects of semiconducting barium-titanate thermister. *Journal of Marine Science and Technology-Taiwan* **15**, 307-314 (2007).

129 Glower, D. D. & Heckman, R. C. Conduction-Ionic or Electronic-in $BaTiO_3$. *Journal of Chemical Physics* **41**, 877-879 (1964).

130 Bigger, J. V. & Gardopee, G. J. Hydrogen Reduction of $BaTiO_3$ Ceramics. *Ceramic Bulletin* **53**, 53-56 (1974).

131 Rečnik, A. Nahajališča mineralov v Sloveniji. 384 (Jozef Stefan Institute, 2007).

132 Midgley, P. A. *et al.* Nanoscale scanning transmission electron tomography. *Journal of Microscopy-Oxford* **223**, 185-190 (2006).

133 Ang, C., Yu, Z. & Jing, Z. Dielectric spectra and electrical conduction in Fe-doped $SrTiO_3$. *Physical Review B* **61**, 3922-3926 (2000).

134 Steinsvik, S., Bugge, R., Gjonnes, J., Tafto, J. & Norby, T. The defect structure of $SrTi_{1-x}Fe_xO_{3-y}$ (x=0-0.8) investigated by electrical conductivity measurements and electron energy loss spectroscopy (EELS). *Journal of Physics and Chemistry of Solids* **58**, 969-976 (1997).

135 Rodewald, S., Fleig, J. & Maier, J. Measurement of conductivity profiles in acceptor-doped strontium titanate. *Journal of the European Ceramic Society* **19**, 797-801 (1999).

136 Kind, H., Yan, H. Q., Messer, B., Law, M. & Yang, P. D. Nanowire ultraviolet photodetectors and optical switches. *Advanced Materials* **14**, 158-160 (2002).

137 Prades, J. D. *et al.* Toward a systematic understanding of photodetectors based on individual metal oxide nanowires. *Journal of Physical Chemistry C* **112**, 14639-14644, (2008).

List of figures

List of tables

Appendix

Articles and other component parts

Original scientific article

1. K. Žagar, A. Rečnik, P. M. Ajayan, M. Čeh, Oriented cube-on-cube nanocrystal assembly of $SrTiO_3$ tubules. *Nanotechnology (Bristol)*, 2010, vol. 21, no. 37, str. 375605-1-375605-7.

2. K. Žagar, A. Rečnik, S. Šturm, M. Čeh, Structural and chemical characterization of $BaTiO_3$ nanorods. *Mater. res. bull.*. [Print ed.], 2011, vol. 46, no. 3, str. 366-371, doi: 10.1016/j.materresbull.2010.12.012 |.

3. A. Gajović, S. Šturm, B. Jančar, A. Šantić, K. Žagar, M. Čeh, The synthesis of pure-phase bismuth ferrite in the Bi–Fe–O system under hydrothermal conditions without a mineralizer, *J. Am. Ceram. Soc.*, 2010, vol. 93, no. 10, str. 3173-3179.

4. G. Kramberger, V. Cindro, I. Mandić, M. Mikuž, M. Milovanović, M. Zavrtanik, K. Žagar. Investigation of irradiated silicon detectors. *IEEE trans. nucl. sci.*, 2010, vol. 57, no. 4, str. 2294-2302, doi: 10.1109/TNS.2010.2051957.

Patents

1. D. Verhovšek, T. Gominšek, M. Čeh, P. Blagotinšek, S. Šturm, K. Žagar, *Nanodelci anatasa in postopek sinteze za pridobivanje nanodelcev anatasa = patentna prijava št. P-200900341*. Ljubljana: Urad RS za intelektualno lastnino, 4. nov. 2009.

2. D. Verhovšek , T. Rožman, M. Čeh, P. Blagotinšek, S. Šturm, K. Žagar, *Nanodelci rutila in postopek sinteze za pridobivanje nanodelcev : patentna prijava P-200900340*. Ljubljana: Urad RS za intelektualno lastnino, 14. nov. 2009.

Published scientific conference contribution

1. K. Žagar, S. Šturm, M. Čeh, Template-assisted synthesis and characterization of $BaTiO_3$ nanorods. V: NEBESÁŘOVÁ, Jana (ur.), HOZÁK, Pavel (ur.). 8th Multinational Congress on Microscopy, June 17-21, 2007, Prague Czech Republic. *Proceedings*. [Prague]: Czechoslovak Microscopy Society, cop. 2007, p. 323-324.

2. K. Žagar, S. Šturm, M. Čeh, Template-assisted synthesis and characterization of $SrTiO_3$ nanostructures. V: RICHTER, Silvia (ur.), SCHWEDT, Alexander (ur.). 14th European

Microscopy Congress, 1-5 September 2008, Aachen, Germany. *EMC 2008*. Berlin; Heidelberg: Springer, 2008, zv. 2, p. 585-586.

3. M. Gec, K. Žagar, B. Bussmann, P.A. van Aken, M Čeh, Preparation of nanotubes for cross-sectional TEM/STEM observation. V: KOTHLEITNER, Gerald (ur.), LEISCH, Manfred (ur.). Microscopy Conference, Graz, Austria, 30 August - 4 September 2009. *MC 2009. Vol. 1, Instrumentation and methodology*. Graz: Verlag der Technischen Universität, 2009, p. 245-246.

4. K. Žagar, M. Čeh, Synthesis and characterization of $SrTiO_3$ nanotubes. V: GROGGER, Werner (ur.), HOFER, Ferdinand (ur.), PÖLT, Peter (ur.). Microscopy Conference, Graz, Austria, 30 August - 4 September 2009. *MC 2009. Vol. 3, Materials Science*. Graz: Verlag der Technischen Universität, 2009, p. 65-66.

5. D. Verhovšek, K. Žagar, M. Čeh, The syntheis and characterization of rutile titanium oxide nanoparticles. V: GROGGER, Werner (ur.), HOFER, Ferdinand (ur.), PÖLT, Peter (ur.). Microscopy Conference, Graz, Austria, 30 August - 4 September 2009. *MC 2009. Vol. 3, Materials Science*. Graz: Verlag der Technischen Universität, 2009, p. 127-128.

6. K. Žagar, L. Suhadolnik, M. Čeh, Synthesis of $BaTiO_3$ nanorods : optimization of processing parameters and electron microscopy characterization. V: IMC 17, 17th International Microscopy Congress, Sepetember 19-24, Rio de Janeiro, Brazil. *Revealing the nanoworld in life and materials science : proceedings*. [S. l.]: SBMM: = Sociedade Brasileria de Microscopia e Microanálise, 2010, 2 str.

7. K. Žagar, F. Hernandez-Ramirez, J-R. Morante, M. Čeh. Template-assisted processing, structural and electrical characterization of barium titanate nanorods. V: IMC 17, 17th International Microscopy Congress, Sepetember 19-24, Rio de Janeiro, Brazil. *Revealing the nanoworld in life and materials science : proceedings*. [S. l.]: SBMM: = Sociedade Brasileria de Microscopia e Microanálise, 2010, 2 str.

Published scientific conference contribution abstract

1. K. Žagar, S. Šturm, M. Čeh, Synthesis and characterization of perovskite nanorods. *Mater. tehnol.*, 2007, letn. 41, št. 6, p. 307-309.

2. K. Žagar, S. Šturm, M. Čeh, Synthesis and characterization of perovskite nanorods V: JENKO, Monika (ur.). 15th Conference on Materials and Technology, 8-10 October, 2007 Portorož, Slovenia. *Program in knjiga povzetkov*. Ljubljana: Inštitut za kovinske materiale in tehnologije], 2007, p. 54.

3. K. Žagar, S. Šturm, M. Čeh, Synthesis and characterization of $BaTiO_3$ nanorods. V: USKOKOVIĆ, Dragan (ur.). Ninth Annual Conference of the Yugoslav Materials Research Society YUCOMAT 2007, Herceg Novi, September 10-14, 2007. *Programme and the book of abstracts*. Belgrade: Institute of Technical Sciences of SASA, 2007, p. 146.

4. K. Žagar, S. Šturm, M. Čeh, Synthesis and characterization of $BaTiO_3$ nanorods. V: *SLONANO 2007 : 10-12 October, Jožef Stefan Institute, Ljubljana, Slovenia : programme & abstracts*. Ljubljana: Jožef Stefan Institute, 2007.

5. K. Žagar, A. Gajović, S. Šturm, M. Čeh, $BaTiO_3$ nanorods : new insight by Raman spectroscopy. V: MUSIĆ, Svetozar (ur.), RISTIĆ, Mira (ur.), KREHULA, Stjepko (ur.). XXIX European Congress on Molecular Spectrosopy [also] EUCMOS 2008, Opatija, Croatia, August 31st - September 5th 2008. *Book of abstracts*. [S. l.: s. n., 2008], p. 181.

6. K. Žagar, S. Šturm, M. Čeh, Synthesis and characterization of $SrTiO_3$ nanostructures. V: MIHAILOVIĆ, Dragan (ur.), KOBE, Spomenka (ur.), REMŠKAR, Maja (ur.), JAMNIK, Janko (ur.), ČOPIČ, Martin (ur.), DROBNE, Damjana (ur.). *Hot nano topics 2008 : incorporating SLONANO 2008, 3 overlapping workshops on current hot subjects in nanoscience, 23-30 May, Portorož, Slovenia : abstract book*. Ljubljana: [s. n.], 2008, p. 118.

7. K. Žagar, S. Šturm, M. Čeh, Template-assisted synthesis of $BaTiO_3$ nanorods. V: KOBE, Spomenka (ur.), ŽUŽEK ROŽMAN, Kristina (ur.), NOVAK, Saša (ur.), FIDLER, Sanja (ur.). *WomenInNano winter school : 7-9 February 2008, Kranjska Gora, Slovenia : abstract book*. [S.l.: s.n.], 2008, p. 117.

8. K. Žagar, S. Šturm, M. Čeh, Synthesis and characterization of $BaTiO_3$ nanostructures. V: 33rd International Conference and Exposition on Advanced Ceramics and Composites, January 18-23, 2009, Daytona Beach, Florida, USA. *Abstracts book*. [S. l.]: The American Ceramic Society, 2009, p. 73.

9. K. Žagar, S. Šturm, M. Čeh, Template-assisted synthesis and characterization of $SrTiO_3$ nanostructures. V: 33rd International Conference and Exposition on Advanced Ceramics and Composites, January 18-23, 2009, Daytona Beach, Florida, USA. *Abstracts book*. [S. l.]: The American Ceramic Society, 2009, p. 73.

10. K. Žagar, A. Rečnik, M. Čeh, Template-assisted synthesis and characterization of perovskite nanostructure. V: 1st MACAN Conference on Interfaces, Novermber 14-17, 2009, Berlin, Germany. *Abstracts*, (FP7-NMP-2009-CSA, 233484 MACAN). [S. l.: s. n.], 2009, p. 76-77.

11. K. Žagar, S. Šturm, M. Čeh, Sol-gel elektroforetska depozicija in karakterizacija $SrTiO_3$ nanostruktur. V: ISKRA, Jernej (ur.), MILOŠEV, Ingrid (ur.). *Dan mladih raziskovalcev 2009*. Ljubljana: Institut "Jožef Stefan", 2009, 1 p.

12. K. Žagar, A. Rečnik, M. Čeh, Sinteza in karakterizacija perovskitnih nanostruktur. V: KUŠČER, Danjela (ur.), PERC, Branka (ur.). 4. Dan Mladih Raziskovalcev KMBO, Ljubljana, Slovenija, 11.2.2010. *[Program in povzetki]*. Ljubljana: Institut "Jožef Stefan", 2010, p. 45.

13. K. Žagar, F. Hernandez-Ramirez, J-R. Morante, M. Čeh. Template-assisted and characterization of barium titanate nanorods. V: MIHAILOVIĆ, Dragan (ur.), HOČEVAR, Samo B. (ur.), ARČON, Denis (ur.), KUNEJ, Špela (ur.), UMEK, Polona (ur.), KNAVS,

Martina (ur.). *Book of abstracts : SLONANO 2010, 20-22 October 2010, Ljubljana, Slovenia*. Ljubljana: National Institute of Chemistry, 2010, str. 99.

14. K. Žagar, A. Rečnik, P. M. Ajayan, M. Čeh. Samourejanje nanokristalov znotraj submikronskih $SrTiO_3$ cevk. V: PRIBOŠIČ, Irena (ur.), KRNEL, Kristoffer (ur.). 5. Dan Mladih Raziskovalcev, Ljubljana, Februar 2011. *[Program in povzetki]*. Ljubljana: Institut "Jožef Stefan", 2011, str. 12.